# SILICON ANODES FOR LITHIUM-ION BATTERIES

A Dissertation

by

KASTURI SARANG

Submitted to the Office of Graduate and Professional Studies of
Texas A&M University
in partial fulfillment of the requirements for the degree of

DOCTOR OF PHILOSOPHY

| | |
|---|---|
| Chair of Committee, | Jodie L. Lutkenhaus |
| Committee Members, | Yossef A. Elabd |
| | Perla B. Balbuena |
| | Svetlana A. Sukhishvili |
| Head of Department, | Arul Jayaraman |

May 2021

Major Subject: Chemical Engineering

ABSTRACT

Silicon anodes are promising for high energy density lithium-ion batteries because of their high theoretical capacity (3579 mAh/g) and low potential of ~0.2 V *vs.* $Li/Li^+$. However, silicon undergoes >300% volume changes during cycling. This causes delamination from the current collector and unstable solid electrolyte interphase (SEI) build-up, leading to rapid capacity fade during battery cycling. To address these issues, binder and conducting carbon, are added to the silicon anode. In this dissertation, we explored a new binder, conductive additive, and anode architecture, and also identified the interactions between the anode components that led to improved cycling performance.

Binders improve cohesion between anode components and adhesion to the current collector. We demonstrated the use of tannic acid, a natural polyphenol, as a binder for silicon anodes. Tannic acid was explored as a small molecule binder with abundant hydroxyl (−OH) groups (14.8 mmol of OH/g of tannic acid). This allowed for the specific evaluation of hydrogen-bonding interactions without the consideration of particle bridging that occurs otherwise with high molecular weight long-chain polymers. The resultant silicon anodes demonstrated a capacity of ~850 mAh/g at 0.5 C-rate.

Along with huge volume expansion, silicon has poor conductivity which requires the addition of hydrophobic carbon, thus effectively diluting the active silicon material. To address this issue, we used minimal amount of MXene nanosheets (4 wt% in the entire anode) to maximize total silicon anode capacity. We made silicon anodes using a composite binder of sodium alginate and MXenes that demonstrated capacities of ~900 mAh/g at 0.5 C-rate. The stable anode performance even with a minimal MXene content

is attributed to homogenous electrode formation with improved interactions due to high conductivity, hydrophilicity, and large lateral size of MXene nanosheets.

To stabilize SEI build-up, the contact between silicon and electrolyte should be minimized. Thus, we made a yolk-shell type structure by crumpling MXene nanosheets around silicon particles via a spray-dryer. Our electrodes made using crumpled MX/Si capsules demonstrated decent cycling capacities, while minimizing the electrode's through-plane expansion. An in-house comparison of crumpled with uncrumpled anode showed that crumpling does improve cycling stability due to stable SEI formation.

# ACKNOWLEDGEMENTS

I am eternally grateful for my thesis advisor, Dr. Jodie L. Lutkenhaus, whose expertise and guidance was invaluable in formulating my research topics. She has been an amazing mentor to me, always guiding me in my research and my professional development. I would like to thank her for being patient with me, caring for me, and motivating me to bring out my skills and abilities. She has very unique technical, communication, and managing skills which I hope to incorporate in my future professional life.

I would also like to thank my committee members, Dr. Yossef A. Elabd, Dr. Perla B. Balbuena, and Dr. Svetlana A. Sukhishvili, for their guidance and support throughout the course of this research. I have highly valued your inputs during committee meetings and preliminary exams.

I am very grateful to Dr. Micah Green, Dr. Miladin Radovic , and their team members, Xiaofei Zhao, Dustin Holta, Huaixuan Chao, for providing me with MXenes and for their constant guidance on MXenes-based projects.

I am also thankful to our collaborators, Dr. Rafael Verduzco (Rice University), Dr. Eun0Suok Oh (University of Ulsan), and Dr. Andrea Miranda (now at Applied Materials, Inc.) for teaching me about silicon anodes. I am also thankful to Dr. Eun-Suok Oh for teaching us the basics of electrochemistry, as it has helped me in the long run.

I highly appreciate my Ph.D. mentor, Dr. Hyosung An, who gave me valuable learnings during my two years in my Ph.D. I thank my amazing lab colleagues and friends,

Dr. Pilar Suarez-Martinez, Dr. Anish Patel, Dr. Shaoyang Wang, Dr. Ting Ma, Dr. Junyeong Yun, Dr. Yilan Ye, Dr. Josh O'Neal, Paraskevi Flouda, Alexandra Easley, Ian Echols, Dimitrios Loufakis, Suvesh Lalwani, Suyash Oka, Chikaodinaka Eneh, Ratul Mitra Thakur, Natalie Neal, Ahmed Emara, Sabrina Pickert, Selena Li, Nutan Patil, Naveen Mishra, Niranjan Sitapure, Rushant Sabnis, Saloni Raina, and Sushrut Kaul for constantly being there throughout my Ph.D. You all have not only helped me with technical difficulties, but have also held my hand in difficult times and helped me move ahead in my life.

I would like to thank the staff, Ashley Henley, Terah Cooper, Bridgette Gray, Su Liu, and Louis Muniz, of the Artie McFerrin Department of Engineering for their help in making sure I graduated. I highly appreciate the training Dr. Yordanos Bisrat and Dr. Jing Wu provided on SEM and XPS equipment.

Finally, I would like to thank my Mom (Mohini Sarang), Dad (Tulashidas Sarang), my twin brother (Kaustubh Sarang), and Rohan Bhirangi for always supporting me. They have always cheered and cared for me, and I thank them for having their blessings showered on me all the time.

CONTRIBUTORS AND FUNDING SOURCES

## Contributors

This work was supervised by my graduate advisor and thesis committee: Dr. Jodie Lutkenhaus (advisor) of the Chemical Engineering Department, Dr. Yossef Elabd (committee member) of the Chemical Engineering Department, Dr. Perla Balbuena (committee member) of the Chemical Engineering Department, and Dr. Svetlana Sukhishvili (committee member) of the Materials Science and Engineering Department.

Chapter II and Chapter III was in collaboration with Xiaoyi Li (Department of Chemical and Biomolecular Engineering, Rice University), Andrea Miranda (Department of Chemical and Biomolecular Engineering, Rice University), Tanguy Terlier (ToF-SIMS instrument Manager, Rice University), Eun-Suok Oh (School of Chemical Engineering, University of Ulsan), Rafael Verduzco (Department of Chemical and Biomolecular Engineering, Rice University), and Jodie L. Lutkenhaus (Department of Chemical Engineering, Texas A&M University).

Chapter IV was in collaboration with Xiaofei Zhao (Department of Chemical Engineering, Texas A&M University), Dustin Holta (Department of Materials Science and Engineering, Texas A&M University), Miladin Radovic (Department of Materials Science and Engineering, Texas A&M University), Micah Green (Department of Chemical Engineering, Texas A&M University), Eun-Suok Oh (School of Chemical Engineering, University of Ulsan), and Jodie L. Lutkenhaus (Department of Chemical Engineering, Texas A&M University). In addition, the authors thank Tan Nguyen for his

assistance with the Attenuated Total Reflectometry Fourier Transform Infrared Spectroscopy analysis.

Chapter V was in collaboration with Xiaofei Zhao (Department of Chemical Engineering, Texas A&M University), Dustin Holta (Department of Materials Science and Engineering, Texas A&M University), Huaixuan Cao (Department of Chemical Engineering, Texas A&M University), Paraskevi Flouda (Department of Materials Science and Engineering, Texas A&M University), Miladin Radovic (Department of Materials Science and Engineering, Texas A&M University), Micah Green (Department of Chemical Engineering, Texas A&M University), and Jodie L. Lutkenhaus (Department of Chemical Engineering, Texas A&M University).

**Funding Sources**

Graduate study was supported by the Artie McFerrin Department of Chemical Engineering with their graduate student assistantship. This work was supported by the National Science Foundation (grant numbers 1604666, 1604682, and 1760859).

This work's contents are solely the responsibility of the authors and do not necessarily represent the official views of the Texas A&M University Office of Graduate and Professional Studies and National Science Foundation.

TABLE OF CONTENTS

Page

LIST OF FIGURES

Page

LIST OF TABLES

Page

# CHAPTER I

# INTRODUCTION

## Rechargeable lithium-ion battery

Our world was transformed in the last three decades by the invention of a device that nearly everybody on earth carries in their pockets today. That device is, of course, the humble lithium-ion battery. The first successful commercialization of a rechargeable lithium-ion battery was done by Sony in 1991.[1] They made the world's first high power density, light weight, portable size, and long-life lithium-ion battery based on a carbon anode and lithium cobalt oxide ($LiCoO_2$) cathode which exhibited an open circuit voltage of over 3.6 V, and an energy density of 150 Wh/kg.[1] The energy density of commercial cells has almost doubled since their introduction in 1991. Now, lithium-ion batteries have wide variety of applications ranging from consumer (electronic devices, power tools, electric vehicle etc.) to industry (wind and solar grid scale storage), Figure I-1a.[2] Tremendous research effort has been undertaken, and considerable progress has been made in developing the material systems and different components of lithium-ion batteries.

Lithium-ion battery consists of four major components; anode (negative electrode), cathode (positive electrode), electrolyte, and separator, Figure I-1b and the description of each is provided in the following sections.

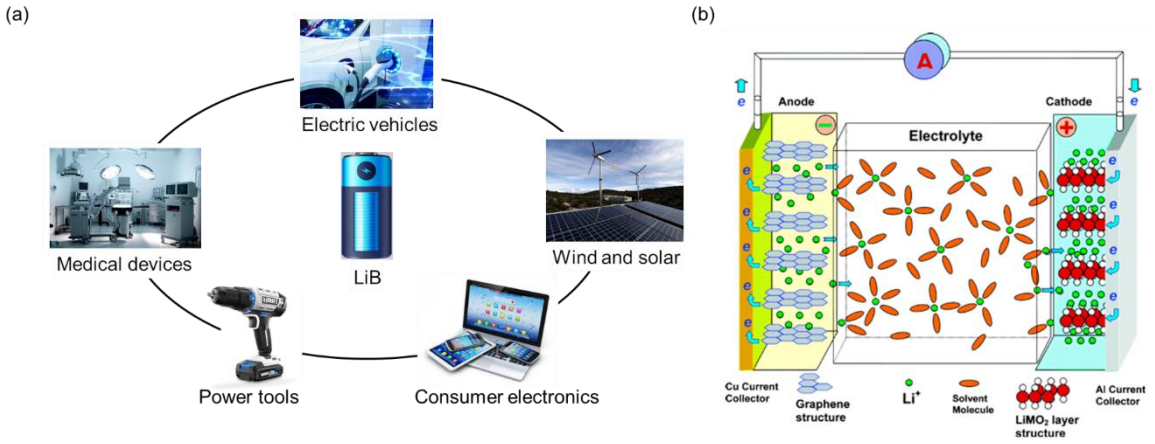


Figure I-1. (a) Applications of lithium-ion battery. (b) Working of a basic lithium-ion battery. Reprinted with permission from reference [3]. Copyright (2004) American Chemical Society.

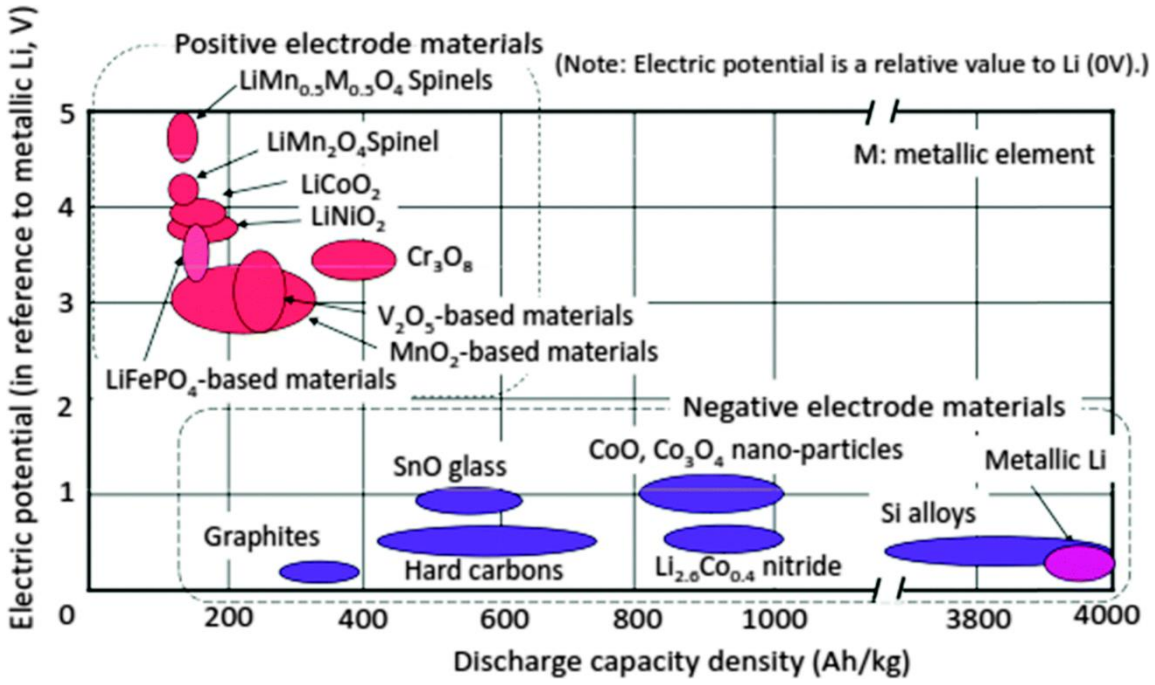


Figure I-2. List of cathode and anode active materials used in lithium-ion batteries and their respective electric potential and capacities. Reprinted with permission from reference [4]. Copyright (2015) Royal Society of Chemistry.

***Anode and cathode***

In a lithium-ion battery, anode is the negative electrode and cathode is the positive electrode. Several materials for anode and cathode have been explored (Figure I-2). Cathode active material have high electric potential and anode active material have low electric potential. The cathode active materials include $LiCoO_2$, lithium iron phosphate, lithium manganese oxide, lithium nickel oxide, and vanadium oxides. The anode active materials include graphite, carbon-based materials, silicon, and lithium metal. However, in a commercial lithium-ion battery, the most commonly used anode is graphite and cathode is $LiCoO_2$. Both these materials store energy via an intercalation mechanism.[5] The working of a lithium-ion battery represents a rocking chair mechanism wherein the lithium ions move from cathode to anode during charge and back from anode to cathode during discharge.[6] The following reactions takes place in the graphite anode and $LiCoO_2$ cathode:

$$\text{Cathode: } LiCoO_2 \leftrightarrow Li_xCoO_2 + xLi^+ + xe^- \quad \ldots 1.1$$

$$\text{Anode: } 6C + xLi^+ + xe^- \leftrightarrow Li_xC_6 \quad \ldots 1.2$$

The electrons travel in the external circuit and the balanced $Li^+$ ions travel in the electrolyte system back and forth between anode and cathode.

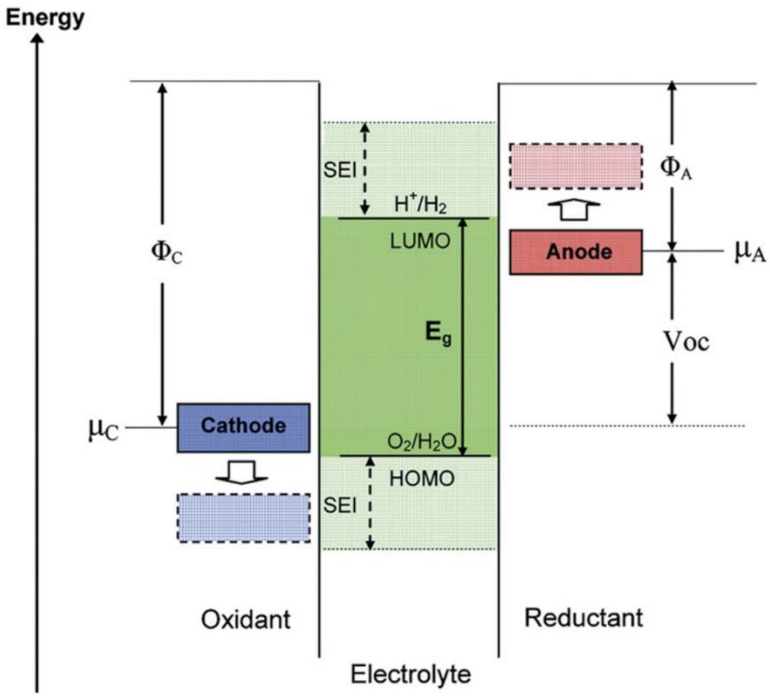


Figure I-3. Schematic open-circuit energy diagram of an electrolyte. $\Phi_A$ and $\Phi_C$ are the anode and cathode work functions. $E_g$ is the electrolyte's electrochemical stability window. $\mu_A$ and $\mu_C$ are the redox potential of the anode and cathode, respectively. Reprinted with permission from reference [7]. Copyright (2010) American Chemical Society.

***Electrolyte***

The electrolyte serves as a medium that enables movement of only lithium ions between anode and cathode. The electrolyte is typically a liquid that consist of lithium salts (*e.g.* lithium hexafluorophosphate ($LiPF_6$)) dissolved in mixture of organic solvents. The organic solvents used in the electrolyte are combination of a cyclic carbonate (*e.g.* ethylene carbonate (EC)) and a linear carbonate (*e.g.* diethyl carbonate (DEC)). They cyclic carbonate is highly polar solvent that assists in the dissociation and dissolution of lithium salt, and the linear carbonate assist in the migration of $Li^+$ ions.[8] For an electrochemically stable battery, anode must have lower electrochemical potential ($\mu_A$)

than the lowest unoccupied molecular orbital (LUMO) of the electrolyte, otherwise the electrolyte will be degraded, and cathode must have higher electrochemical potential ($\mu_C$) than the highest occupied molecular orbital (HOMO) of the electrolyte to prevent the oxidation of the electrolyte (Figure I-3).[8]

***Separator***

The separator physically separates the anode and cathode to prevent short-circuit and allows $Li^+$ ions to pass through it. The main characteristics/parameters that affect the performance of a separator are permeability, porosity/pore size, electrolyte absorption and retention, chemical, mechanical and thermal stability.[9] Typically, Celgard polypropylene based separators are used in a battery.

**Silicon anode**

The growing lithium-ion battery markets require increased levels of performance in terms of energy density, fast charging properties, and be lighter in weight, more so than the current generation of lithium-ion batteries.[10] Over the past 30 years, lithium-ion batteries based on intercalation electrode materials have been utilized in consumer electronics and electrical transportation; however, intercalation-type electrode materials have reach their performance limit.[11] There is a need to increase energy density of electrodes by modifying the cell chemistry, specifically anode and cathode chemistries. Tremendous research is being done in the area of cathodes which is provided in some great reviews.[12-14]

To replace the conventional graphite anodes in lithium-ion batteries, several high capacity anode materials are explored; for *e.g.*, silicon (Si), germanium (Ge), lithium

titanium oxide (LTO), tin (Sn) etc. Among a variety of emerging anode materials for substituting the conventional graphite, silicon has been considered as the most outstanding candidate because it has one of the highest theoretical capacity of 3579 mAh/g (10 times the gravimetric capacity of graphite.[15, 16] Table I-1 and Figure I-2 show several anode materials studied for a lithium-ion battery.

Table I-1. Properties of some commonly studied anode materials.

| **Anode material** | **Lithiated phase** | **Theoretical capacity (mAh/g)** | **Lithiation potential** | **Delithiation potential** | **Volume change** |
|---|---|---|---|---|---|
| **Graphite** | $LiC_6$ | 375 | 0.07, 0.1, 0.19 | 0.1, 0.14, 0.23 | 10% |
| **Si** | $Li_{3.75}Si$ | 3579 | 0.05, 0.21 | 0.31, 0.47 | 300% |
| **Ge** | $Li_{4.4}Ge$ | 1625 | 0.2, 0.3, 0.5 | 0.5, 0.62 | 240% |
| **Sn** | $Li_{4.4}Sn$ | 994 | 0.4, 0.57, 0.69 | 0.58, 0.7, 0.78 | 255% |
| **LTO** | $Li_7Ti_5O_{12}$ | 175 | 1.55 | 1.58 | 0.2% |

Silicon react with lithium via an alloying mechanism, which involves breaking the bonds between host atoms. This mechanism is very different than intercalation mechanism observed in graphite. The large difference in capacity between silicon and graphite arises because a silicon atom can bond with upto about four lithium ions while it takes six carbon atoms to bond with only one lithium ion.[15] Eqns. (1.3) and (1.4) are the half reactions for the silicon and graphite anodes, respectively.

$$6C + Li^+ + e^- \leftrightarrow LiC_6 \quad \ldots 1.3$$

$$Si + 3.75Li^+ + 3.75e^- \leftrightarrow Li_{3.75}Si \quad \ldots 1.4$$

Some papers have shown that one silicon atom can accommodate upto 4.4 $Li^+$ ions giving capacities upto 4200 mAh/g.[17, 18] The lithiation potential of silicon is higher than that of graphite which further minimizes the issues of lithium plating that occurs at potentials close to 0 V *vs.* $Li/Li^+$.[19] But, the potential is low enough such that when paired with a cathode can provide a huge potential difference that can ultimately increase the energy density of the battery. Silicon is a second most abundant element on the earth and the large-scale production has been well developed for decades.[19]

***Properties of silicon***

Silicon is a chemical element with symbol Si and atomic number 14. Despite being the eighth most common element in the universe by mass, silicon very rarely occurs as a pure free element in the Earth's crust. Silicon has been widely applied in solar cells and semiconductors and thus large scale production of silicon is a matured technology. Silicon can either be crystalline or amorphous in nature. Silicon is a fourfold coordinated atom that is tetrahedrally bonded to four neighboring silicon atoms with lattice constants of 5.431 Å (Figure I-4). In crystalline silicon (*c*-Si), this tetrahedral structure continues over a long range, thereby forming a well-ordered crystal lattice. Amorphous silicon (*a*-Si) is the non-crystalline form of silicon, which has no long range order. *c*-Si is easy to synthesize and is extensively studied as compared to *a*-Si.

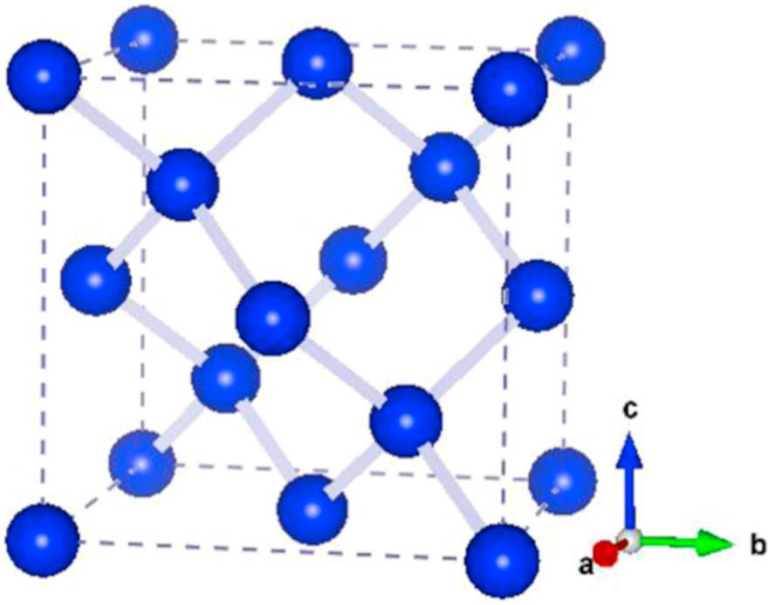


Figure I-4. Structure of crystalline silicon. Reprinted with permission from reference [20]. Copyright (2015) Elsevier.

***Energy storage in silicon***

Silicon undergoes almost 300% volumetric expansion during lithiation.[21] In order to understand the reason behind this volumetric expansion, it is essential to understand the energy storage mechanism of silicon. *c*-Si is electrochemically lithiated via a two-phase mechanism in which the silicon is consumed to form lithiated amorphous silicon (*a*-$Li_XSi$), and the two phases are separated by a sharp reaction front of nanometer scale thickness (Figure I-5a).[22, 23] The formation of highly lithiated silicon at the reaction front causes almost 300% volume expansion. The huge volume expansion occurs because of breakage of Si-Si bonds to form Li-Si bonds.[24, 25] It was shown that most of the expansion occurs at the <110> face of silicon due to difference in interfacial mobilities of the crystallographic planes (Figure I-5b).[22, 26]

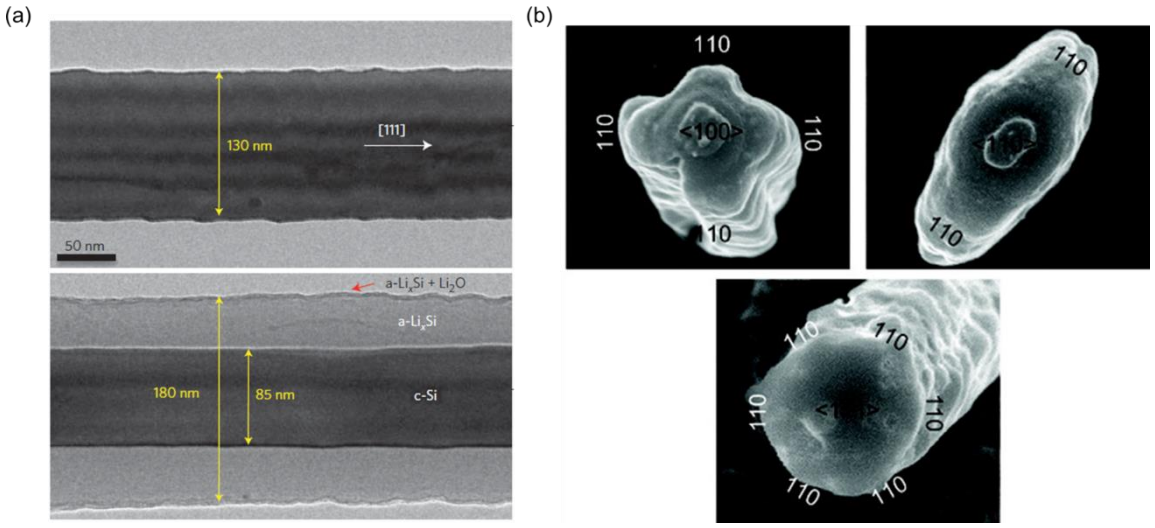


Figure I-5. (a) Two phase lithiation reaction of silicon nanowire. The sharp reaction front between crystalline silicon (*c*-Si) and amorphous silicon (a-$Li_XSi$) and is visible. Reprinted with permission from reference [22]. Copyright (2012) Springer Nature. (b) Preferential expansion of silicon particle at <110> face. Reprinted with permission from reference [26]. Copyright (2011) American Chemical Society.

***Stress generation in silicon***

There were a few computational studies that calculated modulus and stress during lithiation and delithiation of silicon.[27-30] It was reported that as the lithiation progressed, a drop in modulus is observed, which implies that silicon becomes softer on lithiation because the strength of Li-Si bonds is much lower than that of Si-Si bonds.[27] This Li-assisted Si-Si bond breaking and re-forming is largely responsible for plastic flow.[31] Sethuraman *et al.* multi-beam optical sensor technique to experimentally study in-situ stress generation in silicon thin films during lithiation and delithiation.[30] They observed that as the lithiation progressed, a transition from elastic loading to plastic deformation occurred in silicon film. During delithiation, the same behavior was observed but with tensile instead of compressive stress. The high stress of ~1 GPa that occurs in silicon

anode during lithiation and delithiation causes changes in electrochemical potential (as high as 100-125 mV/GPa) which results in voltage hysteresis.[32] The compressive stress during lithiation would decrease the voltage from the equilibrium value and the tensile stress during delithiation would increase it.

***Drawbacks of silicon anode***

Silicon anode stores upto 4 $Li^+$ ions during lithiation which gives very high capacities, but in order to accommodate those $Li^+$ ions, silicon undergoes huge 300% volume expansion. This volume expansion causes extreme instability in silicon anode resulting in drop in capacities during cycling. Figure I-6 shows an example of the charge-discharge curves of silicon powder with an average size of 10 μm.[33] High capacity is achieved on the first lithiation, but capacity quickly fades with cycle number, with only 30% capacity retention at the end of five cycles.

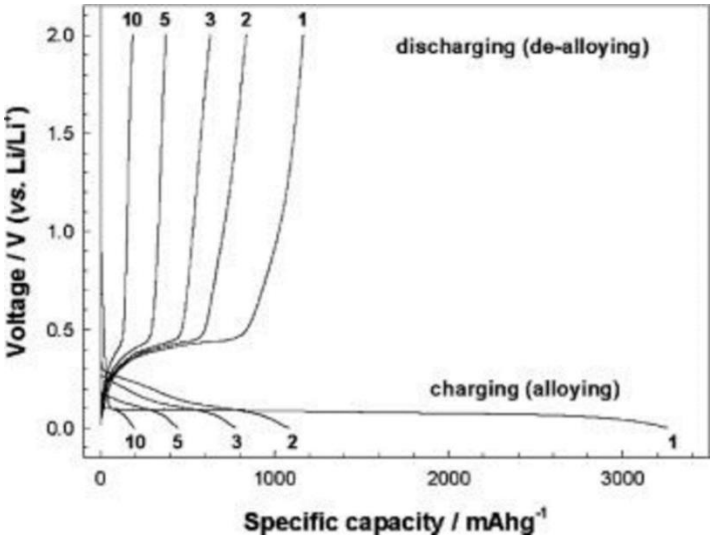


Figure I-6. Galvanostatic charge-discharge voltage profiles obtained with a 10 μm diameter sized silicon powder anode. The gravimetric current density was 100 mA/g and the voltage cut-off range was 0-2 V *vs.* $Li/Li^+$. Reprinted with permission from reference [33]. Copyright (2004) The Electrochemical Society.

Volumetric expansion causes stress generation in silicon particles which results in pulverization, *i.e.* breakage into smaller-sized particles (Figure I-8).[34] This is caused because of hoop tension generated on silicon surface due to two-phase electrochemical lithiation. However, Liu *et al*. used in-situ TEM analysis to show that silicon particles of size<150 nm do not undergo pulverization as the stresses generated during volumetric expansion do not overcome the strain fracture (Figure I-7a-d).[35] Additionally, smaller sized particles shortens the ion diffusion.

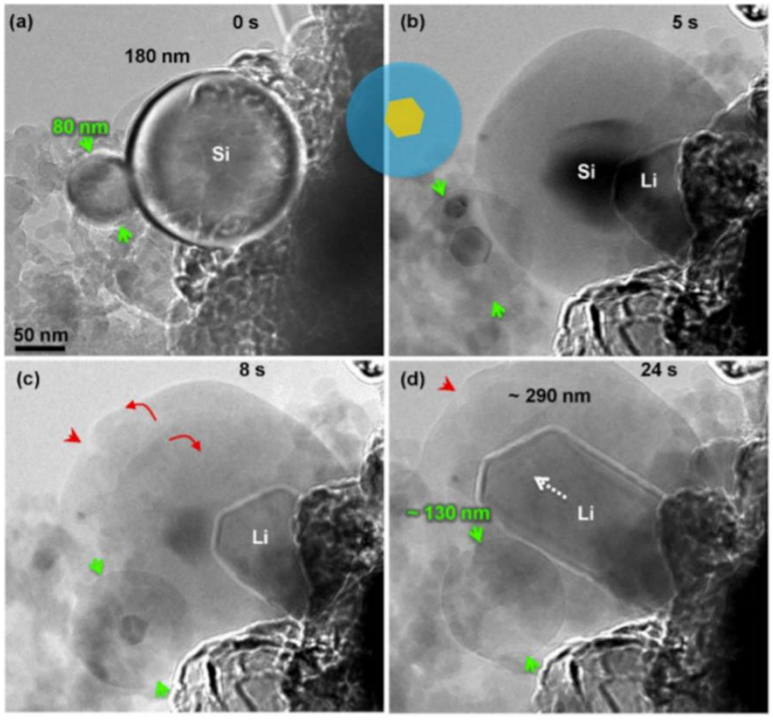


Figure I-7. (a) Pristine round silicon particles with diameters of 80 and 180 nm (labelled). (b) Core-shell structure during the lithiation. The smaller silicon particle had a hexagonal core. (c) Cracks (marked by the red arrows) formed when the $Li_XSi$ shell was thickened. (d) Fully lithiated silicon particles. Reprinted with permission form reference [35]. Copyright (2012) American Chemical Society.

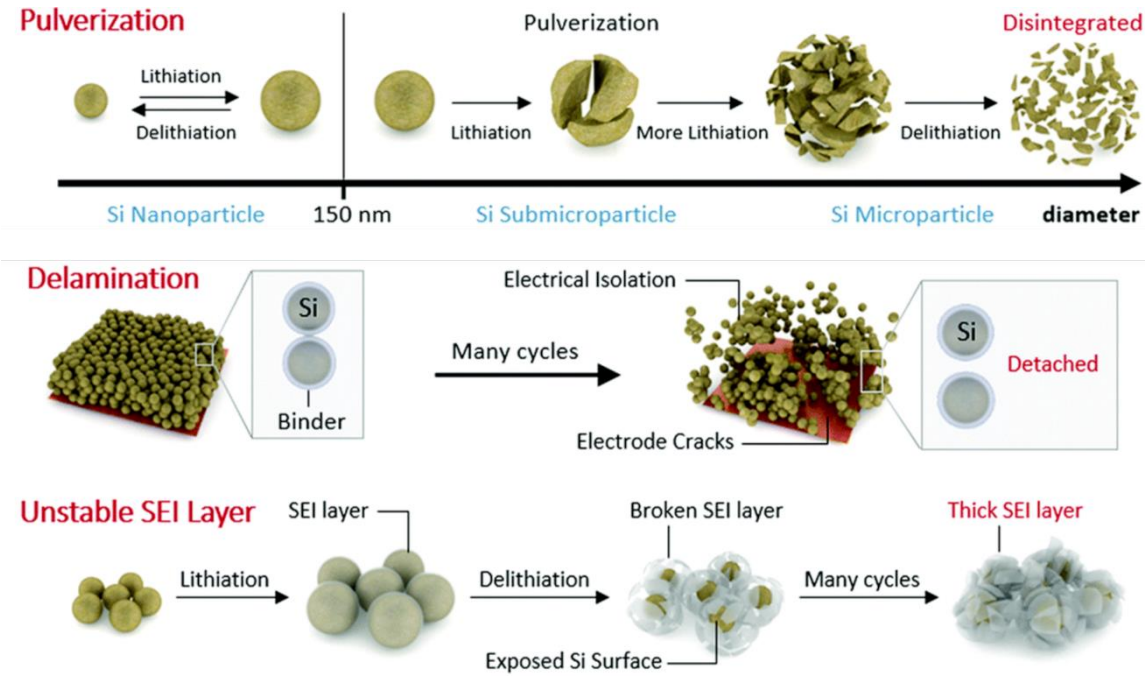


Figure I-8. Three representative failure mechanisms of silicon anodes: pulverization, delamination, and unstable solid electrolyte interphase (SEI) layer formation. Reprinted with permission form reference [36]. Copyright (2018) Royal Society of Chemistry.

Even though the pulverization issue is minimized by using silicon particle of size<150 nm, they will still undergo volumetric expansion. This causes delamination of silicon particles from the current collector, and they also separate from each other which disrupts the path of electron flow (Figure I-8).[36] This also causes formation of irreversibly lithiated silicon particles that cannot undergo delithiation due to loss of  loss of electronic contact.

When the potential of the anode is below ~1 V *vs.* $Li/Li^+$, the electrolyte decomposes and the products are deposited on the anode surface to form a layer called as the solid-electrolyte interphase (SEI).[37] Briefly, the SEI film is a multi-layered structure—an inorganic inner layer near the electrode/SEI interface which consist of lithium

carbonate, lithium fluoride, lithium oxide, lithium silicates etc., that allows $Li^+$ transport; and an organic outer layer (ROCOOLi, R depends on solvent), which is heterogeneous, porous, and permeable to both $Li^+$ and electrolyte solvent molecules, near the SEI/electrolyte interface.[8] The SEI layer is electronically insulating, but ionically conducting, and thus it prevents further decomposition of electrolyte.[38] However, the huge volumetric expansion occurring in silicon causes the SEI layer to break down thus exposing more silicon surface to the electrolyte and causing excessive SEI buildup during cycling (Figure I-8).[34] This causes drop in capacities because the $Li^+$ ions that should ideally be utilized by silicon for energy storage are instead getting irreversibly consumed during SEI formation. Excessive SEI buildup also unnecessarily increases electrode's resistance causing further drop in capacities. One important term to monitor SEI stability or growth is the Coulombic efficiency (CE). CE is the ratio of delithiation capacity to lithiation capacity, and thus more the SEI formation, lower is the CE value.

Silicon has poor electrical conductivity ($10^{-3}$ S/cm) and low ion diffusivity ($10^{-14}$-$10^{-13}$ $cm^2/s$) which further hinders transport of ions and electrons throughout the electrode.[21]

To address the issues of delamination, unstable SEI buildup, and poor conductivity, binders and conductive additives are utilized. The binder will improve the cohesion of electrode components and adhesion to the current collector. The conductive additives will maintain electronic conductivity throughout the electrode. Thus, silicon anode is actually a composite of silicon particles, binder and conductive additives as

shown in Figure I-9a. A typical distribution of these components in silicon anode reported in literature is shown in Figure I-9b.

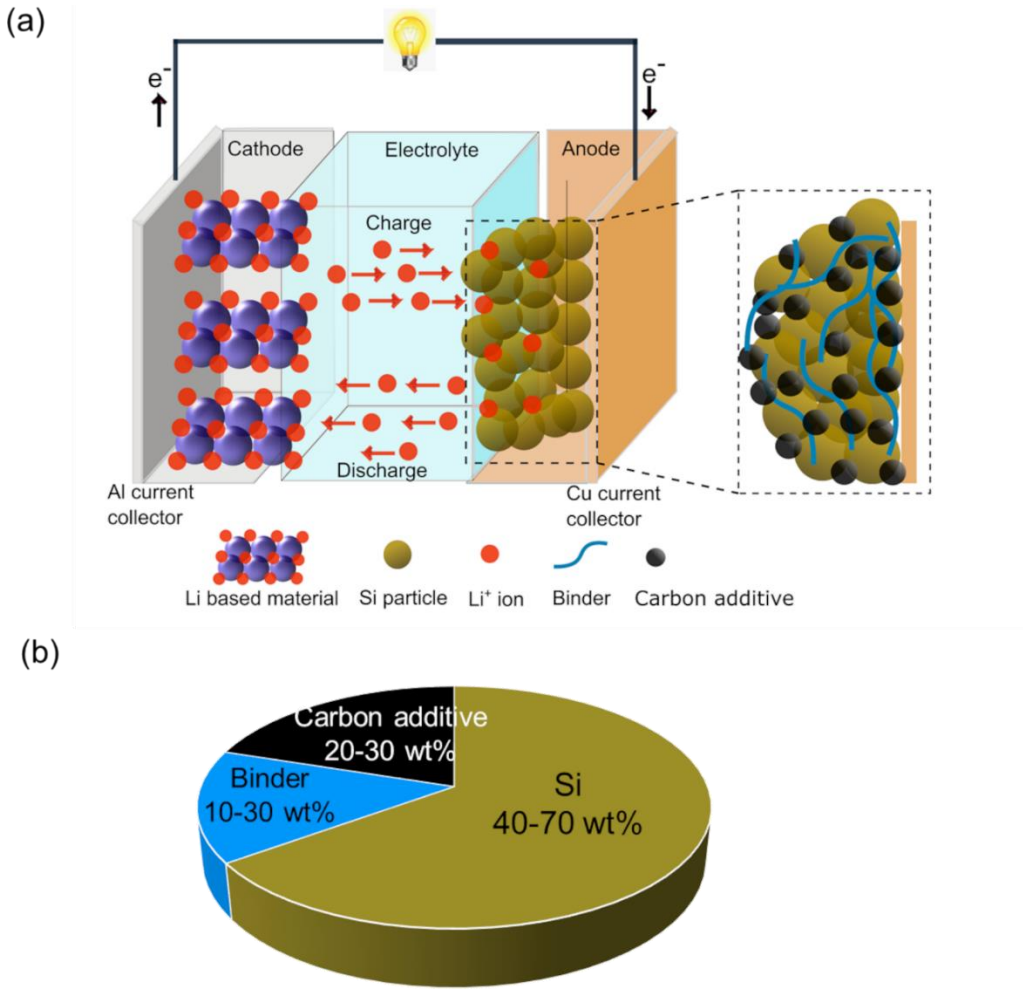


Figure I-9. (a) Working of a lithium-ion battery with silicon as an anode. Zoomed in image shows silicon anode with binder and carbon additives. (b) Typical range of composition of silicon anode reported in published literature

## MXenes

### *What are MXenes?*

MXenes (pronounced as “maxines”) are a new category of two-dimensional (2D) metal carbides, constituted by transition-metal carbides, nitrides, and carbonitrides. They

were recently discovered by Gogotsi and group in 2011.[39] They are synthesized from a MAX phase where M can be any transition metal, A can be any group A element, and X can be either C or N (Figure I-10).[40] In other words, the MAX phase structure can be described as 2D layers of early transition metal carbides and/or nitrides "glued" together with an A element. To make MXenes, the A layer is etched out from the MAX phase so as to get a layered structure. The general formula of MXenes is $M_{n+1}X_nT_X$, where n is the no of layers (typical n is 1 to 4) and $T_X$ are the surface functional groups (-OH, -O, -F, Cl, *etc*.). The distribution of surface functional groups are highly dependent on the synthesis method.[41] These polar terminal groups result in strong hydrophilicity and electronegativity, which allow them to be dispersed in water and form a suspension. In addition, the types and distribution of terminal groups can have a strong impact on the properties, stability, and functionality of MXenes.[42] Controlling the M and X elements as well as the number of layers makes it possible to tune the physicochemical properties of MXene. Prior studies have highlighted MXenes' hydrophilicity, excellent electrical and thermal conductivities, ease of processability, and in-plane stiffness.[43] These materials hold promise for a wide range of applications in batteries, supercapacitors, electronic sensors, electromagnetic interference shielding, and electrocatalysts.[44, 45] The most studied MXenes to date is $Ti_3C_2T_x$ because it is easier to synthesize and has the highest electrical conductivity ($10^4$ S/cm).[41]

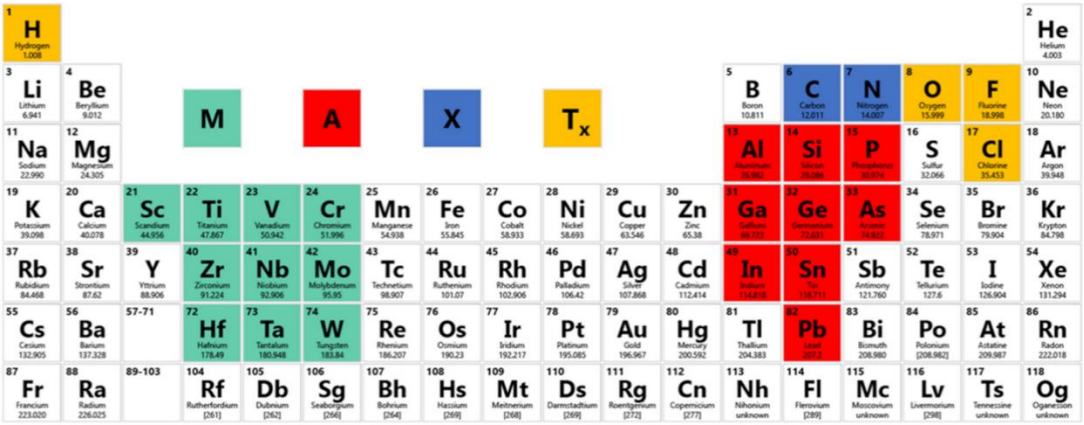


Figure I-10. Elements used to build MAX phases and MXenes. Reprinted with permission form reference [40]. Copyright (2019) John Wiley and Sons.

### *Synthesis of $Ti_3C_2T_x$ MXene nanosheets*

Several methods have been reported in literature to synthesize the $Ti_3C_2T_x$ MXene nanosheets.[46] However, we used the mild acid etching method consisting of lithium fluoride and hydrochloric acid (Figure I-11a-b).

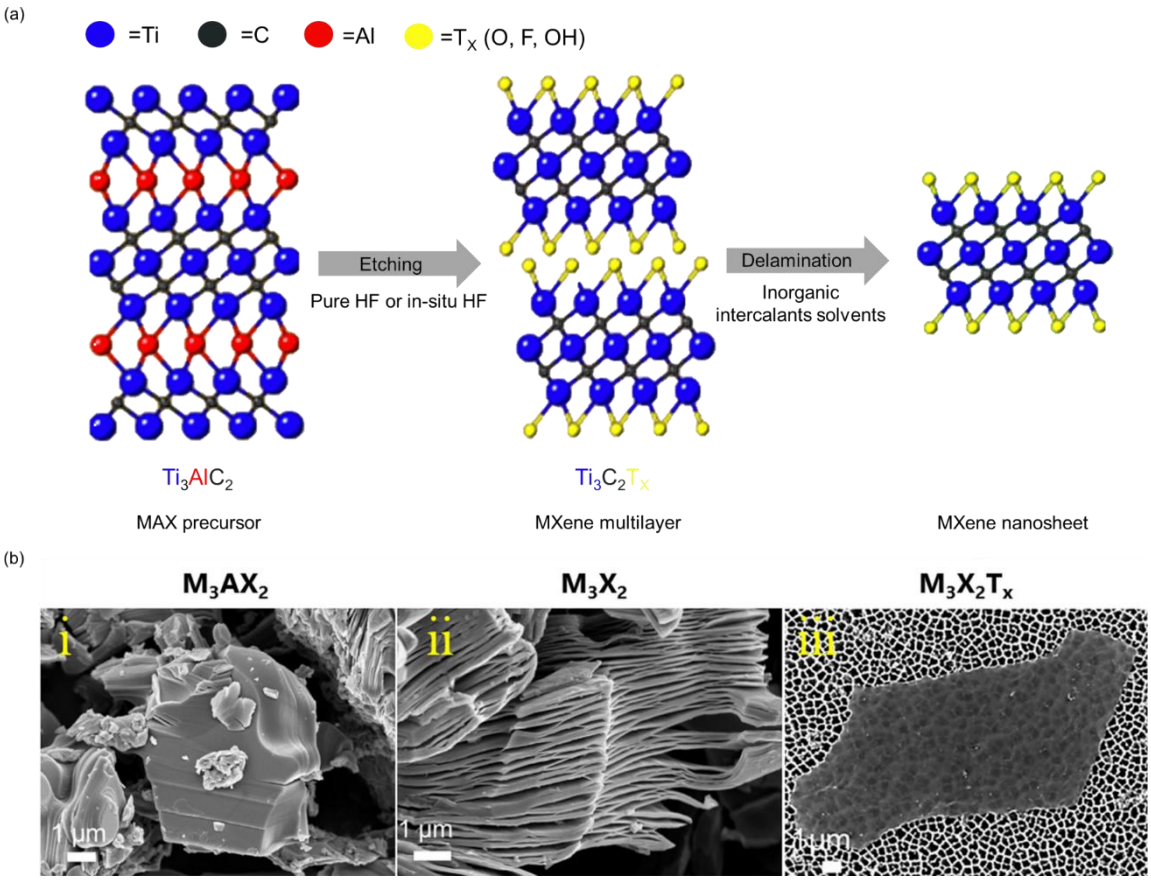


Figure I-11. (a) Step-by-step description of $Ti_3C_2T_x$ MXene synthesis from $Ti_3AlC_2$ MAX precursor. Reproduced with permission from reference [47]. Copyright (2020) Elsevier. (b) SEM images of (i) MAX phase, (ii) non delaminated MXene, and (iii) delaminated MXene. Reproduced with permission from reference [46]. Copyright (2017) American Chemical Society.

### *Synthesis of $Ti_3AlC_2$ MAX phase*

$Ti_3AlC_2$ MAX phase was synthesized from Ti (with a particle size of 44 µm and 99.5% purity), Al (with a particle size of 44 µm and 99.5% purity) and TiC (with a particle size of 2-3 µm and 99.5% purity) powders which were mixed in the molar ratio of Ti: Al: TiC=1.2:1.2:1.8. All chemicals were used as received from Alfa Aesar, MA, USA. The bulk high-purity $Ti_3AlC_2$ samples were synthesized by heating up the Ti+Al+TiC powder

mixture in a tube furnace to 1510 ℃ at 10 ℃/min and being kept for 4 hours. After sintering, the highly porous bulk $Ti_3AlC_2$ samples were drill-milled to obtain $Ti_3AlC_2$ powder, which was then sieved to obtain the powder with particle size less than 45 μm.

***Synthesis of $Ti_3C_2T_x$ MXene clay***

$Ti_3C_2T_x$ MXene clay was obtained by etching the Al layer from the sieved MAX phase by a wet etching method. 50 mL of 6 M hydrochloric acid (HCL) solution (ACS reagent, Sigma-Aldrich) and 3 g of lithium fluoride (LiF) (with the purity of 98+%, Alfa Aesar) were first mixed in a polypropylene bottle until all LiF was dissolved. The solution was heated to 35 °C before 5 g of as-prepared MAX powder was slowly added into the solution over 15 minutes to prevent overheating. The mixture was continuously agitated and reacted for 40 hours. Deionized water was used to wash the MXene clay repeatedly until pH of the water effluent reached a minimum value of 6.

***Intercalation and delamination of $Ti_3C_2T_x$ MX clay***

MXene clay was intercalated with dimethyl sulfoxide (DMSO) (>99.5%, Sigma-Aldrich) with agitation for 20 hours. After washing the DMSO away by distilled water, the MXene clay in water dispersion was bath sonicated for 60 mins to exfoliate into nanosheets. The delaminated dispersion was centrifuged at 3500 rpm for 1 hour to separate the unexfoliated MXenes and other heavier components. The supernatant containing the $Ti_3C_2T_x$ nanosheet dispersion was collected after centrifugation, while the sediment after centrifugation was discarded.

### *Characterization of $Ti_3C_2T_x$ MXene nanosheets*

To confirm the successful synthesis of MXenes we used X-ray diffraction (XRD) and X-ray photoelectron spectroscopy (XPS) analysis. The XRD in Figure I-12a shows a shift in (002) peak from 9.7º for $Ti_3AlC_2$ to 6.5º for $Ti_3C_2T_X$, which suggests increase d-spacing and decreased thickness of $Ti_3C_2T_x$ layers.[48] The XPS spectra revealed Ti 2p, O 1s, C 1s, F 1s peaks attributed to MXene nanosheets. AFM was used to measure thickness and lateral size of MXene nanosheets. The sample tested using AFM was prepared by dropping casting the diluted MXene dispersion on a freshly cleaved mica substrate. The sample was dried overnight under vacuum at 40 °C. Height profiles of nanosheets were obtained in tapping mode (Bruker dimension icon AFM). The thickness and lateral size of the as-synthesized MXene nanosheets was around 1 nm and 1 µm, respectively.

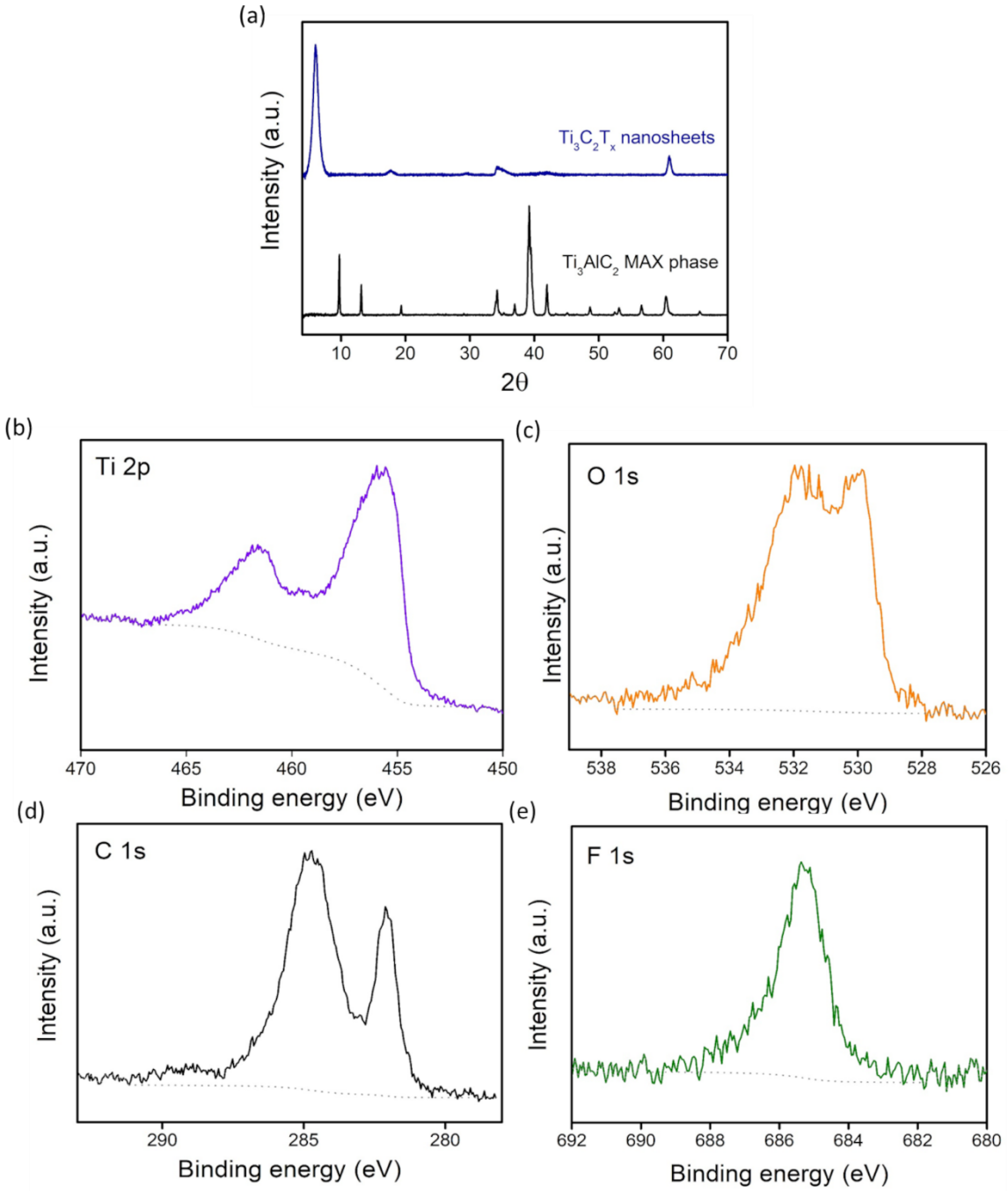


Figure I-12. (a) X-ray diffraction spectra (XRD) of $Ti_3AlC_2$ MAX phase and $Ti_3C_2T_x$ MXene nanosheets (b)-(e) X-ray photoelectron spectroscopy (XPS) spectra of Ti 2p, O 1s, C 1s, and F 1s for the MXene nanosheets.

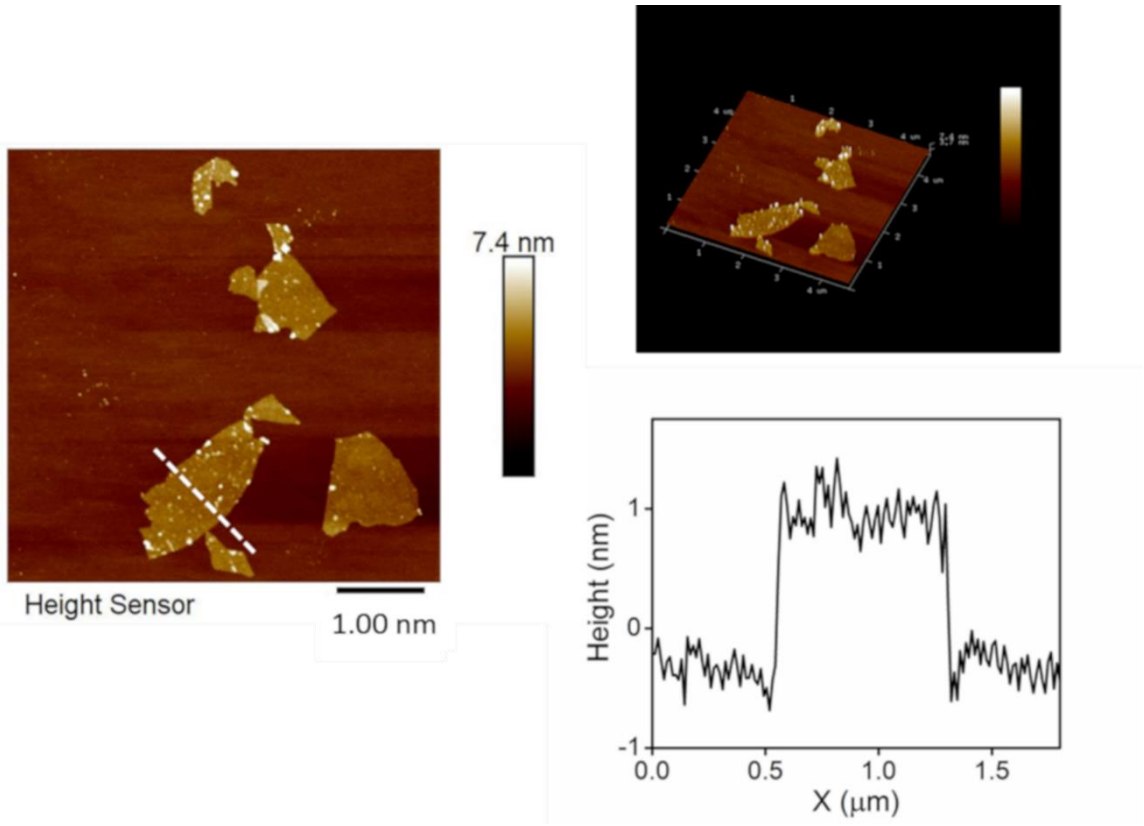


Figure I-13. Atomic force microscopy (AFM) image of MXene nanosheets. MXene nanosheets had a lateral size of around 1 μm and a thickness around 1.2 nm.

**Dissertation overview**

Silicon has a great potential to be used as anode material in lithium-ion battery. However, its three major intrinsic drawbacks of delamination, poor conductivity, and unstable solid electrolyte interphase (SEI) formation has set a roadblock to its commercialization. All these issues can be minimized by adding appropriate binder, conductive additives and, and electrode engineering to protect silicon particles from direct exposure to electrolyte. In this dissertation, we focused on these three parameters independently: (1) effect of density of functional groups on a binder and its architecture, (2) effect of conductive additives, and (3) effect of electrode architecture. Our aim was

not to make the best performing silicon anode, but instead it is to fundamentally understand the interaction between electrode materials and fill the gap in literature.

Chapter I provides a brief introduction to lithium-ion batteries and motivation to study silicon anodes, followed by challenges associated with it. Chapter I also introduces MXenes, which are newly developed, highly conductive, two dimensional transition metal based carbides. It details the synthesis and characterization methods.

Chapter II and Chapter III focusses on binder for silicon anode. Chapter II introduces a polymer named as poly(fluorene-*alt*-naphthalene diimide) (PFNDI). We investigated its performance as a binder in silicon anode. As a binder for silicon anodes, PFNDI exhibited poor performance, which was attributed to its poor adhesion to the silicon particles and its non-redox activity within silicon working potential window of 0.01 V to 1 V *vs.* $Li/Li^+$. Chapter III introduces a small molecule, tannic acid, as a binder for silicon anodes. Tannic acid is natural polyphenol with abundant hydroxyl groups. To the best of our knowledge, nobody has explored small molecules as binder for silicon anodes. We did an in-house comparison of tannic acid with other long chain, high molecular weight polymeric binders, such has poly(vinylidene fluoride), sodium alginate, and poly(acrylic acid). This comparison showed that along with density of functional groups, the binder architecture affects its performance; more branched the structure, better is the performance.

Chapter IV focusses on incorporation of MXenes into silicon anodes. In a typical silicon anode, additives (binder + conductive material) account for almost 30-60 wt% of the weight. These additives do not store energy and are regarded as “dead weight”.

Excessive dead weight dilutes the silicon active material which overall reduces the total energy density of the anode. To address this issue, we showed that the dead weight in silicon anode can be reduced by replacing the less conductive and hydrophobic Super P carbon black with much lower of amount of highly conductive and hydrophilic $Ti_3C_2T_x$ MXene nanosheets. We used only 4 wt% MXene nanosheets, 16 wt% water-based sodium alginate, and 80 wt% silicon. These electrodes demonstrated stable capacities around 900 $mAh/g_{Si}$ (720 $mAh/g_{total}$) at a high C-rate of 0.5 C, which was higher than a comparable electrode made in-house containing 4 wt% carbon black. The stable electrode performance even with a minimal MXene content is attributed to several factors: (1) highly uniform silicon electrodes due to the dispersibility of MXenes in water, (2) the high MXene aspect ratio that enables improved electrical connections, and (3) hydrogen bonding among MXenes, sodium alginate, and silicon particles.

Chapter V also focusses on mixing $Ti_3C_2T_x$ MXenes into silicon anodes, but in the form of a different electrode architecture. We used spray-dryer to wrap MXene nanosheets around silicon particles. Such an electrode architecture (crumpled electrode) minimized direct contact of silicon particles with electrolyte. An in-house comparison of crumpled architecture to the uncrumpled architecture revealed the advantages of effective wrapping of silicon particles by MXene nanosheets which minimized SEI formation and improved cycle life of anode. XPS and EIS analysis showed that large amounts of SEI had formed on cycled uncrumpled electrodes as compared to the crumpled electrodes.

Chapter VI summarizes the thesis work and proposes directions for future work.

## References


1. Reddy, M. V.; Mauger, A.; Julien, C. M.; Paolella, A.; Zaghib, K., Brief History of Early Lithium-Battery Development. *Materials (Basel)* **2020,** *13* (8), 1884.
2. Nitta, N.; Wu, F.; Lee, J. T.; Yushin, G., Li-ion Battery Materials: Present and Future. *Mater. Today* **2015,** *18* (5), 252-264.
3. Xu, K., Nonaqueous Liquid Electrolytes for Lithium-Based Rechargeable Batteries. *Chem. Rev.* **2004,** *104* (10), 4303–4418.
4. Bhatt, M. D.; O'Dwyer, C., Recent Progress in Theoretical and Computational Investigations of Li-Ion Battery Materials and Electrolytes. *Phys Chem Chem Phys* **2015,** *17* (7), 4799-844.
5. Winter, M.; Besenhard, J. O.; Spahr, M. E.; Novák, P., Insertion Electrode Materials for Rechargeable Lithium Batteries. *Adv. Mater.* **1998,** *10*, 725-763.
6. M.B., A., Intercalation Electrodes. In *Materials for Advanced Batteries*, Springer, Boston, MA: Boston, MA, 1980; Vol. 2, pp 145-161.
7. Goodenough, J. B.; Kim, Y., Challenges for Rechargeable Li Batteries†. *Chem. Mater.* **2010,** *22* (3), 587-603.
8. Wang, A.; Kadam, S.; Li, H.; Shi, S.; Qi, Y., Review on Modeling of the Anode Solid Electrolyte Interphase (SEI) for Lithium-Ion Batteries. *npj Comput. Mater.* **2018,** *4*, 15.
9. Costa, C. M.; Lee, Y.-H.; Kim, J.-H.; Lee, S.-Y.; Lanceros-Méndez, S., Recent Advances on Separator Membranes for Lithium-Ion Battery Applications: From Porous Membranes to Solid Electrolytes. *Energy Storage Materials* **2019,** *22*, 346-375.
10. Choi, S.; Wang, G., Advanced Lithium-Ion Batteries for Practical Applications: Technology, Development, and Future Perspectives. *Adv. Mater. Technol.* **2018,** *3* (9), 1700376.
11. Sun, Y.; Liu, N.; Cui, Y., Promises and Challenges of Nanomaterials for Lithium-Based Rechargeable Batteries. *Nat. Energy* **2016,** *1* (7), 16071.
12. Chen, Z.; Zhang, W.; Yang, Z., A Review on Cathode Materials for Advanced Lithium Ion Batteries: Microstructure Designs and Performance Regulations. *Nanotechnology* **2020,** *31* (1), 012001.
13. Mohamed, N.; Allam, N. K., Recent Advances in the Design of Cathode Materials for Li-ion Batteries. *RSC Adv.* **2020,** *10* (37), 21662-21685.
14. Breddemann, U.; Krossing, I., Review on Synthesis, Characterizations, and Electrochemical Properties of Cathode Materials for Lithium Ion Batteries. *ChemElectroChem* **2020,** *7*, 1389.
15. Feng, K.; Li, M.; Liu, W.; Kashkooli, A. G.; Xiao, X.; Cai, M.; Chen, Z., Silicon-Based Anodes for Lithium-Ion Batteries: From Fundamentals to Practical Applications. *Small* **2018,** *14* (8), 1702737.
16. Chae, S.; Ko, M.; Kim, K.; Ahn, K.; Cho, J., Confronting Issues of the Practical Implementation of Si Anode in High-Energy Lithium-Ion Batteries. *Joule* **2017,** *1* (1), 47-60.
17. Wen, C. J.; Huggins, R. A., Chemical Diffusion in Intermediate Phases in the Lithium-Silicon System. *J. Solid State Chem.* **1981,** *37* (3), 271-278.

18. C. van der Marel; G.J.B. Vinke; Lugt, W. v. d., The Phase Diagram of the System Lithium-Silicon. *Solid State Commun.* **1985,** *54* (11), 917-919.
19. Luo, W.; Chen, X.; Xia, Y.; Chen, M.; Wang, L.; Wang, Q.; Li, W.; Yang, J., Surface and Interface Engineering of Silicon-Based Anode Materials for Lithium-Ion Batteries. *Adv. Energy Mater.* **2017,** *7* (24), 1701083.
20. Gu, M.; He, Y.; Zheng, J.; Wang, C., Nanoscale Silicon as Anode for Li-Ion Batteries: The Fundamentals, Promises, and Challenges. *Nano Energy* **2015,** *17*, 366-383.
21. Ko, M.; Chae, S.; Cho, J., Challenges in Accommodating Volume Change of Si Anodes for Li-Ion Batteries. *ChemElectroChem* **2015,** *2* (11), 1645-1651.
22. Liu, X. H.; Wang, J. W.; Huang, S.; Fan, F.; Huang, X.; Liu, Y.; Krylyuk, S.; Yoo, J.; Dayeh, S. A.; Davydov, A. V.; Mao, S. X.; Picraux, S. T.; Zhang, S.; Li, J.; Zhu, T.; Huang, J. Y., In Situ Atomic-Scale Imaging of Electrochemical Lithiation in Silicon. *Nat. Nanotechnol.* **2012,** *7* (11), 749-56.
23. Chon, M. J.; Sethuraman, V. A.; McCormick, A.; Srinivasan, V.; Guduru, P. R., Real-Time Measurement of Stress and Damage Evolution During Initial Lithiation of Crystalline Silicon. *Phys. Rev. Lett.* **2011,** *107* (4), 045503.
24. Wan, W.; Zhang, Q.; Cui, Y.; Wang, E., First Principles Study of Lithium Insertion in Bulk Silicon. *J. Phys. Condens. Matter* **2010,** *22* (41), 415501.
25. Chan, M. K.; Wolverton, C.; Greeley, J. P., First Principles Simulations of the Electrochemical Lithiation and Delithiation of Faceted Crystalline Silicon. *J. Am. Chem. Soc.* **2012,** *134* (35), 14362-74.
26. Lee, S. W.; McDowell, M. T.; Choi, J. W.; Cui, Y., Anomalous Shape Changes of Silicon Nanopillars by Electrochemical Lithiation. *Nano Lett* **2011,** *11* (7), 3034-9.
27. Shenoy, V. B.; Johari, P.; Qi, Y., Elastic Softening of Amorphous and Crystalline Li–Si Phases With Increasing Li Concentration: A First-Principles study. *J. Power Sources* **2010,** *195* (19), 6825-6830.
28. Hertzberg, B.; Benson, J.; Yushin, G., Ex-Situ Depth-Sensing Indentation Measurements of Electrochemically Produced Si–Li Alloy Films. *Electrochem. Commun.* **2011,** *13* (8), 818-821.
29. Li, D.; Wang, Y.; Hu, J.; Lu, B.; Cheng, Y.-T.; Zhang, J., In Situ Measurement of Mechanical Property and Stress Evolution in a Composite Silicon Electrode. *J. Power Sources* **2017,** *366*, 80-85.
30. Sethuraman, V. A.; Chon, M. J.; Shimshak, M.; Srinivasan, V.; Guduru, P. R., In Situ Measurements of Stress Evolution in Silicon Thin Films During Electrochemical Lithiation and Delithiation. *J. Power Sources* **2010,** *195* (15), 5062-5066.
31. Zhao, K.; Wang, W. L.; Gregoire, J.; Pharr, M.; Suo, Z.; Vlassak, J. J.; Kaxiras, E., Lithium-Assisted Plastic Deformation of Silicon Electrodes in Lithium-Ion Batteries: A First-Principles Theoretical Study. *Nano Lett.* **2011,** *11* (7), 2962-7.
32. Sethuraman, V. A.; Srinivasan, V.; Bower, A. F.; Guduru, P. R., In Situ Measurements of Stress-Potential Coupling in Lithiated Silicon. *J. Electrochem. Soc.* **2010,** *157* (11), A1253.

33. Ryu, J. H.; Kim, J. W.; Sung, Y.-E.; Oh, S. M., Failure Modes of Silicon Powder Negative Electrode in Lithium Secondary Batteries. *Electrochem. Solid-State Lett.* **2004,** *7* (10), A306.
34. McDowell, M. T.; Lee, S. W.; Nix, W. D.; Cui, Y., 25th Anniversary Article: Understanding the Lithiation of Silicon and Other Alloying Anodes for Lithium-Ion Batteries. *Adv. Mater.* **2013,** *25* (36), 4966-85.
35. Liu, X. H.; Zhong, L.; Huang, S.; Mao, S. X.; Zhu, T.; Huang, J. Y., Size-Dependent Fracture of Silicon Nanoparticles During Lithiation. *ACS Nano* **2012,** *6* (2), 1522-1531.
36. Kwon, T. W.; Choi, J. W.; Coskun, A., The Emerging Era of Supramolecular Polymeric Binders in Silicon Anodes. *Chem. Soc. Rev.* **2018,** *47* (6), 2145-2164.
37. Wu, H.; Cui, Y., Designing Nanostructured Si Anodes for High Energy Lithium Ion Batteries. *Nano Today* **2012,** *7* (5), 414-429.
38. Peled, E.; Menkin, S., Review—SEI: Past, Present and Future. *J. Electrochem. Soc.* **2017,** *164* (7), A1703-A1719.
39. Naguib, M.; Kurtoglu, M.; Presser, V.; Lu, J.; Niu, J.; Heon, M.; Hultman, L.; Gogotsi, Y.; Barsoum, M. W., Two-Dimensional Nanocrystals Produced by Exfoliation of $Ti_3AlC_2$. *Adv. Mater.* **2011,** *23* (37), 4248-53.
40. Zhang, C.; Ma, Y.; Zhang, X.; Abdolhosseinzadeh, S.; Sheng, H.; Lan, W.; Pakdel, A.; Heier, J.; Nüesch, F., Two-Dimensional Transition Metal Carbides and Nitrides (MXenes): Synthesis, Properties, and Electrochemical Energy Storage Applications. *Energy Environ. Mater.* **2020,** *3* (1), 29-55.
41. Hui, X.; Ge, X.; Zhao, R.; Li, Z.; Yin, L., Interface Chemistry on MXene-Based Materials for Enhanced Energy Storage and Conversion Performance. *Adv. Funct. Mater.* **2020,** *30* (50), 2005190.
42. Xiong, D.; Li, X.; Bai, Z.; Lu, S., Recent Advances in Layered $Ti_3C_2T_x$ MXene for Electrochemical Energy Storage. *Small* **2018,** *14* (17), e1703419.
43. Naguib, M.; Mochalin, V. N.; Barsoum, M. W.; Gogotsi, Y., 25th Anniversary Article: MXenes: A New Family of Two-Dimensional Materials. *Adv. Mater.* **2014,** *26* (7), 992-1005.
44. Papadopoulou, K. A.; Chroneos, A.; Parfitt, D.; Christopoulos, S.-R. G., A Perspective on MXenes: Their Synthesis, Properties, and Recent Applications. *J. Appl. Phys.* **2020,** *128* (17), 170902.
45. Jun, B.-M.; Kim, S.; Heo, J.; Park, C. M.; Her, N.; Jang, M.; Huang, Y.; Han, J.; Yoon, Y., Review of MXenes as New Nanomaterials for Energy Storage/Delivery and Selected Environmental Applications. *Nano Research* **2018,** *12* (3), 471-487.
46. Alhabeb, M.; Maleski, K.; Anasori, B.; Lelyukh, P.; Clark, L.; Sin, S.; Gogotsi, Y., Guidelines for Synthesis and Processing of Two-Dimensional Titanium Carbide ($Ti_3C_2T_x$ MXene). *Chem. Mater.* **2017,** *29* (18), 7633-7644.
47. Shekhirev, M.; Shuck, C. E.; Sarycheva, A.; Gogotsi, Y., Characterization of MXenes at Every Step, from their Precursors to Single Flakes and Assembled Films. *Prog. Mater. Sci.* **2020**, 100757.

48. Zhao, X.; Vashisth, A.; Prehn, E.; Sun, W.; Shah, S. A.; Habib, T.; Chen, Y.; Tan, Z.; Lutkenhaus, J. L.; Radovic, M.; Green, M. J., Antioxidants Unlock Shelf-Stable $Ti_3C_2T$ (MXene) Nanosheet Dispersions. *Matter* **2019,** *1* (2), 513-526.

# CHAPTER II

# ANALYSIS OF POLY(FLUORENE-*ALT*-NAPTHALANE DIIMIDE) AS A BINDER FOR SILICON ANODES*

## Introduction

Silicon is an abundant, stable, and non-toxic material with a high specific capacity for lithium storage, and it is therefore an attractive target for use as an anode active material in lithium-ion batteries.[1] However, developing silicon anodes that outperform commercial graphite anodes is a significant challenge. While silicon has a specific capacity more than 10 times that of graphite, the silicon undergoes >300% volumetric expansion during lithiation which gives rise to several challenges such as pulverization, delamination , and unstable solid electrolyte interphase (SEI) formation.[2] The polymeric binder added to the silicon anode maintains the structure of the anode, serving as a glue to hold the various components of the electrode together and maintain contact with the current collector.[3] Binder contents of 3–5 wt% are used in commercial graphite electrodes, while silicon and alloy anode materials are typically fabricated with 10 wt% binder or more.[4] Therefore, in order to develop a superior silicon anode, irreversible capacity losses have to be reduced while also decreasing the content of polymer binders used.

Effective polymeric binders for silicon and other alloy anodes perform multiple functions. This includes maintaining strong adhesion to silicon, conductive additives, and the current collector, facilitating repeated and large volume changes of the silicon particles, and enhancing the transport of charges or ions through the electrode.[5]

Redox active polymers (RAPs) are a class of polymers that store energy by a reversible chemical conversion mechanism called doping.[6, 7] RAPs offer several advantages such as excellent electrode processability, simple redox reaction, and fine-tuning of electrochemical properties by modifying the chemical structure.[8] There are two main types of RAPs; p-type RAP that becomes positively charged upon oxidation and doping with anions and the n-type RAP that becomes negatively charged upon reduction and doping with cations.[9] n-Type RAPs are an interesting class of polymers that can be potentially used as binders for silicon anode. Liu *et al.* synthesized poly(9,9-dioctylfluorene-co-fluorenone-co-methylbenzoic ester) (PFFOMB) by adding carbonyl (C=O) and methylbenzoic ester (MB) functional groups to a conjugated polyfluorene (PF) unit[10] for use as an n-type conductive binder in silicon electrodes. The carbonyl group lowered the lowest unoccupied molecular orbital (LUMO) of the PFFOMB polymer, which improved the ability of PFFOMB to be reduced. These results highlight the growing interest in redox-active conjugated polymers in which a redox-active group reversibly stores energy and a conjugated unit assist in electron conduction.

One such polymer with both redox-active and conjugated units is poly(fluorene-*alt*-napthalene diimide) (PFNDI) (Figure II-1a). Although not yet studied in the context of energy storage, PFNDI is of interest because of the dual nature of the fluorene and naphthalene diimide units. The NDI unit accepts 2 $Li^+$ ions per repeat unit at a potential of ~2.5 V *vs.* $Li/Li^+$ and exhibits battery-like behavior– Figure II-1b.[11-14] However polyNDIs are generally insulating, so large amounts of carbon are required to facilitate the energy storage. On the other hand, PFs have conductivities around $10^{-4}$-$10^{-2}$ S/cm (when

doped with a base such as potassium or tert-butoxide),[15] and modest redox activity above 4 V *vs.* Li/Li$^+$.[16-18] As an alternating co-polymer, PFNDI has a LUMO level of -3.61 eV and a highest occupied molecular orbital (HUMO) level of -5.93 eV, and this high HOMO energy level is indicative of its possible stability in a reducing environment.[6, 13]

Here, we investigated n-type PFNDI as a binder for silicon anode. Our approach used cyclic voltammetry (CV), galvanostatic charge-discharge (GCD), and electrochemical impedance spectroscopy (EIS). We used PFNDI as a binder for silicon anodes and characterized the battery cycling performance.

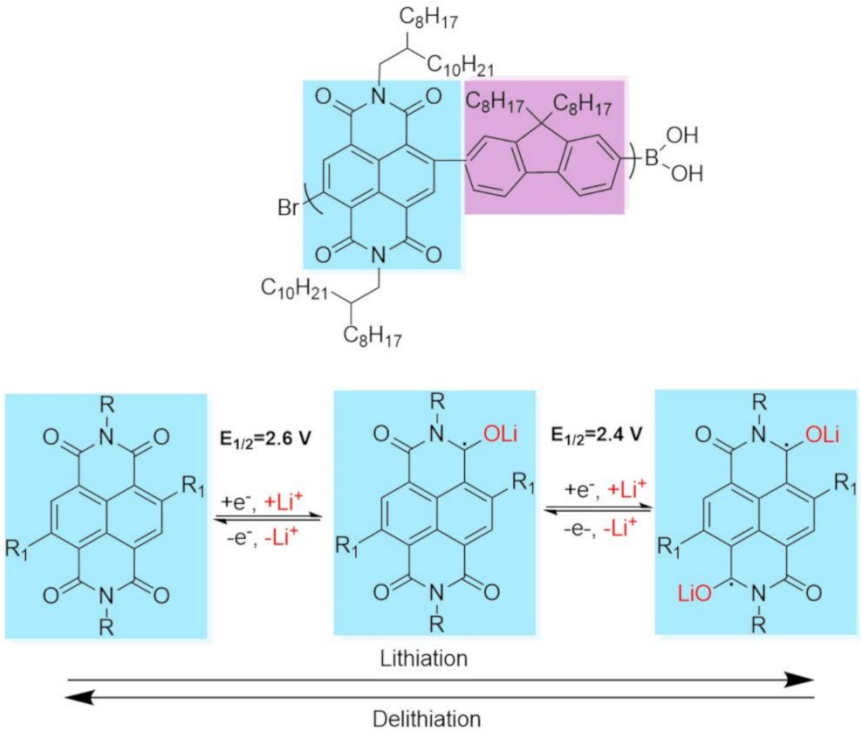


Figure II-1. (a) Structure of poly(fluorene-*alt*-naphthalene diimide) (PFNDI) showing the redox active NDI unit (blue) and the conjugated fluorene unit (purple). (b) Doping of a naphthalene diimide (NDI) unit with Li$^+$ ions. Upon the first reduction, one carbonyl oxygen is doped with a Li$^+$ ion, and upon the second reduction, a second carbonyl oxygen is doped. The reverse process takes place during oxidation. Voltages are *vs.* Li/Li$^+$.

**Materials**

For the PFNDI synthesis, 9,9-dioctylfluorene-2,7-diboronic acid bis(1,3-propanediol) ester and (4,9-dibromo-2,7-bis(2-octyldodecyl)benzo[lmn][3,8]phenanthroline-1,3,6,8 (2H,7H)-tetraone were acquired from Sigma Aldrich and SunaTech Inc. Tetraethylammonium hydroxide, 20 wt% solution in water was acquired form ACROS organics. Indium tin oxide (ITO) coated glass substrates were purchased from Delta Technologies (7 mm x 50 mm x 0.7 mm, resistance 5-10 Ω, one side coated). Dichloromethane, isopropyl alcohol, acetone, and anhydrous chloroform were purchased from VWR. Super P carbon black (CB) (0.04 µm particle size, 62 $m^2/g$ surface area) and stainless-steel substrates (15.5 mm diameter x 0.2 mm thick) were purchased from MTI corporation. Anhydrous lithium perchlorate ($LiClO_4$), anhydrous acetonitrile (MeCN), 1-methyl-2-pyrrolidinone (NMP) and the electrolyte composed of 1 M lithium hexafluorophosphate ($LiPF_6$) in ethylene carbonate:diethylene carbonate (EC:DEC) (1:1 v/v) were purchased from Sigma Aldrich. The reference electrode used was a saturated silver/silver chloride (Ag/AgCl) electrode purchased from Pine Research Instrumentation. Lithium metal foil (0.75 mm thick x 19 mm wide) and Aliquat 336 were purchased from Alfa Aesar. Polypropylene separator (Celgard 3501) (19 mm diameter x 0.025 mm thick) was purchased from Celgard. Silicon nanoparticles (98+% purity, 20-30 nm size, 80-120 $m^2/g$ surface area) were purchased from US Research Nanomaterials.

## Methods

### *PFNDI polymer characterization*

Polymer molecular weights and polydispersities were determined using an Agilent 1200 module equipped with three PSS SDV columns in series (100, 1000, and 10,000 Å pore sizes), an Agilent variable wavelength UV/vis detector, a Wyatt technology HELEOS II multiangle laser light scattering (MALLS) detector ($\lambda$ = 658 nm), and a Wyatt Technology Optilab reX RI detector. This system enables GPC with simultaneous refractive index (GPC-RI), UV/vis (GPC-UV/vis), and MALLS detection. THF was used as the mobile phase at a flow rate of 1 ml/min at 40 °C. Proton-NMR (1H NMR) spectra were recorded using tetramethylsilane as the internal standard in ($d_3$-chloroform) $CDCl_3$ on a 400 MHz Bruker multinuclear spectrometer. Samples were placed in 5 mm outer diameter tubes and the concentration was ~10 mg/ml.

### *Silicon anode preparation*

To make a silicon electrode with PFNDI as the conductive binder, 65 wt% silicon nanoparticles, 15 wt% PFNDI, and 20 wt% CB were dispersed in NMP by sonicating the mixture for 30 minutes to form a slurry. This slurry was then drop-cast onto a stainless steel substrate, dried in air, and then dried in a vacuum oven at 120 °C for 3-4 h to remove the residual NMP. The active material loading of Si/PFNDI/CB electrode was around 0.3-0.4 mg/cm$^2$ with total areal loading of 0.5 mg/cm$^2$.

### *PFNDI electrode preparation*

ITO-coated glass and stainless-steel substrates were cleaned by sonicating sequentially in dichloromethane, isopropyl alcohol, distilled water, and acetone. They

were then dried using nitrogen gas. Furthermore, the ITO-coated glass substrates were cleaned using ozone plasma treatment (Harrick PDC-32G) for 20 minutes. PFNDI was dissolved in chloroform (2 mg/ml) and drop-cast on the conducting side of cleaned ITO or the stainless-steel substrate to yield an active material loading of approximately 0.3–0.4 mg/cm$^2$. The PFNDI polymer electrode was dried in a vacuum oven at 75 °C for 6 h to remove residual chloroform.

***Electrochemical characterization***

A two-electrode half-cell was also used to study Si/PFNDI/CB=65/15/20 working electrodes with lithium metal as the counter and reference electrodes, Celgard separators, and 1 M $LiPF_6$ in EC:DEC (1:1 v/v) as the electrolyte. The Solartron Potentiostat/Galvanostat Instrument (Solartron, Electrochemical Interface 1287) was used to perform cyclic voltammetry at 1 mV/s and galvanostatic cycling at 0.1 C. For these experiments, the C-rate was calculated using the theoretical capacity of silicon (3579 mAh/g).

For the PFNDI/silicon polymer anode, the voltage window was 0.01 V to 1 V *vs*. $Li/Li^+$, and a two-electrode half-cell was used. PFNDI coated stainless-steel was used as the working electrode and lithium metal was used as the counter and reference electrode. Celgard separators were used between these two electrodes and 0.5 M $LiClO_4$ in MeCN was used as the electrolyte. The Solartron instrument was used to conduct cyclic voltammetry at 1 mV/s and galvanostatic cycling at different C-rates (0.1 C, 0.2 C, 0.5 C, and 1 C). A Gamry Potentiostat/Galvanostat Instrument (Gamry Interface 1000, Gamry

Instruments) was used to perform electrochemical impedance spectroscopy (EIS) with 50 mV amplitude and 100 kHz to 5 mHz frequency range.

A three-electrode electrochemical cell was used to perform electrochemical measurements on PFNDI electrodes. PFNDI drop-cast onto ITO-coated glass was the working electrode, Ag/AgCl was the reference electrode, platinum wire was the counter electrode, and 0.5 M $LiClO_4$ in MeCN was used as the electrolyte.

**Results and discussion**

Synthesis of PFNDI was adapted from a prior report.[19] PFNDI as-synthesized had a molecular weight of approximately 41.0 kDa and a dispersity index of 1.7. We added n-type PFNDI as a polymeric binder in silicon anode to evaluate its performance as a conductive binder. The electrode was prepared following a mass ratio of Si/PFNDI/CB = 65/15/20 wt% in NMP, which was drop-cast onto stainless steel. This electrode was used as the working electrode in a two-electrode half-cell with lithium metal as the counter/reference electrode and 1 M $LiPF_6$ in EC:DEC (1:1 v/v) as the electrolyte. Figure II-2a shows the cycling performance of the silicon electrode at 0.1 C for 10 cycles and it can be observed that the capacity of the silicon electrode is very low (10 mAh/g) as compared to theoretical capacity of silicon anode (3579 mAh/g). The current magnitude in the cyclic voltammogram plot at 0.1 mV/s (Figure II-2b) was also low which implies that the extent of electrochemical reaction was low. Also, the cell failed within a few galvanostatic cycles, which implies that the electrode suffered from volume changes attributed to silicon.

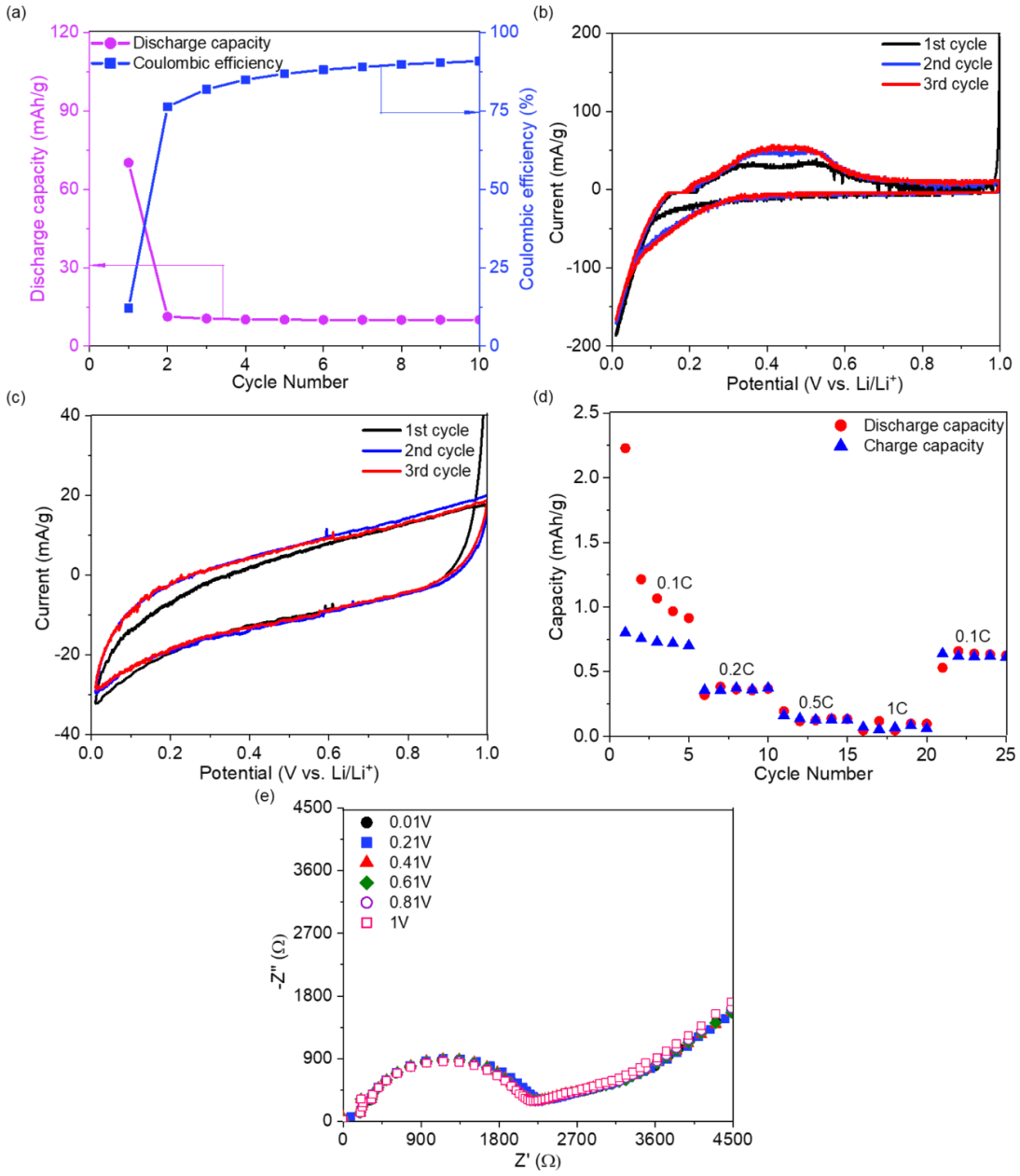


Figure II-2. (a) Galvanostatic charge-discharge and Coulombic efficiency of Si/PFNDI/CB=65/15/20 wt% electrode at 0.1 C. (b) Cyclic voltammogram of the same electrode at 0.1 mV/s for three cycles. (c) Cyclic voltammogram of pure PFNDI electrode at 1 mV/s for 3 cycles and (d) galvanostatic charge-discharge at difference C-rates from 0.1 C to 1 C (5 cycles each). (e) Nyquist plot obtained via electrochemical impedance spectroscopy (EIS) analysis of pure PFNDI at different potentials in 0.01 V to 1 V *vs.* $Li/Li^+$. The AC amplitude was 50 mV. The frequency range was from 100 kHz to 5 mHz. All tests were carried out in 0.01 V to 1 V *vs.* $Li/Li^+$ voltage window.

To analyze the reasons behind failure of battery made using Si/PFNDI/CB electrode, we did analysis on the pure PFNDI binder itself. For that, we drop-cast PFNDI onto stainless-steel substrate and used that as a working electrode in a half-cell assembly vs lithium metal. We observed no redox peaks in the cyclic voltammogram at 1 mV/s, which implies that PFNDI was not redox-active in the silicon working voltage window of 0.01-1 V vs. $Li/Li^+$ (Figure II-2c). We also did rate performance study on pure PFNDI in silicon working volage window and it showed very poor capacities (Figure II-2d). EIS analysis showed that the PFNDI had very high charge transfer resistance (diameter of the depressed semi-circle) and this could be a reason for poor electrode performance (Figure II-2e). Thus, we showed that PFNDI is not redox-active in 0.01-1 V *vs.* $Li/Li^+$ window, which made it highly resistive that overall led to poor performance as a binder in silicon anode. Also, PFNDI did not possess the essential hydrogen bonding functional groups that improve the binding ability to silicon, and thus PFNDI did not do failed to main electrode's structural integrity during volume changes. Lastly, we observed non-unform distribution of PFNDI binder in silicon anode after drop-casting probably due to aggregation of binder.

We further analyzed pure PFNDI in detail to evaluate its redox-activity. For that, we drop-cast PFNDI on ITO substrate to use as a working electrode in a 3-electrode assembly with Ag/AgCl as referee electrode, Pt wire as counter electrode, and 1 M $LiClO_4$ in acetonitrile as electrolyte. Figure II-3 shows a cyclic voltammogram at 1 mV/s with three different voltage regions explored: low voltage region (LVR, 1.7 V to 3.7 V), a high voltage region (HVR, 3.7 V to 5.2 V), and the full voltage region (FVR, 1.7 V to 5.2 V). The reference electrode was Ag/AgCl, and the electrolyte was 0.5 M $LiClO_4$ in

acetonitrile. Krtil and Novak showed that $LiClO_4$ in acetonitrile was stable up to 5.5 V *vs.* $Li/Li^+$.[20] The electrochemical activity appears in the LVR and FVR scans, with the LVR showing higher specific current than the FVR. There is not remarkable electrochemical activity in the HVR scan. Two pairs of peaks occurring at different potentials were observed, indicating the presence of two redox reactions (Figure II-1b). Upon the first reduction (2.53 V), a carbonyl group on the NDI unit gains an electron; for charge neutrality a $Li^+$ cation dopes the negatively charged NDI unit. As the voltage decreases further, a second reduction occurs at the NDI unit (2.32 V); resulting in another carbonyl group's reduction and doping with $Li^+$. The peak current of the second reduction peak is notably less than that of the first reduction peak. When the potential is reversed, oxidation and first (de)lithiation of the NDI unit occurs (2.54 V). Upon increasing the potential further, a second oxidation event occurs at the NDI unit (2.75 V).This showed that PFNDI was redox-active within potential window of 1.7-5.2 V *vs.* $Li/Li^+$.

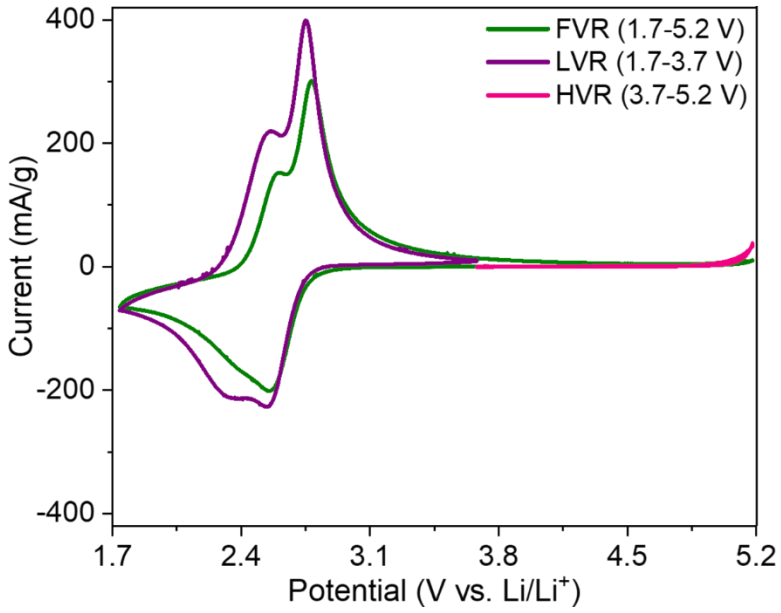


Figure II-3. Cyclic voltammograms of PFNDI at scan rate of 1 mV/s in various voltage windows: low voltage region (LVR, 1.7 V to 3.7 V), high voltage region (HVR, 3.7 V to 5.2 V), and the full voltage region (FVR, 1.7 V to 5.2 V). Tests were conducted in a three-electrode cell, with PFNDI as the working electrode, Ag/AgCl as the reference electrode, platinum wire as the counter electrode, and 0.5 M lithium perchlorate ($LiClO_4$) in acetonitrile as the electrolyte.

Overall, n-type PFNDI was a poor binder for silicon as compared to other polyfluorene-type binders[10] poly(9,9-dioctylfluorene-co-fluorenone) (PFFO) and PFFOMB.[10] Here, the poor performance of PFNDI as a binder for silicon may be attributed to the poor adhesion of the PFNDI to the silicon particles.[2, 21] Therefore, PFNDI is more suitable for use on its own or blended with carbon black as an n-type polymeric electrode.

**Conclusions**

N-type poly(fluorene-*alt*-naphthalene diimide) (PFNDI) was synthesized via Suzuki coupling and its performance as a binder in silicon anode was investigated. As a

binder for silicon anodes, PFNDI exhibited poor performance, which was attributed to its poor adhesion to the silicon particles and its non-redox activity within silicon working potential window of 0.01 V to 1 V *vs.* $Li/Li^+$. Instead, PFNDI was redox active within 1.7-5.2 V *vs.* $Li/Li^+$. Future work should address these issues by increasing the molecular weight and/or installing adhesive groups, such as hydroxyl groups. PFNDI's reversible charge storage points to its possible application as a battery anode either by itself or with carbon black as an additive.

**References**


1. Casimir, A.; Zhang, H.; Ogoke, O.; Amine, J. C.; Lu, J.; Wu, G., Silicon-Based Anodes for Lithium-Ion Batteries: Effectiveness of Materials Synthesis and Electrode Preparation. *Nano Energy* **2016,** *27*, 359-376.
2. Erk, C.; Brezesinski, T.; Sommer, H.; Schneider, R.; Janek, J., Toward Silicon Anodes for Next-Generation Lithium Ion Batteries: A Comparative Performance Study of Various Polymer Binders and Silicon Nanopowders. *ACS Appl. Mater. Interfaces* **2013,** *5* (15), 7299-307.
3. Kwon, T. W.; Choi, J. W.; Coskun, A., The Emerging Era of Supramolecular Polymeric Binders in Silicon Anodes. *Chem. Soc. Rev.* **2018,** *47* (6), 2145-2164.
4. Chou, S. L.; Pan, Y.; Wang, J. Z.; Liu, H. K.; Dou, S. X., Small Things Make a Big Difference: Binder Effects on the Performance of Li and Na Batteries. *Phys. Chem. Chem. Phys.* **2014,** *16* (38), 20347-59.
5. Miranda, A.; Sarang, K.; Gendensuren, B.; Oh, E.-S.; Lutkenhaus, J.; Verduzco, R., Molecular Design Principles for Polymeric Binders in Silicon Anodes. *Mol. Syst. Des. Eng.* **2020,** *5* (4), 709-724.
6. Mike, J. F.; Lutkenhaus, J. L., Recent Advances in Conjugated Polymer Energy Storage. *J. Polym. Sci., Part B: Polym. Phys* **2013,** *51* (7), 468-480.
7. Novák, P.; Müller, K.; Santhanam, K. S. V.; Haas, O., Electrochemically Active Polymers for Rechargeable Batteries. *Chem. Rev.* **1997,** *97*, 207-281.
8. Kim, J.; Kim, J. H.; Ariga, K., Redox-Active Polymers for Energy Storage Nanoarchitectonics. *Joule* **2017,** *1* (4), 739-768.
9. Sarang, K. T.; Miranda, A.; An, H.; Oh, E.-S.; Verduzco, R.; Lutkenhaus, J. L., Poly(fluorene-alt-naphthalene diimide) as n-Type Polymer Electrodes for Energy Storage. *ACS Appl. Polym. Mater.* **2019,** *1* (5), 1155-1164.
10. Liu, G.; Xun, S.; Vukmirovic, N.; Song, X.; Olalde-Velasco, P.; Zheng, H.; Battaglia, V. S.; Wang, L.; Yang, W., Polymers with Tailored Electronic Structure for High Capacity Lithium Battery Electrodes. *Adv. Mater.* **2011,** *23* (40), 4679-83.

11. Liang, Y.; Chen, Z.; Jing, Y.; Rong, Y.; Facchetti, A.; Yao, Y., Heavily n-Dopable pi-Conjugated Redox Polymers with Ultrafast Energy Storage Capability. *J. Am. Chem. Soc.* **2015,** *137* (15), 4956-9.
12. Han, X.; Chang, C.; Yuan, L.; Sun, T.; Sun, J., Aromatic Carbonyl Derivative Polymers as High-Performance Li-Ion Storage Materials. *Adv. Mater.* **2007,** *19* (12), 1616-1621.
13. Song, Z.; Zhan, H.; Zhou, Y., Polyimides: Promising Energy-Storage Materials. *Angew. Chem., Int. Ed. Engl.* **2010,** *49* (45), 8444-8.
14. Xu, F.; Jin, S.; Zhong, H.; Wu, D.; Yang, X.; Chen, X.; Wei, H.; Fu, R.; Jiang, D., Electrochemically Active, Crystalline, Mesoporous Covalent Organic Frameworks on Carbon Nanotubes for Synergistic Lithium-Ion Battery Energy Storage. *Sci. Rep.* **2015,** *5*, 8225.
15. Ranger, M.; Leclerc, M., New Base-Doped Polyfluorene Derivatives. *Macromolecules* **1999,** *32*, 3306-3313.
16. Xu, J.; Zhang, Y.; Hou, J.; Wei, Z.; Pu, S.; Zhao, J.; Du, Y., Low Potential Electrosyntheses of Free-Standing Polyfluorene Films in Boron Trifluoride Diethyl Etherate. *Eur. Polym. J.* **2006,** *42* (5), 1154-1163.
17. Calzolari, A.; Vercelli, B.; Ruini, A.; Virgili, T.; Pasini, M., Fluorine-Induced Enhancement of the Oxidation Stability and Deep-Blue Optical Activity in Conductive Polyfluorene Derivatives. *J. Phys. Chem. C* **2013,** *117* (50), 26760-26767.
18. Dong, B.; Song, D.; Zheng, L.; Xu, J.; Li, N., Electrosynthesis of Polyfluorene in an Ionic Liquid and Characterization of its Stable Electrocatalytic Activity for Formic Acid Oxidation. *J. Electroanal. Chem.* **2009,** *633* (1), 63-70.
19. Zhou, E.; Cong, J.; Zhao, M.; Zhang, L.; Hashimoto, K.; Tajima, K., Synthesis and Application of Poly(fluorene-alt-naphthalene diimide) as an n-Type Polymer for All-Polymer Solar Cells. *Chem. Commun.* **2012,** *48* (43), 5283-5.
20. Krtil, P.; Kavan, L.; Novak, P., Oxidation of Acetonitrile-Based Electrolyte Solutions at high potentials. *J. Electrochem. Soc.* **1993,** *140*, 3390-3395.
21. Kierzek, K., Influence of Binder Adhesion Ability on the Performance of Silicon/Carbon Composite as Li-Ion Battery Anode. *J. Mater. Eng. Perform.* **2016,** *25* (6), 2326-2330.

# CHAPTER III

# TANNIC ACID AS A SMALL MOLECULE BINDER FOR SILICON ANODES*

## Introduction

Increasing energy demands have advanced the development of high energy density lithium-ion batteries.[1, 2] Lithium-ion batteries have been used as energy storage devices in a wide variety of applications, ranging from consumer electronics to industrial solar/wind energy storage, and electric vehicles.[3] Several electrode materials for lithium-ion batteries have been studied previously,[4-6] however the need to improve the cost, performance, and energy density of lithium-ion batteries has spurred the interest in developing stable, high capacity electrode materials.[7] Anode materials that can form intermetallic compounds with lithium have attracted attention due to their much higher capacities relative to conventional graphite anodes.[8] Specifically, silicon holds great promise due to its low discharge potential, abundance, and high theoretical capacity of 3500 mAh/g (ten times higher than that of graphite).[9] However, silicon has >300 % volumetric expansion upon lithiation and low electrical conductivity.[10] The limited conductivity can be addressed through conductive additives,[11, 12] but the volumetric expansion during lithiation generates stresses in the electrode that result in capacity fade from electrode fragmentation and loss of electrical contact.[10, 13]

To mitigate this issue, significant research efforts have focused on designing nanostructured silicon particles[14] and synthesizing carbon/Si composites.[15] However, these methods require multi-step processing conditions and are thus expensive or

*Reprinted with permission from "Tannic Acid as a Small Molecule Binder for Silicon Anodes", by Kasturi Sarang, Xiaoyi Li, Andrea Miranda, Tanguy Terlier, Eun-Suok Oh, Rafael Verduzco, Jodie L Lutkenhaus, ACS Appl. Energy Mater., 2020, 3, 7, 6985-6994. Copyright (2020) American Chemical Society.

complex.[16] One alternative route is to develop polymeric binders that can accommodate silicon's volume changes. Silicon anodes typically contain a binder that adheres the electrode components together, including the silicon particles, conductive additives, and current collector.[17] Poly(vinylidene fluoride) (PVDF) is a commonly used polymeric binder, but it has poor adhesion to silicon due to weak van der Waals forces, which lead to poor battery cycle life.[18, 19] Also, PVDF (along with many other binders) require organic solvents for processing, which can lead to detrimental environmental impacts relative to water-based binders for silicon anodes.[19] A systematic study by Kwon *et al*., demonstrated that binder performance depends on the type of chemical bond formed with the silicon surface and that strong non-covalent interactions, such as hydrogen bonding, are preferred.[20] Examples of such water-based binders include poly(acrylic acid),[21, 22] carboxymethyl cellulose,[23] alginate,[24] and galactomannans.[16] Not only the type of chemical bond, but also the polymer architecture, affects the binder performance for silicon anodes. Specifically, a branched structure offered an advantage over a linear structure by providing more anchors to the silicon nanoparticle surface.[17] Researchers have explored hyperbranched polymers,[25, 26] graft polymers,[27, 28] and network polymers.[29, 30] Small molecules such as tannic acid (TA) have not been explored as binders for silicon anodes. Tannic acid is a water soluble natural polyphenol that contains multiple 3,4,5-trihydroxybenzoyl (galloyl) groups arranged in a branch-like architecture as shown in Figure III-1a.[31] This structure provides a number of groups that potentially bond with the silicon surface.

Motivated by this, we sought to understand how a small molecule with hydrogen bonding functional groups, specifically TA, would behave as a binder for silicon anodes. We hypothesized that evaluation of TA binders would isolate the effects of hydrogen

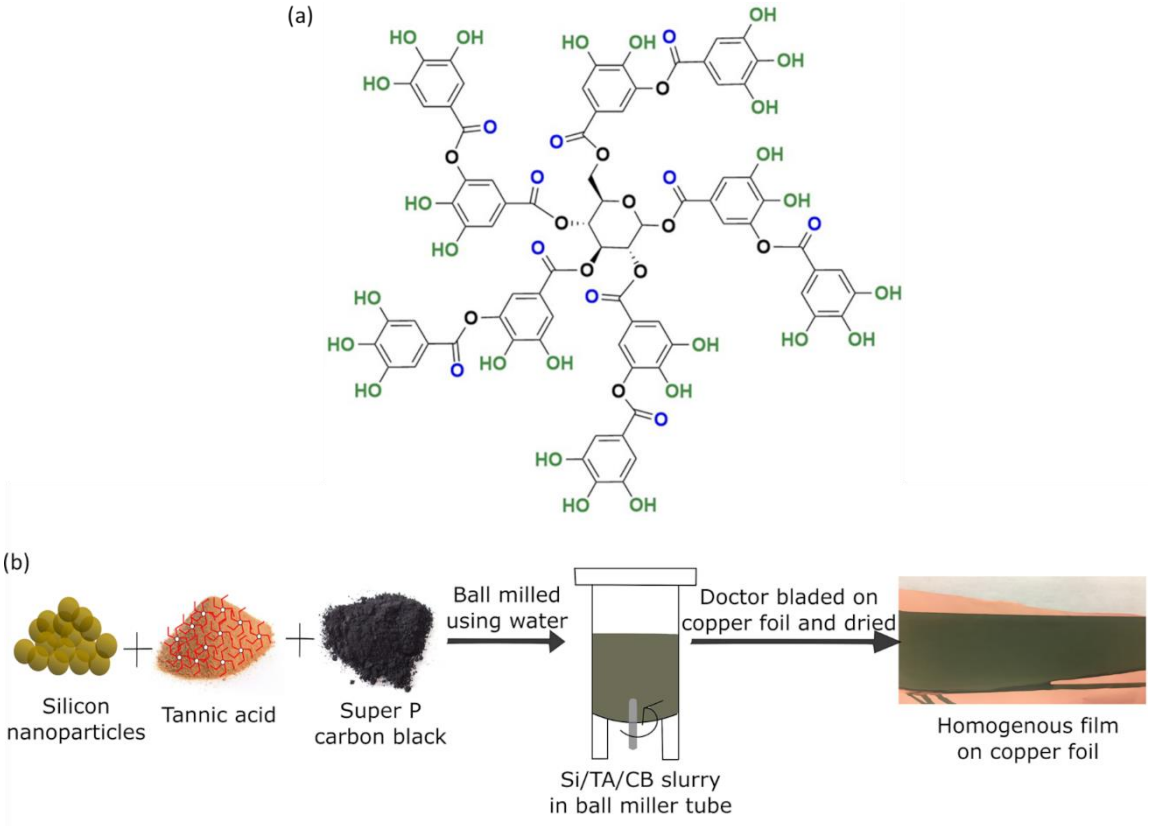


Figure III-1. (a) Molecular structure of tannic acid (TA). (b) Schematic for preparation of homogeneous composite silicon electrodes.

bonding without the effects of large-scale particle-to-particle bridging caused by high molecular weight polymers. Tannic acid itself has been explored as an anode material, but not as a binder for silicon. Xu *et al*. demonstrated that TA's abundant oxygen-containing functionalities could store charge via $Li^+$ doping around 1.1-1.5 V *vs.* $Li/Li^+$ with a discharge capacity of 100 mAh/g.[32] Researchers have also explored the hydrogen bonding

capabilities of TA with different polymers.[33, 34] Recently, Zhang *et al*., demonstrated a 3D cross-linked tannic acid/polyethylene oxide binder for a sulfur cathodes.[35]

Here we present small molecule tannic acid (1700 g/mol) as a water-processible binder for silicon anodes. Our approach used cyclic voltammetry, galvanostatic cycling, and electrochemical impedance spectroscopy (EIS). We first performed cyclic voltammetry on the electrode to evaluate reversible lithiation of the silicon particles. Galvanostatic cycling and rate capability experiments were conducted to determine cycling stability and performance. Scanning electron microscopy (SEM) captured the changes in the morphology upon cycling. Time-of-flight ion mass spectroscopy (ToF-SIMS) and X-ray photo electron spectroscopy (XPS) was performed to characterize solid electrolyte interphase formation (SEI). EIS related electrode impedance to the electrode's performance. Overall, we show that tannic acid's abundant hydroxyl groups can effectively bond with silicon nanoparticles to maintain a cohesive electrode that withstands repeated cycling. This is unique because most other binders are high molecular weight polymers and some require organic solvents for processing.

**Materials**

Silicon nanoparticles (98+ % purity, 20-30 nm size, 80-120 $m^2/g$ surface area) were purchased from US Research Nano Materials. Tannic acid (TA) (1701.2 g/mol), 1 M lithium hexafluorophosphate ($LiPF_6$) in ethylene carbonate (EC):diethyl carbonate (DEC) (1:1) v/v, and fluoroethylene carbonate (FEC) were purchased from Sigma Aldrich. Lithium foil (0.75 mm thick x 19 mm wide) and fluoroethylene carbonate (FEC) were purchased from Alfa Aesar. Super P carbon black (CB) (0.04 µm particle size, 62 $m^2/g$

surface area) and copper foil (length x width x thickness = 170 m x 280 mm x 9 μm) were purchased from MTI corporation. Polypropylene separator (19 mm diameter x 0.025 mm thick) was purchased from Celgard

**Methods**

***Silicon anode preparation***

To make electrodes, silicon nanoparticles (Si), TA, and CB with a mass ratio of Si:TA:CB = 70:10:20 were ball milled together in water to form a homogenous slurry. The resulting slurry was doctor bladed onto copper foil using an automated film applicator (Elcometer 4340 Automatic applicator) with a blade thickness of 200 μm. (Figure III-1b) Electrodes of two other compositions (Si/TA/CB=60/20/20 and Si/TA/CB=80/10/10 by mass) were also fabricated for an initial screening experiment using the slurry casting method. Blade thicknesses of 220 μm and 180 μm were used to cast Si/TA/CB=60/20/20 and Si/TA/CB=80/10/10 electrodes, respectively. These electrodes were air dried at room temperature for 1 h, then at 40 °C overnight, followed by vacuum drying at 80 °C for 3 – 4 h. After drying, 16 mm electrodes were punched. The electrode thickness after drying was measured using Zetasizer (TESA μ-Hite) instrument. The loading of active material in all electrodes was controlled to around 0.7 – 0.8 mg/cm$^2$.

***Scanning electron microscopy (SEM) and energy dispersive X-ray spectroscopy (EDS)***

SEM was carried out on a JEOL JSM SEM equipment with an accelerating voltage of 5 kV and a working distance of 15 mm. The samples before cycling were dried in vacuum oven at room temperature for 24 h before analysis; and the samples after cycling were washed with dichloromethane to remove excess lithium salt. They were then dried

inside the glovebox for two days followed by drying in vacuum oven at room temperature for one day. EDS was performed on JEOL JSM SEM with an accelerating voltage of 20 kV and a working distance of 8 mm. The data acquisition and data processing for EDS was done using INCA software. For the microscope setup, the probe current and process time were optimized to obtain a deadtime of approximately 45 %. For quant optimization, the measurements were done on a reference copper tape which was placed besides the sample on sample holder. Different homogenous rectangular areas on the samples were selected to acquire the data. All these steps were done to ensure that process parameters were optimized to get a good quantification of elements present in the sample.

***Time-of-flight (ToF-SIMS) ion mass spectroscopy***

Positive and negative high mass resolution spectra were performed using a ToF-SIMS NCS instrument, which combines a ToF.SIMS5 instrument (ION-ToF GmbH, Münster, Germany) and an in-situ scanning probe microscope (NanoScan, Switzerland) at Shared Equipment Authority from Rice University. A bunched 30 keV $Bi^{3+}$ ions (with a measured current of 0.2 pA) was used as primary probe for analysis (scanned area 100 × 100 $\mu m^2$) with a raster of 128 × 128 pixels. A charge compensation with an electron flood gun has been applied during the analysis. An adjustment of the charge effects has been operated using a surface potential of -6 V and an extraction bias of 0 V for the positive polarity and a surface potential of 0 V and an extraction bias of -20 V for the negative polarity. The cycle time was fixed to 90 µs (corresponding to m/z = 0 – 737 a.m.u mass range).

***X-ray photoelectron spectroscopy***

X-ray photoelectron spectroscopy (XPS) was performed using Omicron ESCA Probe (Omicron Nanotechnology) with a monochromated Mg Ka radiation (hm = 1253.6 eV). XPS survey scans were performed with an analyzer pass energy of 100-1100 eV (1.0 eV steps, 50 ms dwell time), while high resolution scans of carbon (C 1s) and silicon (Si 2p) were performed with a pass energy of 150 eV (0.05 eV steps, 200 ms dwell time). All spectra were calibrated with the C 1s photoemission peak for $sp^2$-hybridized carbons at 284.5 eV. Curve fitting (using CasaXPS software) was conducted using a Gaussian-Lorentzian peak shape after Shirley-type background correction.

***Electrochemical characterization***

For electrochemical characterization, cells were assembled inside an argon-filled glovebox (MBraun, Labstar 1200). 16 mm punched electrodes were used as working electrodes and lithium metal foil (16 mm) was employed as the counter/reference electrode. Two Celgard polypropylene discs (19 mm diameter, 25 µm thick) were used as separators. 1 M $LiPF_6$ in EC:DEC with 10 wt% FEC was used as an electrolyte in the battery. Galvanostatic charge-discharge, rate capability, and cyclic voltammetry tests were performed using an Arbin (Arbin Instruments, HPT-100mA). Electrochemical properties were measured within a voltage range of 0.01 V to 1 V *vs.* $Li/Li^+$, and the charge-discharge currents were calculated using the theoretical capacity of silicon (3579 mAh/g). For each galvanostatic cycling test, the electrodes were cycled in constant current (CC) – constant voltage (CV) mode for the first 5 cycles. In the CC–CV mode, the electrodes were first lithiated at 0.1 C until the potential reached 0.01 V (CC mode) and then the potential was

held constant at 0.01 V until the current had decayed to 0.01 C. After the first 5 cycles, the electrodes were cycled in constant current mode at 0.5 C for 200 cycles. After the first 5 cycles, the electrodes were cycled in constant current mode at 0.5 C for 200 cycles. The capacities are reported based on mass of silicon, unless mentioned. Electrochemical impedance spectroscopy was performed on fresh electrodes and cycled electrodes for 5, 10, and 50 cycles. EIS was performed using a Gamry Potentiostat/Galvanostat Instrument (Gamry Interface 1000, Gamry Instruments) with 10 mV AC amplitude, with 100 kHz to 5 mHz frequency range, and at 0.2 V *vs.* $Li/Li^+$.

**Results and discussion**

Silicon nanoparticles of size 50-70 nm were used since it is shown in literature that particle fracture is minimized for silicon particles of size <150 nm.[36] Silicon electrodes using TA as a binder were prepared by casting a slurry of silicon nanoparticles, TA, and carbon black, as shown schematically in Figure III-1b. After drying, a homogeneous film formed, and no cracking or agglomeration was observed.

Figure III-2a shows the cyclic voltammogram of Si/TA/CB=70/10/20 (represented by mass ratio) electrode at 0.1 mV/s. In the first cycle, a small cathodic peak is observed at 0.1 V which is attributed to initial alloying of crystalline silicon with $Li^+$ ions.[37] This peak was not present in subsequent cycles. The cathodic peak observed at 0.17 V is attributed to the formation of amorphous - lithiated silicon (a-$Li_XSi$) phase, and the two anodic peaks at 0.4 V and 0.54 V are ascribed to delithiation, which results in the transformation of a-LixSi to a-Si.[38, 39] These results are consistent with other silicon anodes reported.[24, 40-42] We also performed cyclic voltammetry at varying scan rates, as

demonstrated in Figure III-2b. With increasing scan rate, cathodic and anodic peaks shifted to lower and higher potentials, respectively. At scan rates greater than 1 mV/s, cathodic and anodic peaks are not observed. This behavior can be attributed to the limited diffusion of $Li^+$ ions[43, 44] and to ohmic losses in the two-electrode assembly caused by the electrolyte solution.[45] TA itself is redox active, but not within the potentials explored herein.[32] However for this study, silicon anodes were studied in the potential window of 0.01 V to 1 V *vs.* $Li/Li^+$, and thus TA did not contribute to the storage of $Li^+$ ions.

We believe some of the TA will be in reduced form as the reduction potential of TA is ~1.5 V *vs.* $Li/Li^+$.[32] As per the study by Xu et al., the disappearance of C=O and C-O-C peaks in FTIR, followed by an increase in the intensity of in-plane bend of C-O-H group suggests reaction of $Li^+$ ions with the ester carbonyl groups.[32] Since the phenolic -OH groups of TA remains intact in reduced form, those -OH groups still remain available for hydrogen bonding interactions with silicon.

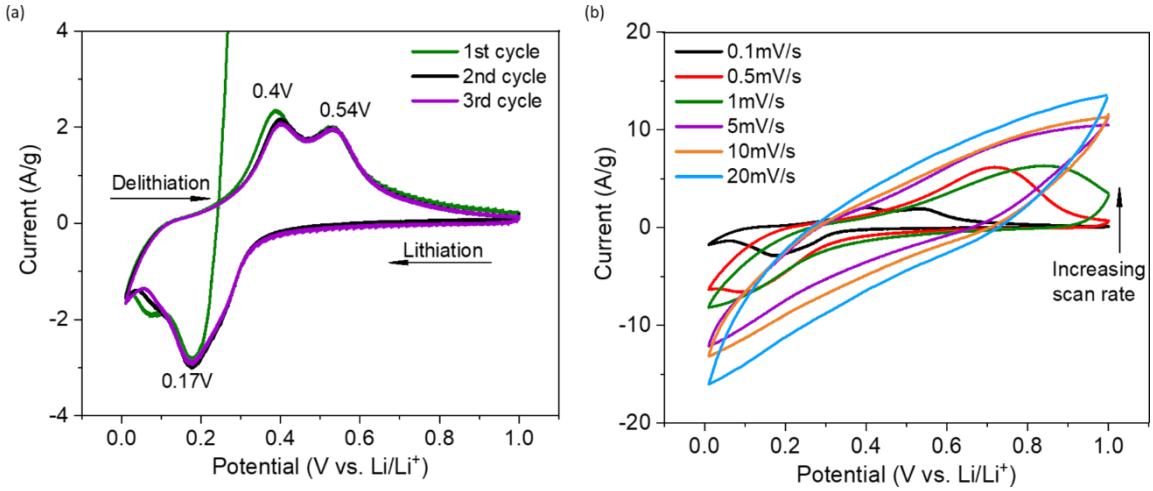


Figure III-2. (a) Cyclic voltammogram of Si/TA/CB=70/10/20 electrode at 0.1 mV/s for three cycles. The peak at 0.17 V represents the formation of lithiated silicon, and the peaks at 0.4 V and 0.5 V represent the delithiation of silicon. (b) Cyclic voltammograms at different scan rates.

Figure III-3a-c demonstrates the galvanostatic cycling performance of silicon electrodes with TA as a binder. Galvanostatic cycling was performed at 0.1 C first for five cycles in CC-CV mode, followed by cycling at 0.5 C for the remaining cycles. Figure III-3a shows discharge capacities and Coulombic efficiencies for different electrode

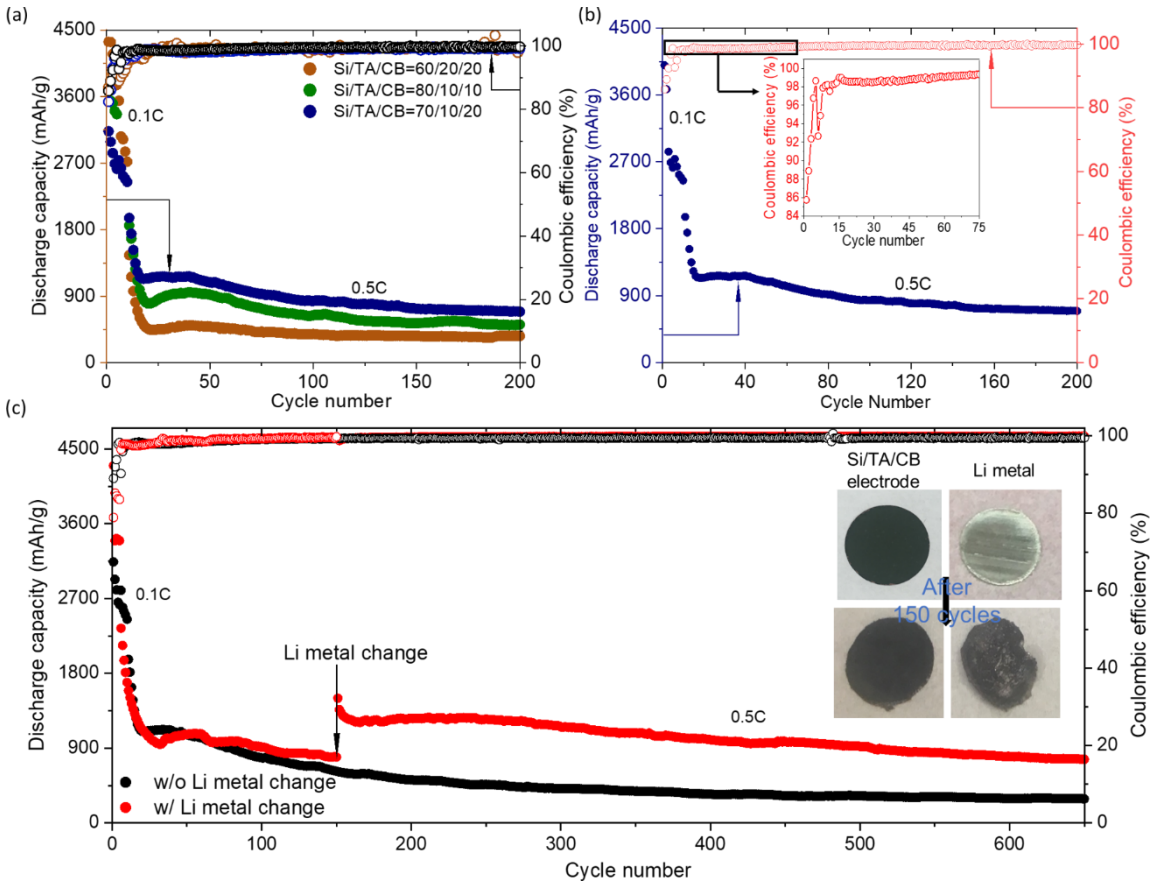


Figure III-3. Galvanostatic charge-discharge of (a) different compositions of Si/TA/CB electrodes, (b) Si/TA/CB=70/10/20 electrode for 200 cycles. Inset in Figure III-3b shows a plot of Coulombic efficiency *vs.* cycle number for first 75 cycles. (c) Galvanostatic charge-discharge of Si/TA/CB=70/10/20 electrode for 650 cycles (in black) without changing lithium metal. Galvanostatic cycling was performed on another electrode (in red) that had its lithium metal changed after the 150$^{th}$ cycle to eliminate any limitation from the lithium itself. Galvanostatic charge-discharge was performed at 0.1 C for the first five cycles in constant current-constant voltage (CC-CV) mode followed by 0.5 C for the remaining 195 cycles.

compositions: Si/TA/CB=60/20/20, Si/TA/CB=70/10/20, and Si/TA/CB=80/10/10 by mass. The silicon loading was controlled to around 0.7-0.8 mg/cm$^2$. The electrode thicknesses after drying for Si/TA/CB=60/20/20, Si/TA/CB=70/10/20, and Si/TA/CB=80/10/10 were 10-12 μm, 7-8 μm, and 6-7 μm, respectively. The electrode with 70 wt% silicon, 10 wt% TA, and 20 wt% CB showed the best capacity out of the three compositions tested.

To further understand the improved performance for the Si/TA/CB=70/10/20 electrode, Figure III-4a-b, we performed electrochemical impedance spectroscopy (EIS) for electrodes of varying compositions. The overall resistance *(i.e.* sum of the semicircle diameters) of the Si/TA/CB=70/10/20 was lowest as compared to the two other electrode compositions tested. Si/TA/CB=80/10/10 showed the highest resistance probably due to its lower CB content. Si/TA/CB=60/20/20 showed a slightly higher resistance than Si/TA/CB=70/10/20 probably due to the higher binder content and higher electrode thickness.[46] This indicates that Si/TA/CB=70/10/20 had a better balance of electron conducting additives and accessibility to the active material, leading to the higher capacity as compared to the other compositions tested.

The results in Figure III-3a and Figure III-4a-b show that the ratio of silicon, TA binder, and carbon black additive is an important factor. Excess TA binder increases the overall impedance[47] and may also participate in side-reactions with the electrolyte.[19] On the other hand, an insufficient amount of TA binder may result in poor adhesion of the electrode components. Peel testing of these electrodes, as shown in Figure III-4c,

demonstrate that the silicon electrode containing 20 wt % TA showed better adhesion, as compared to that with 10 wt % TA. Overall, we believe that a proper balance between active material, binder, and carbon additives is essential to maintain a proper electronic network without any agglomeration. With these factors in consideration, all further studies were performed using the Si/TA/CB=70/10/20 composition because it provided the best balance of these factors.

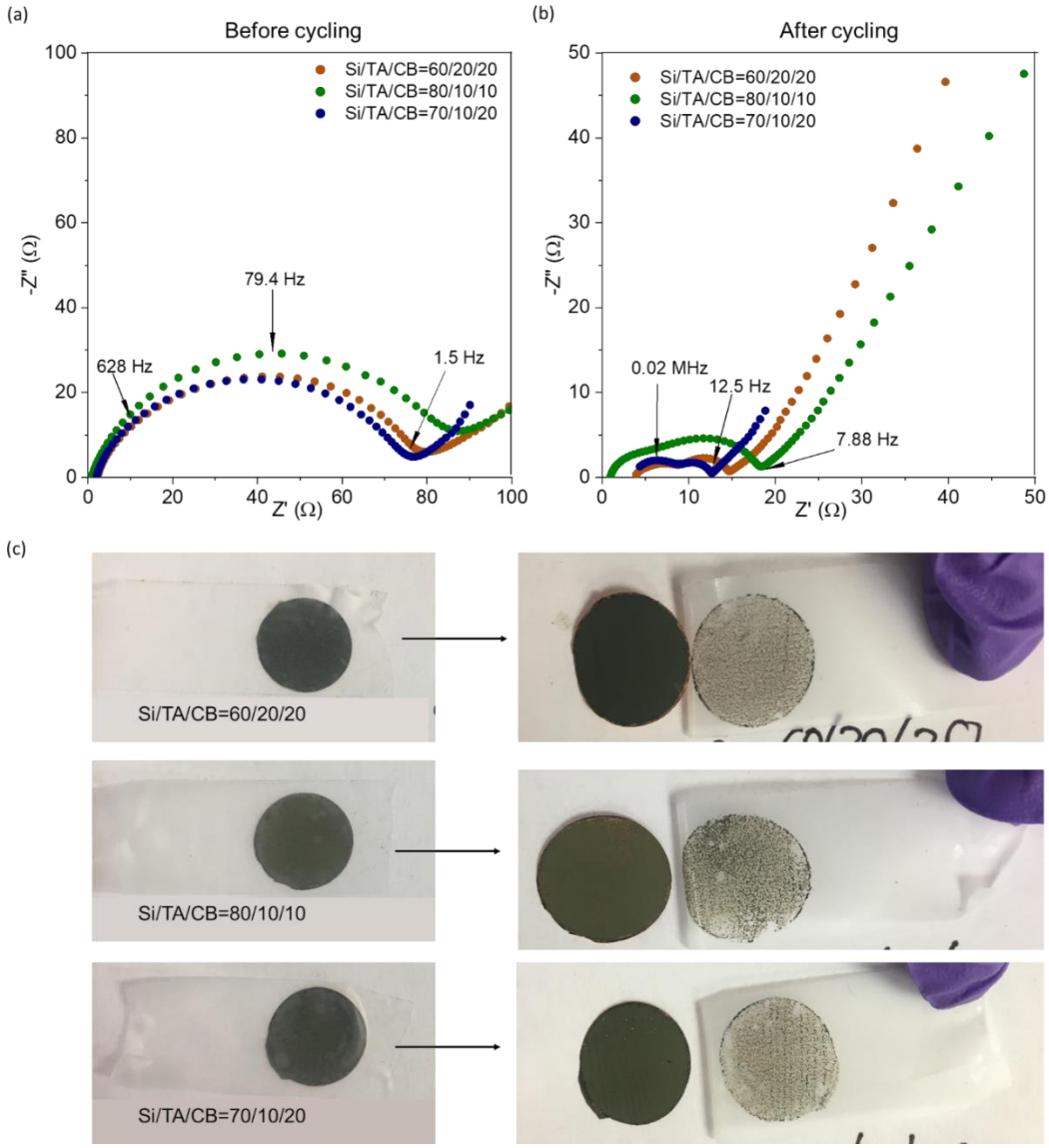


Figure III-4. Nyquist plot of Si/TA/CB electrodes with different compositions (a) before and (b) after 50 cycles. Electrochemical impedance spectroscopy (EIS) was performed on fresh and cycled electrodes at a potential of 0.2 V. The AC amplitude was 10 mV. The frequency range was 100 kHz to 5 mHz. (c) Peel test of Si/TA/CB=60/20/20, Si/TA/CB=80/20/20, and Si/TA/CB=70/10/20 electrodes. A 3M tape was used here, and it was pressed on the samples for 5 seconds with equal force before peeling it off.

We next examined the Si/TA/CB=70/10/20 electrode in further detail. The initial discharge capacity of Si/TA/CB=70/10/20 electrode was 4050 mAh/g (Figure III-3b and

Figure III-5a) and the charge capacity was 2800 mAh/g at 0.1 C. Such a large irreversible capacity loss is common for silicon electrodes, arising from electrolyte decomposition, SEI formation, or electrical disconnection caused by volume changes.[48] The voltage profile demonstrated in Figure III-5a was consistent with previous silicon studies, which exhibit a long flat plateau during the first lithiation process in which silicon reacts with $Li^+$ ions to form amorphous $Li_xSi$.[49]

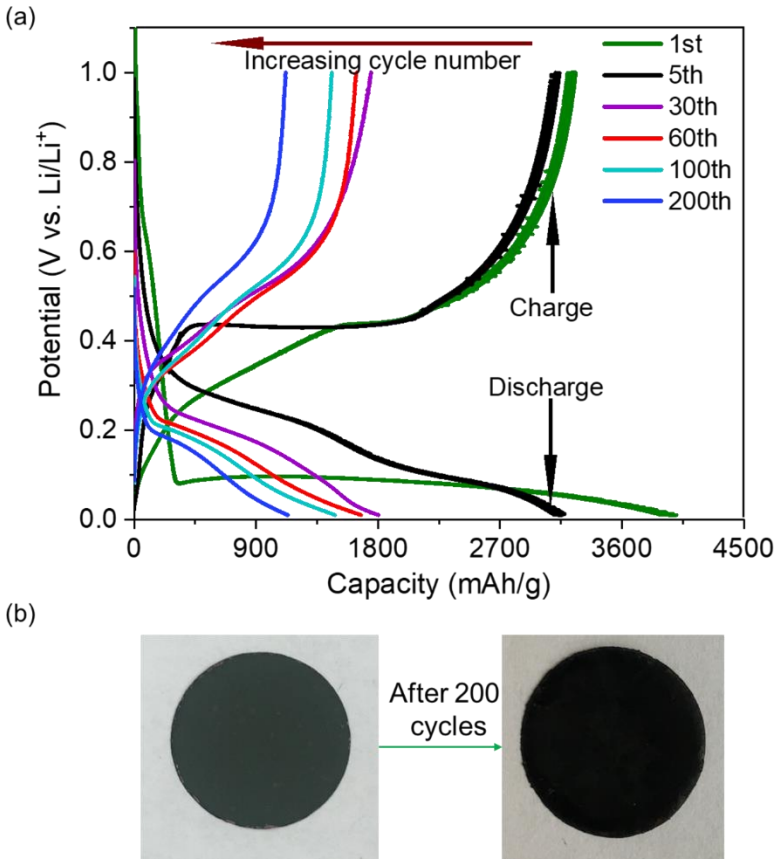


Figure III-5. (a) Voltage profile of Si/TA/CB=70/10/20 electrode for different cycle numbers. (b) Picture of Si/TA/CB=70/10/20 electrode before and after cycling for 200 cycles. The picture for the cycled electrode was taken after it was washed with dichloromethane and dried inside the glovebox.

After five cycles at 0.1 C, the anodes were then cycled at 0.5 C. The capacity decreased to 1000 mAh/g and then stabilized at 700 mAh/g up to 200 cycles, which

implies that the electrode was structurally stable.[50, 51] Also, no visual delamination or crack formation occurred after 200 cycles (Figure III-5b). Thus, the drop in capacity for the first few cycles can be attributed to SEI formation (demonstrated later in the text) and to the lack of elastic nature of TA as compared to that of a high molecular weight polymeric binder. Analysis of the Coulombic efficiency can also lend insight into the evolution of the electrode during cycling. The Coulombic efficiency of the first cycle was 86 %. Within the first 15 cycles, the Coulombic efficiency increased to 98 % then stabilized to >99.5 % within 50 cycles, implying the formation of a stable SEI.

To further demonstrate electrode stability over many cycles, a Si/TA/CB=70/10/20 electrode was cycled for 650 cycles at 0.5 C (Figure III-3c). We note that the discharge capacity dropped rapidly around the 120th cycle (shown in black). After disassembling the cell, we observed that the silicon electrode was devoid of cracks or delamination; however, the lithium metal had become black in color (inset in Figure III-3c). This behavior can be explained by degradation of the lithium metal at a high C-rate (>0.2 C), as reported previously by Choi *et al.*[42] In a separate sample, the lithium metal was exchanged for a new one after the 150th cycle (shown in red), and galvanostatic cycling was continued at 0.5 C. After changing the lithium metal, the silicon electrode recovered some of its capacity, and operated at a capacity above 850 mAh/g for the remaining 500 cycles at 0.5 C.

We compare the performance of our electrode with that reported by Tian *et al.* in which they made electrodes using silicon microparticles, TA, poly(acrylic acid) (PAA), and Super P CB.[46] Their electrodes (Si loading = 0.48 mg/cm$^2$) demonstrated a capacity

of ~2000 mAh/g at a current density of 0.6 A/g (~0.1 C) for at the 100$^{th}$ cycle. As compared to their work, our electrodes demonstrated a lower capacity (850 mAh/g at 0.5 C) with higher silicon loading (~0.7 mg/cm$^2$) and for a large number of cycles (600 cycles) with 10 wt % TA. Tian *et al.* added PAA to their electrode system (total binder content ~22 wt%),[46] where as we did not include a polymer so as to assess the behavior of the TA alone. The relatively good stability of our electrode for 10 wt% TA binder is attributed to the strong interactions between TA's hydroxyl groups and -OH groups at the silicon nanoparticle surface. Also, it performed as well as other reported polymeric binders in literature (Table III-1).[16, 21, 23-25, 27, 28, 30, 40, 42, 52-55]

Table III-1. Comparison of different silicon anode binders

| **Binder** | **Si/binder/ CB (by mass)** | **Si Loading (mg/cm$^2$)** | **Electrolyte (Salt, Solvent, Additive)** | **Cycling Performance** | **Ref** |
|---|---|---|---|---|---|
| Water soluble binders | | | | | |
| Tannic acid | 70/10/20 | 0.75-0.82 | 1 M $LiPF_6$, EC:DEC= 1:1 vol%, 10 wt% FEC | 850 mAh/g at 200$^{th}$ cycle at 0.5 C | This work |
| | | 0.5 | | 1125 mAh/g at 200$^{th}$ cycle at 0.5 C | |
| Poly (acrylic acid sodium) grafted carboxymethyl cellulose NaPAA-g-CMC | 60/20/20 | 0.45 | 1 M $LiPF_6$, EC:DMC=1:1 vol%, 10 wt% FEC | 1816 mAh/g at 100$^{th}$ cycle at 0.1 C | [28] |
| Poly(acrylic acid) (PAA) | 43/15/42 | - | 1 M $LiPF_6$ in EC:DEC:DMC= 1:1:1 vol%, 5 wt% VC | 2000 mAh/g at 100$^{th}$ cycle at 0.5 C | [21] |

Table III-1. Continued

| **Binder** | **Si/binder/ CB (by mass)** | **Si Loading ($mg/cm^2$)** | **Electrolyte (Salt, Solvent, Additive)** | **Cycling Performance** | **Ref** |
|---|---|---|---|---|---|
| Poly(acrylic acid)-poly(vinyl alcohol) PAA-PVA | 60/20 (PAA:PVA=9:1)/20 | - | 1 M $LiPF_6$ in EC:DEC:DMC= 1:1:1 vol%, 10 wt% FEC | 2283 mAh/g at $100^{th}$ cycle at 1 C | [27] |
| Poly(dopamine) | 80/10/10 | 0.5 | 1 M $LiPF_6$, EC:DMC=1:1 vol%, 10 wt% FEC | 1800 mAh/g at $100^{th}$ cycle at 0.5 C | [52] |
| Sodium alginate (Alg) | Si:C(3:1)/ Alg =85/15 | - | 1 M $LiPF_6$, DMC:EC:DEC= 1:1:1 vol% | 2000 mAh/g at $100^{th}$ cycle at 1 C | [24] |
| Polymerized β-cyclodextrin | 60/20/20 | 0.6 | 1.15 M $LiPF_6$, EC:EMC:DEC= 3:5:2 vol% | 1500 mAh/g at $100^{th}$ cycle at 1 C | [25] |
| Polyrotaxane-poly(acrylic acid) | 80/10/10 (silicon microparticles were used) | 1 | 1 M $LiPF_6$, EC:DEC=1:1 vol%, 0.5 wt% VC and 7.5 wt% FEC | 2.43 $mAh/cm^2$ at $150^{th}$ cycle at 0.2 C | [42] |
| Sodium carboxymethyl cellulose | 80/8/12 | 1.8 | 1 M $LiPF_6$ in EC:DEC=1:2 vol% | 1100 mAh/g at $70^{th}$ cycle at 0.03 C | [23] |
| Chitosan-glutaraldehyde | 60/20/20 | - | 1 M $LiPF_6$ in a mixture of solvents | 2130 mAh/g at $100^{th}$ cycle at 0.1 C | [30] |
| Galactomannans | 85/5/10 | 0.75 | 1 M $LiPF_6$ in EC:EMC=1:1 vol% | 1000 mAh/g at $100^{th}$ cycle at 1 C | [16] |

Table III-1. Continued

| **Binder** | **Si/binder/ CB (by mass)** | **Si Loading ($mg/cm^2$)** | **Electrolyte (Salt, Solvent, Additive)** | **Cycling Performance** | **Ref** |
|---|---|---|---|---|---|
| Poly(acrylamide) | 70/15/15 | 1-1.1 | 1 M $LiPF_6$ in EC:DEC:DMC= 1:1:1 vol% | 2000 mAh/g at $300^{th}$ cycle at 0.1 C | [40] |
| Polyvinyl alcohol-polyethyleneimine PVA-PEI | 60/20 (PVA:PEI =8:2)/20 | 1.8-2.7 | 1 M $LiPF_6$ in EC:DMC=1:1 vol% | 1060 mAh/g at $300^{th}$ cycle at ~0.2 C | [54] |
| Organic solvent-based binder | | | | | |
| PVDF | Si:C(3:1)/ PVDF=85 /15 | 0.5-0.7 | 1 M $LiPF_6$, EC:DEC:FEC=1 :1:0.04 vol% | 420 mAh/g at $40^{th}$ cycle at 0.1 C | [55] |
| Self-healing polymer (Diamido tetraethyltriurea) | 80/10/10 | 1.13 | 1 M $LiPF_6$ in EC:DEC:VC:FEC=1:1:0.05:0.05 vol% | 1820 mAh/g at $140^{th}$ cycle at 0.05 C | [53] |

To demonstrate the hydrogen bonding interaction between TA and the silicon particles, we performed XPS on a mixture of the two before and after washing with water.[25, 53] It was observed that the C 1s peak resulting from TA was still present in the XPS spectra even after vigorously washing the mixture with water, in which TA is normally highly soluble (Figure III-6). This indirectly implies that silicon nanoparticle-TA interactions are strong and numerous enough to prevent dissolution of the TA.

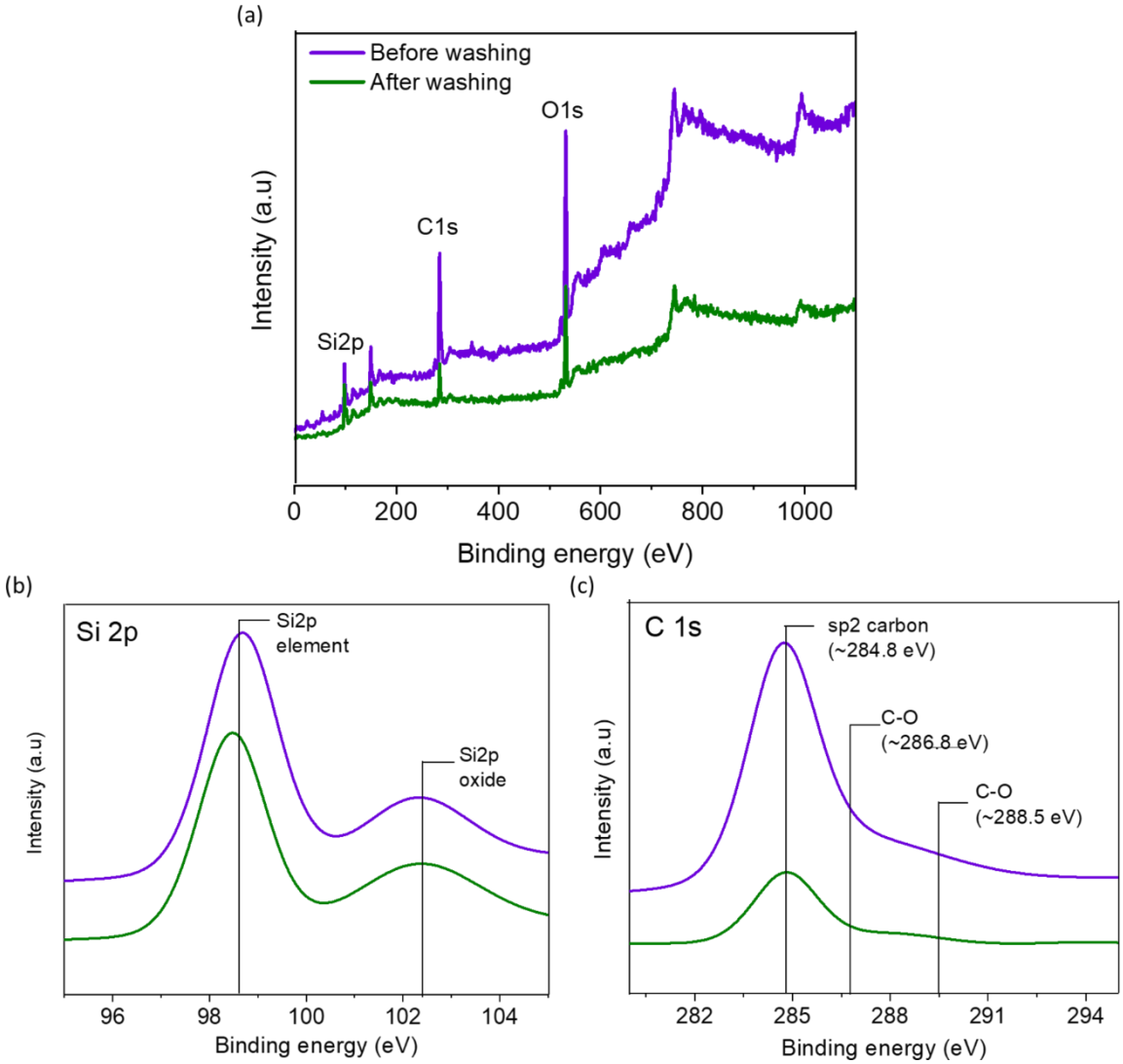


Figure III-6. X-ray photoelectron spectroscopy (XPS) characterization (a) survey scan, (b) Si 2p spectra, and (c) C 1s spectra of silicon nanoparticle and TA mixture before and after washing with water.

We next studied the electrode response at high C-rates, the electrode was subjected to increasing C-rates from 0.1 C to 5 C (Figure III-7a). The first-cycle discharge capacities

at 0.1 C and 1 C were 3800 mAh/g and 1500 mAh/g, respectively. The rapid drop in capacity with higher C-rates has been widely reported for silicon anodes.[56-58] After cycling at 5 C, the C-rate was decreased to 0.1 C, and approximately 87.5 % of the initial capacity was recovered. The similar voltage profiles (Figure III-7b) and decent capacity recovery implies that the electrode did not undergo major degradation (*i.e.* disintegration of electrode structure causing breakage of electronic pathways) higher C-rates and that capacity fade mostly arose from $Li^+$ ion diffusion limitations.[1, 10]

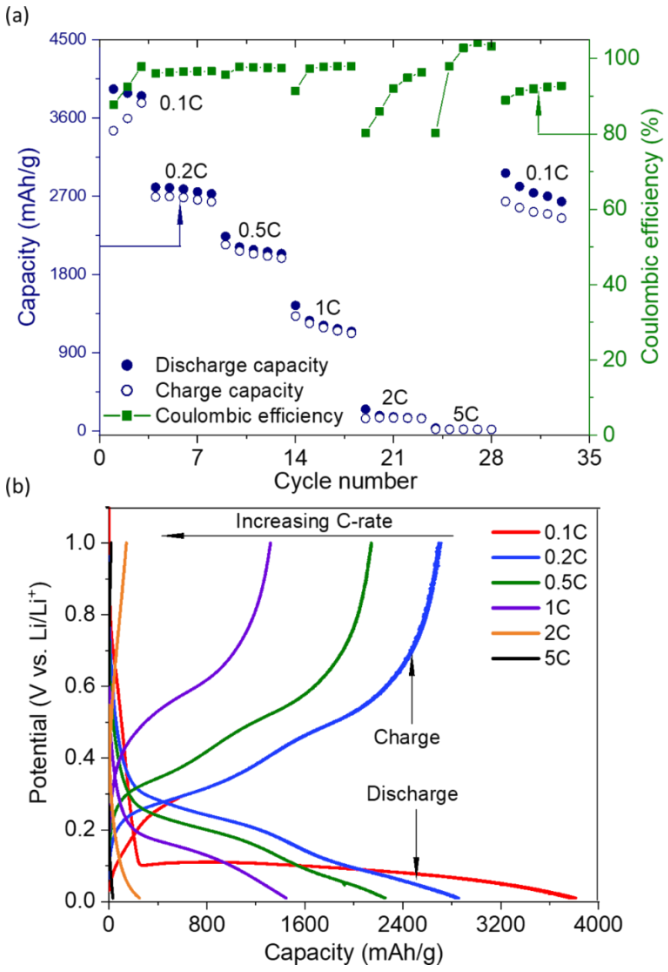


Figure III-7. (a) Galvanostatic charge-discharge of Si/TA/CB=70/10/20 electrode at different C-rates. (b) Voltage profile of the same electrode at different C-rates.

The electrode morphology (surface and cross-section) before and after cycling was studied using SEM (Figure III-8a-b). Fresh electrodes showed a uniform surface morphology, and the cross-section showed a densely packed structure with no visible cracks. Uniform distribution of silicon nanoparticles and TA in the electrode was observed via energy dispersive X-ray spectroscopy (EDS) mapping of Si, C, and O elements, as shown in Figure III-8c. After 50 cycles, an SEI layer was observed at the, along with minor surface cracks due to internal stresses during lithiation and delithiation. The cross-section images show that electrode thickness increased from 8 µm to 11 µm (a 38 % increase). The cracks only appeared at the surface and did not extend through the thickness of the electrode. This increase in electrode thickness after cycling is usually observed for silicon electrodes.[59, 60] But, as indicated in Figure III-3, the electrode maintained a stable capacity over a large number of cycles, which implies that TA was able to anchor to the silicon nanoparticles successfully.

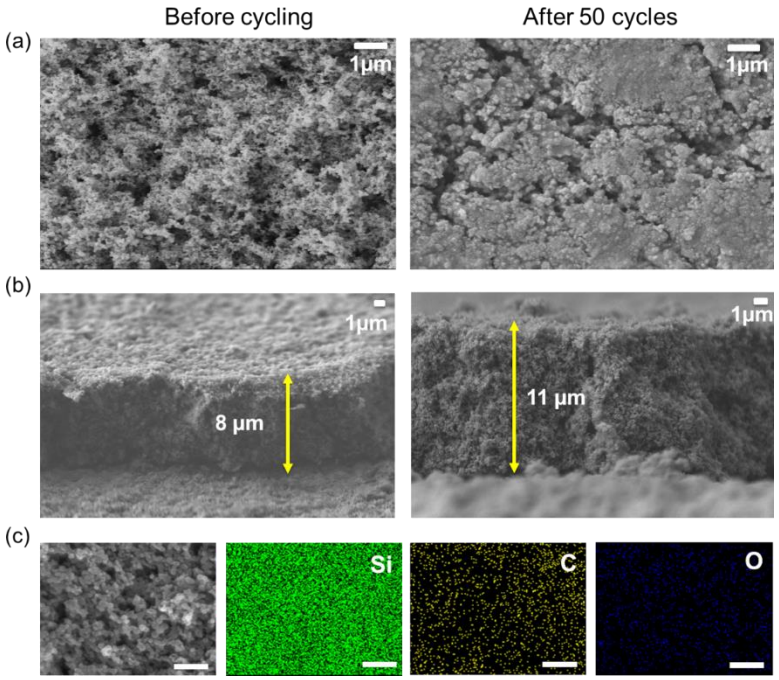


Figure III-8. Scanning electron microscopy (SEM) images of (a) the surface and (b) cross-section of a Si/TA/CB=70/10/20 electrode before and after 50 cycles of charge-discharge. (c) Energy dispersive spectroscopy (EDS) mapping of Si/TA/CB=70/10/20 electrode before 50 cycles of charge-discharge. The scale bar on the EDS images are 1 μm.

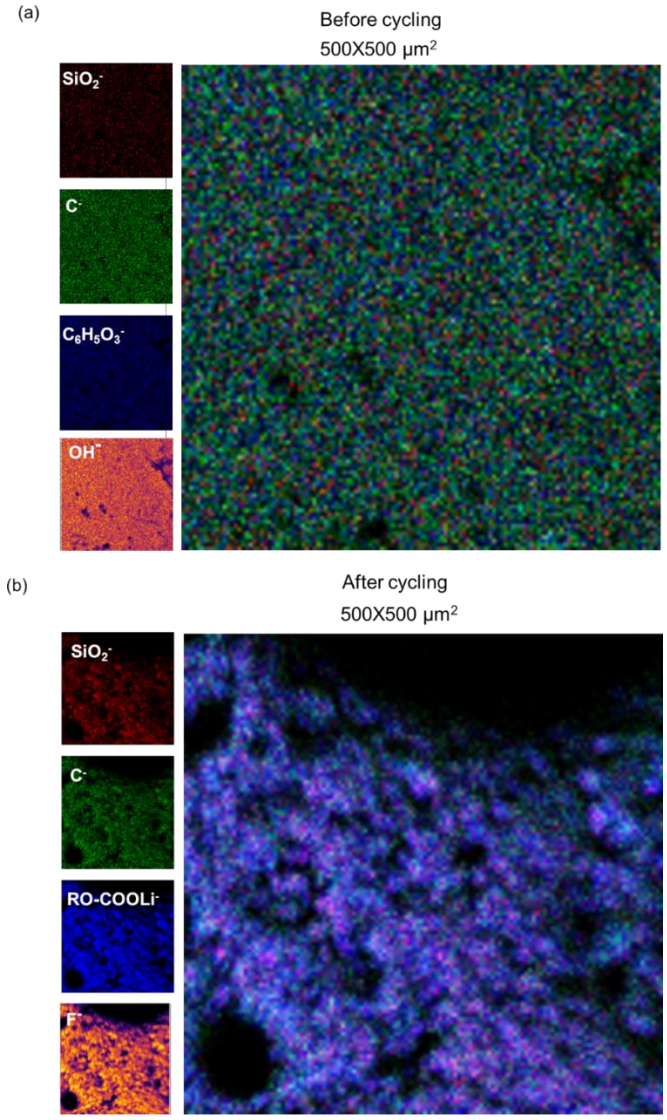


Figure III-9. Overlap of time of flight-secondary ion mass spectroscopy (ToF-SIMS) surface profile images of selected electrode components of Si/TA/CB=70/10/20 electrode (a) before and (b) after 50 cycles of charge-discharge. Here, we used $SiO_2^-$ to represent the silicon nanoparticles, $C_6H_5O_3^-$ to represent TA, $C^-$ to represent carbon from Super P carbon black (CB), and RO-COOLi to represent one component of the SEI.

We also performed ToF-SIMS (Figure III-9) on electrodes before and after 50 cycles of charge-discharge to examine ion fragments corresponding to silicon nanoparticles, TA, Super P CB, and the SEI layer. Specifically, $SiO_2^-$ reflects the silicon

nanoparticles, $C_6H_5O_3^-$ the TA, $C^-$ the Super P CB, and RO-COOLi the SEI layer. As seen in Figure III-9a, a smooth morphology and uniform distribution of silicon, TA and CB is present before cycling. The existence of $SiO_2$- on the fresh electrode surface reveals some amount of oxidation of the silicon particle surface, leading to the presence of -OH groups.[61] This finding supports our hypothesis that TA hydrogen bonds with -OH groups at the silicon particle's surface. The electrodes after cycling showed a more heterogeneous surface chemistry (Figure III-9b). The drop in intensity of $SiO_2$- and an increase in intensity of RO-COOLi indicated the formation of an SEI layer. The $C_6H_5O_3^-$ component representative of TA was not detected, indicating that the SEI covered electrode surface. The overlapped image shows that the majority of the SEI components are present on the surface of the cycled electrode (*i.e.* intensities of $C^-$ and $SiO_2^-$ were much lower than that of RO-COOLi).

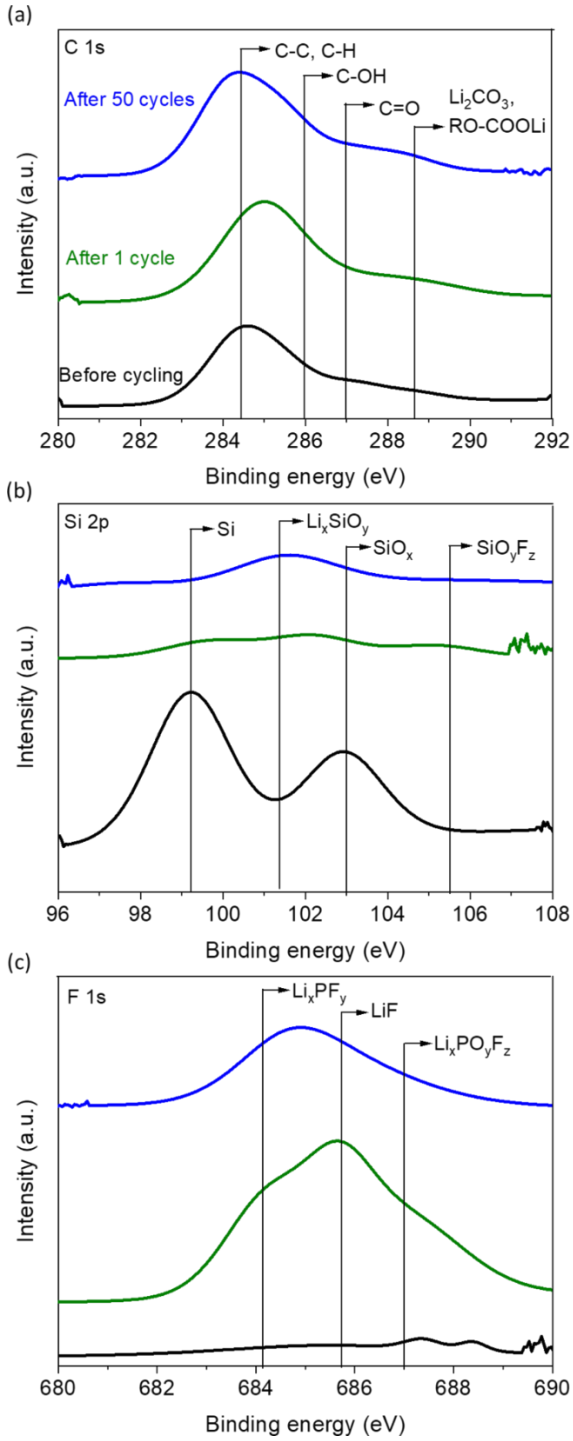


Figure III-10. X-ray photoelectron spectroscopy (XPS) spectra of (a) C 1s, (b) Si 2p, and (c) F 1s of Si/TA/CB=70/10/20 electrode before cycling, after 1 cycle, and after 50 cycles of charge-discharge.

To further understand the composition and stability of the SEI formed, XPS was performed on the silicon electrodes before cycling, after 1 cycle, and after 50 cycles as shown in Figure III-10. The C 1s spectra show the emergence of a peak at approximately 288.5 eV after cycling, which is associated with the formation of carbonaceous species including $Li_2CO_3$ or RO-COOLi. Both have been widely reported as the main components of the SEI formed on silicon.[24, 62, 63] The Si 2p spectra before cycling demonstrates the presence of Si (99.2 eV) and $SiO_2$ (103 eV). After the 1st cycle, an additional peak at 105.3 eV appeared after cycling which is attributed to the formation of $SiO_yF_z$ from consumption of $SiO_x$.[63] This peak disappeared after 5 cycles, and another peak at 101.2 eV was observed, which is attributed to the formation of $Li_xSiO_y$.[64] The Si peak almost disappears after 50 cycles due to thicker SEI formation. No fluorine is observed in the F 1s spectra before cycling, as expected. After cycling, LiF and $Li_xPF_y$ peaks at 685.8 eV and 684 eV, respectively, were observed; these are attributed to decomposition of $LiPF_6$ in which FEC is present in the electrolyte.[64, 65] In general, XPS measurements demonstrate that the SEI layer consisted of electrolyte decomposition products, including LiF, $Li_xSiO_y$, $Li_2CO_3$, $Li_xPO_yF_z$, and RO-COOLi. However, the SEI composition changes slightly after 50 cycles, which can be due to additional reactions on cycling and formation of thicker SEI.[66] Overall, the stable cycling performance, structural integrity, and stable SEI formation can be attributed to tannic acid's many -OH groups that hydrogen bond with the silicon nanoparticle's surface.

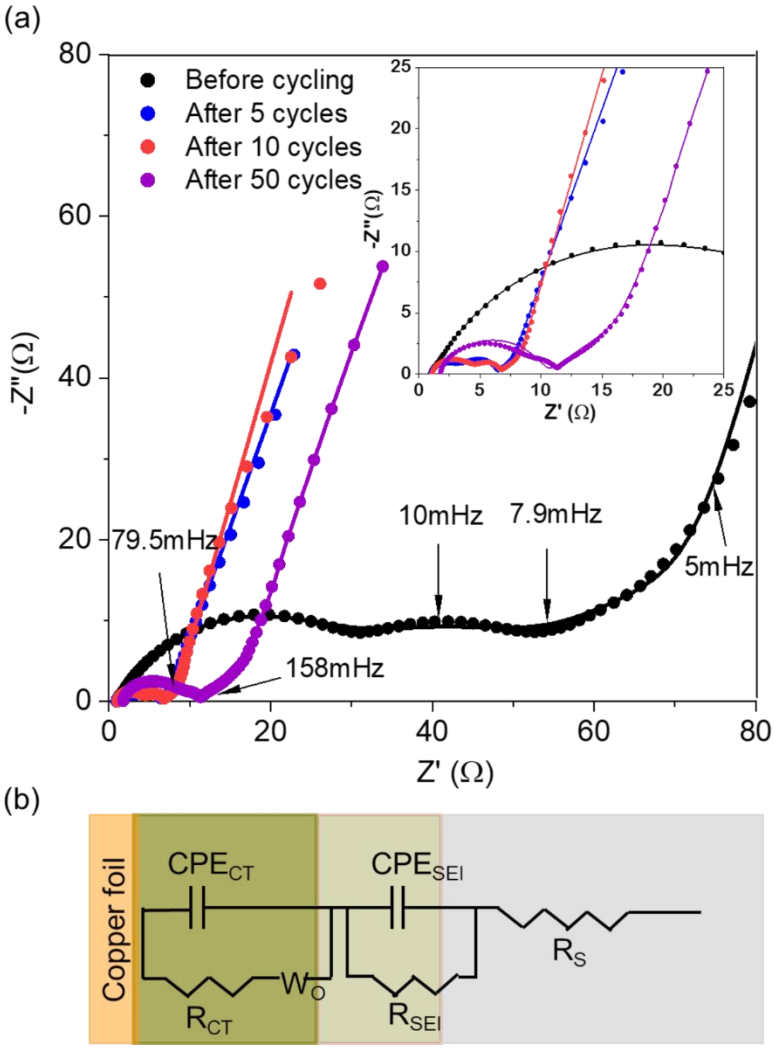


Figure III-11. (a) Nyquist plot of Si/TA/CB=70/10/20 electrode before cycling and after 5, 10, and 50 cycles of charge-discharge. EIS data were collected after different cycles to determine the change in electrode impedance due to cycling. Inset shows an expanded view of the high frequency region. EIS was performed at a potential of 0.2 V (lithiation). The frequency range was from 100 kHz to 5 mHz, and the amplitude was 10 mV. (b) Equivalent circuit used to model the after cycling EIS data. The dotted lines represent the experimental data and solid lines represent the equivalent circuit model fit to the data.

Electrochemical impedance spectroscopy was performed on the Si/TA/CB=70/10/20 electrode before and after cycling to monitor changes in impedance during the lithiation process (at 0.2 V). The Nyquist plot in Figure III-11a shows depressed

semicircles in both the high and medium frequency regions and a Warburg tail in the low frequency region. The depressed semicircle in the high frequency region is indicative of the SEI film resistance, and the one in the medium frequency region is indicative of the charge transfer resistance at the electrode-electrolyte interface. The Warburg tail in the low frequency region is indicative of solid-state $Li^+$ ion diffusion.

To demonstrate the physical significance of the electrochemical process occurring at 0.2 V, an equivalent circuit was fit to the EIS data (Figure III-11b). The circuit consisted of an ohmic resistance ($R_O$), which is the resistance to $Li^+$ ion conduction through the bulk electrolyte to the electrode-electrolyte interface and to the electronic conduction through the electrode to the copper foil-electrode interface; a charge transfer resistance ($R_{CT}$) due to the reaction between the silicon and $Li^+$ ions; a constant phase element (*CPE*) due to the electrode-electrolyte interface; a resistance due to the SEI layer ($R_{SEI}$); a *CPE* due to the SEI layer-electrolyte interface; and a Warburg impedance ($W_O$) related to solid-state $Li^+$ ion diffusion. Table III-2 summarizes the results of fitting the equivalent circuit to the EIS data. The diffusion coefficient (calculated using previous reports)[43, 67] was around 8.1 x $10^{-12}$ $cm^2/s$, which is in accordance with literature values for silicon anodes.[67]

From the equivalent circuit model, we observed that the electrode's resistance ($R_{SEI}$ + $R_{CT}$ = 68.6 ohms) varied with cycling. After 5 cycles, $R_{SEI}$ + $R_{CT}$ was 7.05 Ω, and this value increased slightly to 9.53 Ω after 50 cycles, Table III-2. The slight increase in resistance in subsequent cycles[68] can be attributed to increased thickness due to SEI formation and irreversible increase in electrode's volume during initial $Li^+$ ion insertion/extraction cycles[69] – evident from the SEM images in Figure III-8b.

Table III-2. The results of fitting an equivalent circuit to the EIS data.

| | $R_O$ (Ω) | $R_{SEI}$ (Ω) | $CPE_{SEI}$ (x $10^{-5}$ μF) | $R_{CT}$ (Ω) | $CPE_{CT}$ (x $10^{-4}$ μF) | $\chi^2$ | $\sigma$ (Ω/s) | Solid-state $D_{Li+}$ (x $10^{-12}$ $cm^2/s$) |
|---|---|---|---|---|---|---|---|---|
| **Before cycling** | 1.81 | - | - | 66.1 | 5.55 | 0.001 | - | - |
| **After 5 cycles** | 1.05 | 1.71 | 0.50 | 3.55 | 5.88 | 0.005 | 3.21 | 6.44 |
| **After 10 cycles** | 1.12 | 2.68 | 0.47 | 2.76 | 8.98 | 0.004 | 4.35 | 8.99 |
| **After 50 cycles** | 1.71 | 7.53 | 1.06 | 1.47 | 0.74 | 0.005 | 4.03 | 8.80 |

Our work demonstrates how the small molecule tannic acid behaves as a binder for silicon anodes. Despite having a much lower molecular weight compared with popular polymeric binder materials, tannic acid is effective due to the large number of hydrogen bonding groups (14.8 millimoles of OH/g of TA ), which is even greater than PAA(13.8 millimoles of -COOH/g of repeat unit of PAA) and polydopamine (13.3 millimoles of -OH/g of repeat unit of polydopamine ), see Table III-3. As shown Table III-1, the cycling performance of our silicon electrode with TA binder was comparable to other water-based binders reported in literature. This comparison shows that the TA electrodes reported here compare favorably. One other recent study reported excellent performance in silicon anodes with citric acid as a binder.[70] Our work along with this recent study indicate that

branched, functional small molecules may be superior (or comparable) to many polymers as binders for silicon anodes.

Table III-3. Comparison of different binders and the millimoles of hydroxyl (-OH) and carboxyl (-COOH) functional groups per gram of the binder. For polymers, the molecular weight is that of the repeat unit.

| Type | Binder | Molecular weight (g/mol) | No. of OH/unit | Millimoles of OH/g | No. of COOH /unit | Millimoles of COOH/g |
|---|---|---|---|---|---|---|
| Low molecular weight branched molecule | Tannic acid | 1686 | 25 | 14.8 | - | - |
| Long chain linear polymers | Poly(acrylic acid) | 72[a] | - | - | 1 | 13.8 |
| | Sodium salt of alginic acid | 219[a] | 4 | 18.3 | 2 | 9.13 |
| | Poly(vinylidene fluoride) | 64[a] | - | - | - | - |
| | Polydopamine | 150[a] | 2 | 13.3 | - | - |

Because it is difficult to compare performance of binders across different reports due to differences in electrode composition, loading, battery assembly, and cycling conditions; we performed an in-house comparison with a few common binders. Figure III-12 shows the cycling performance of silicon electrodes with poly(vinylidene fluoride) (PVDF), poly(acrylic acid) (PAA), and sodium alginate (Alg). We purposefully used similar active material loading, battery assembly, and cycling conditions. The 70/10/20 Si/TA/CB anode possessed the best performance in this in-house comparison. Si/PVDF/CB demonstrated the lowest capacity due to the absence of hydrogen bonding groups. Si/PAA/CB showed lower capacity than Si/TA/CB, possibly due to lower density of -COOH groups. Si/Alg/CB also showed lower capacity than Si/TA/CB despite having

higher density of -OH groups (18.3 milimoles of -OH/g of repeat unit of Alg), which can be attributed to the lack of a branched structure. Therefore, this in-house comparison demonstrates the importance of hydrogen bonding groups and branched structures for effective silicon anode binders.

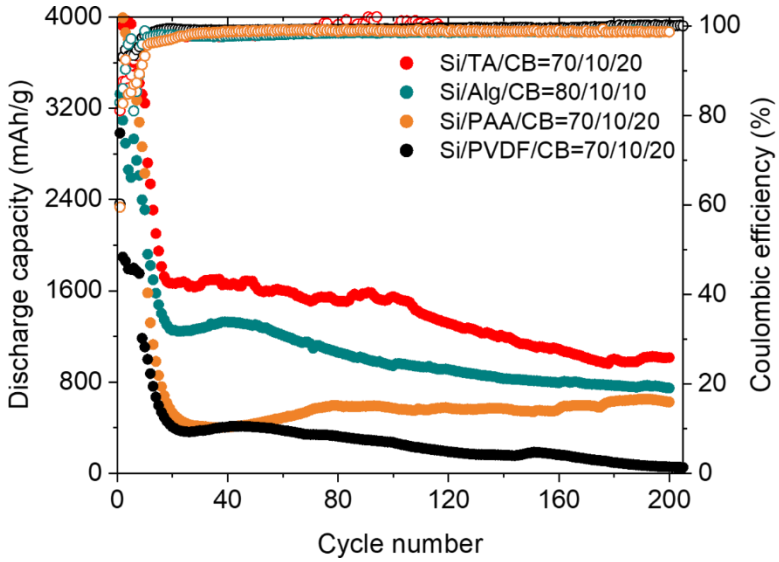


Figure III-12. In-house comparison of cycling performance of Si/TA/CB electrode to Si/Alg/CB, Si/PAA/CB, and Si/PVDF/CB electrode. Here, similar active material loading, same battery assembly, and cycling conditions were used to make a direct comparison.

**Conclusions**

This report isolated the effects hydrogen bonding of the small molecule binder tannic acid for silicon anodes. With few exceptions, silicon anodes primarily incorporate high molecular weight polymeric binders. However, tannic acid, which is a small, branched, water-soluble polyphenol with a large number of -OH functional groups, performs comparably to many polymeric binders and excelled in an in-house comparison to PVDF and PAA. An optimal electrode composition of 70 wt% silicon, 10 wt% TA, 20 wt% CB was identified, which balanced both electronic conductivity and active material

accessibility. This electrode demonstrated a discharge capacity of 850 mAh/g at the 600$^{th}$ cycle at 0.5 C. Cycling did bring about some volume expansion and surface cracking, but no delamination or wide-spread cracking was apparent. Elemental mapping demonstrated evidence of the hydrogen bonding mechanisms between $SiO_2$ at the silicon nanoparticle surface and TA. A well-formed SEI layer was observed, which likely contributed to the stable cycling performance. The in-house comparison with other polymeric binders demonstrated the importance of not only hydrogen bonding but also branching in the molecular structure. Looking to the future, other small molecules may prove to be effective binders, so long as they are branched and have numerous non-covalent interactions with the silicon nanoparticle surface.

**References**


1. Chae, S.; Ko, M.; Kim, K.; Ahn, K.; Cho, J., Confronting Issues of the Practical Implementation of Si Anode in High-Energy Lithium-Ion Batteries. *Joule* **2017,** *1* (1), 47-60.
2. Cheng, F.; Liang, J.; Tao, Z.; Chen, J., Functional Materials for Rechargeable Batteries. *Adv. Mater.* **2011,** *23* (15), 1695-715.
3. Li, J.-Y.; Xu, Q.; Li, G.; Yin, Y.-X.; Wan, L.-J.; Guo, Y.-G., Research Progress Regarding Si-Based Anode Materials Towards Practical Application in High Energy Density Li-Ion Batteries. *Mater. Chem. Front.* **2017,** *1* (9), 1691-1708.
4. Fu, Q.; Cao, H.; Liang, G.; Luo, L.; Chen, Y.; Murugadoss, V.; Wu, S.; Ding, T.; Lin, C.; Guo, Z., A Highly Li(+)-Conductive $HfNb_{24}O_{62}$ Anode Material for Superior Li(+) Storage. *Chem. Commun. (Camb)* **2020,** *56* (4), 619-622.
5. Idrees, M.; Batool, S.; Zhuang, Q.; Kong, J.; Seok, I.; Zhang, J.; Liu, H.; Murugadoss, V.; Gao, Q.; Guo, Z., Achieving Carbon-Rich Silicon-Containing Ceramic Anode for Advanced Lithium Ion Battery. *Ceram. Int.* **2019,** *45* (8), 10572-10580.
6. Batool, S.; Idrees, M.; Kong, J.; Zhang, J.; Kong, S.; Dong, M.; Hou, H.; Fan, J.; Wei, H.; Guo, Z., Assessment of the Electrochemical Behaviour of Silicon@Carbon Nanocomposite Anode for Lithium-Ion Batteries. *J. Alloys Compd.* **2020,** *832*, 154644-154653.
7. Feng, K.; Li, M.; Liu, W.; Kashkooli, A. G.; Xiao, X.; Cai, M.; Chen, Z., Silicon-Based Anodes for Lithium-Ion Batteries: From Fundamentals to Practical Applications. *Small* **2018,** *14* (8), 1702737-70.

8. Erk, C.; Brezesinski, T.; Sommer, H.; Schneider, R.; Janek, J., Toward Silicon Anodes for Next-Generation Lithium Ion Batteries: A Comparative Performance Study of Various Polymer Binders and Silicon Nanopowders. *ACS Appl. Mater. Interfaces* **2013,** *5* (15), 7299-307.
9. Lee, J. K.; Oh, C.; Kim, N.; Hwang, J.-Y.; Sun, Y.-K., Rational Design of Silicon-Based Composites for High-Energy Storage Devices. *J. Mater. Chem. A* **2016,** *4* (15), 5366-5384.
10. Luo, W.; Chen, X.; Xia, Y.; Chen, M.; Wang, L.; Wang, Q.; Li, W.; Yang, J., Surface and Interface Engineering of Silicon-Based Anode Materials for Lithium-Ion Batteries. *Adv. Energy Mater.* **2017,** *7* (24), 1701083-111.
11. See, K. A.; Lumley, M. A.; Stucky, G. D.; Grey, C. P.; Seshadri, R., Reversible Capacity of Conductive Carbon Additives at Low Potentials: Caveats for Testing Alternative Anode Materials for Li-Ion Batteries. *J. Electrochem. Soc.* **2016,** *164* (2), A327-A333.
12. Badi, N.; Erra, A. R.; Hernandez, F. C. R.; Okonkwo, A. O.; Hobosyan, M.; Martirosyan, K. S., Low-Cost Carbon-Silicon Nanocomposite Anodes for LIBs. *Nanoscale Res. Lett.* **2014,** *9* (1), 1-8.
13. Casimir, A.; Zhang, H.; Ogoke, O.; Amine, J. C.; Lu, J.; Wu, G., Silicon-Based Anodes for Lithium-Ion Batteries: Effectiveness of Materials Synthesis and Electrode Preparation. *Nano Energy* **2016,** *27*, 359-376.
14. Wu, H.; Cui, Y., Designing Nanostructured Si Anodes for High Energy Lithium Ion Batteries. *Nano Today* **2012,** *7* (5), 414-429.
15. Shen, X.; Tian, Z.; Fan, R.; Shao, L.; Zhang, D.; Cao, G.; Kou, L.; Bai, Y., Research Progress on Silicon/Carbon Composite Anode Materials for Lithium-Ion Battery. *J. Energy Chem.* **2018,** *27* (4), 1067-1090.
16. Dufficy, M. K.; Khan, S. A.; Fedkiw, P. S., Galactomannan Binding Agents for Silicon Anodes in Li-Ion Batteries. *J. Mater. Chem. A* **2015,** *3* (22), 12023-12030.
17. Kwon, T. W.; Choi, J. W.; Coskun, A., The Emerging Era of Supramolecular Polymeric Binders in Silicon Anodes. *Chem. Soc. Rev.* **2018,** *47* (6), 2145-2164.
18. Morris, M. A.; An, H.; Lutkenhaus, J. L.; Epps, T. H., Harnessing the Power of Plastics: Nanostructured Polymer Systems in Lithium-Ion Batteries. *ACS Energy Lett.* **2017,** *2* (8), 1919-1936.
19. Chou, S. L.; Pan, Y.; Wang, J. Z.; Liu, H. K.; Dou, S. X., Small Things Make a Big Difference: Binder Effects on the Performance of Li and Na Batteries. *Phys. Chem. Chem. Phys.* **2014,** *16* (38), 20347-59.
20. Kwon, T. W.; Jeong, Y. K.; Lee, I.; Kim, T. S.; Choi, J. W.; Coskun, A., Systematic Molecular-Level Design of Binders Incorporating Meldrum's acid for Silicon anodes in Lithium Rechargeable Batteries. *Adv. Mater.* **2014,** *26* (47), 7979-85.
21. Magasinski, A.; Zdyrko, B.; Kovalenko, I.; Hertzberg, B.; Burtovyy, R.; Huebner, C. F.; Fuller, T. F.; Luzinov, I.; Yushin, G., Toward Efficient Binders for Li-Ion Battery Si-Based Anodes: Polyacrylic Acid. *ACS Appl. Mater. Interfaces* **2010,** *2* (11), 3004-10.

22. Komaba, S.; Shimomura, K.; Yabuuchi, N.; Ozeki, T.; Yui, H.; Konno, K., Study on Polymer Binders for High-Capacity SiO Negative Electrode of Li-Ion Batteries. *J. Phys. Chem. C* **2011,** *115* (27), 13487-13495.
23. Li, J.; Lewis, R. B.; Dahn, J. R., Sodium Carboxymethyl Cellulose: A Potential Binder for Silicon Electrodes. *Electrochem. Solid-State Lett.* **2007,** *10* (2), A17– A20.
24. Kovalenko, I.; Zdyrko, B.; Magasinski, A.; Hertzberg, B.; Milicev, Z.; Burtovyy, R.; Luzinov, I.; Yushin, G., A Major Constituent of Brown Algae for Use in Silicon Anodes. *Science* **2011,** *7* (6052), 75-79.
25. Jeong, Y. K.; Kwon, T. W.; Lee, I.; Kim, T. S.; Coskun, A.; Choi, J. W., Hyperbranched Beta-Cyclodextrin Polymer as an Effective Multidimensional Binder for Silicon Anodes in Lithium Rechargeable Batteries. *Nano Lett.* **2014,** *14* (2), 864-70.
26. Kwon, T.-W.; Jeong, Y. K.; Deniz, E.; AlQaradawi, S. Y.; Jang Wook Choi, J. W.; Coskun, A., Dynamic Cross-Linking of Polymeric Binders based on Host-Guest Interactions for Silicon Anodes. *ACS Nano* **2015,** *9* (11), 11317–11324.
27. He, J.; Zhang, L., Polyvinyl Alcohol Grafted Poly (acrylic acid) as Water-Soluble Binder with Enhanced Adhesion Capability and Electrochemical Performances for Si Anode. *J. Alloys Compd.* **2018,** *763*, 228-240.
28. Wei, L.; Chen, C.; Hou, Z.; Wei, H., Poly (acrylic acid sodium) Grafted Carboxymethyl Cellulose as a High Performance Polymer Binder for Silicon Anode in Lithium Ion Batteries. *Sci. Rep.* **2016,** *6*, 19583.
29. Lopez, J.; Chen, Z.; Wang, C.; Andrews, S. C.; Cui, Y.; Bao, Z., The Effects of Cross-Linking in a Supramolecular Binder on Cycle Life in Silicon Microparticle Anodes. *ACS Appl. Mater. Interfaces* **2016,** *8* (3), 2318-24.
30. Chen, C.; Lee, S. H.; Cho, M.; Kim, J.; Lee, Y., Cross-Linked Chitosan as an Efficient Binder for Si Anode of Li-ion Batteries. *ACS Appl. Mater. Interfaces* **2016,** *8* (4), 2658-65.
31. Hlushko, R.; Hlushko, H.; Sukhishvili, S. A., A Family of Linear Phenolic Polymers with Controlled Hydrophobicity, Adsorption and Antioxidant Properties. *Poly. Chem.* **2018,** *9* (4), 506-516.
32. Xu, Z.; Ye, H.; Li, H.; Xu, Y.; Wang, C.; Yin, J.; Zhu, H., Enhanced Lithium Ion Storage Performance of Tannic Acid in LiTFSI Electrolyte. *ACS Omega* **2017,** *2* (4), 1273-1278.
33. Irem Erel-Unal, I.; Sukhishvili, S. A., Hydrogen-Bonded Multilayers of a Neutral Polymer and a Polyphenol. *Macromolecules* **2008,** *41* (11), 3962–3970.
34. Chen, Y. N.; Peng, L.; Liu, T.; Wang, Y.; Shi, S.; Wang, H., Poly(vinyl alcohol)-Tannic Acid Hydrogels with Excellent Mechanical Properties and Shape Memory Behaviors. *ACS Appl. Mater. Interfaces* **2016,** *8* (40), 27199-27206.
35. Zhang, H.; Hu, X.; Zhang, Y.; Wang, S.; Xin, F.; Chen, X.; Yu, D., 3D-crosslinked Tannic Acid/Poly(ethylene oxide) Complex as a Three-In-One Multifunctional Binder for High-Sulfur-Loading and High-Stability Cathodes in Lithium-Sulfur Batteries. *Energy Storage Materials* **2019,** *17*, 293-299.
36. Liu, X. H.; Zhong, L.; Huang, S.; Mao, S. X.; Zhu, T.; Huang, J. Y., Size-Dependent Fracture of Silicon Nanoparticles During Lithiation. *ACS Nano* **2012,** *6* (2), 1522-1531.

37. Shi, F.; Song, Z.; Ross, P. N.; Somorjai, G. A.; Ritchie, R. O.; Komvopoulos, K., Failure Mechanisms of Single-Crystal Silicon Electrodes in Lithium-Ion Batteries. *Nat. Commun.* **2016,** *7*, 11886.
38. Wang, L.; Liu, T.; Peng, X.; Zeng, W.; Jin, Z.; Tian, W.; Gao, B.; Zhou, Y.; Chu, P. K.; Huo, K., Highly Stretchable Conductive Glue for High-Performance Silicon Anodes in Advanced Lithium-Ion Batteries. *Adv. Func. Mater.* **2018,** *28* (3), 1704858-66.
39. Pollak, E.; Salitra, G.; Baranchugov, V.; Aurbach, D., In Situ Conductivity, Impedance Spectroscopy, and Ex Situ Raman Spectra of Amorphous Silicon During the Insertion Extraction of Lithium. *J. Phys. Chem. C* **2007,** *111* (30), 11437-11444.
40. Zhu, X.; Zhang, F.; Zhang, L.; Zhang, L.; Song, Y.; Jiang, T.; Sayed, S.; Lu, C.; Wang, X.; Sun, J.; Liu, Z., A Highly Stretchable Cross-Linked Polyacrylamide Hydrogel as an Effective Binder for Silicon and Sulfur Electrodes toward Durable Lithium-Ion Storage. *Adv. Func. Mater.* **2018,** *28* (11), 1705015-27.
41. Zhang, G.; Yang, Y.; Chen, Y.; Huang, J.; Zhang, T.; Zeng, H.; Wang, C.; Liu, G.; Deng, Y., A Quadruple-Hydrogen-Bonded Supramolecular Binder for High-Performance Silicon Anodes in Lithium-Ion Batteries. *Small* **2018**, e1801189.
42. Choi, S.; Tae-woo Kwon, T.-W.; Coskun, A.; Choi, J. W., Highly Elastic Binders Integrating Polyrotaxanes for Silicon Microparticles Anode in Li Ion Batteries. *Science* **2017,** *357* (6348), 279-283.
43. Ding, N.; Xu, J.; Yao, Y. X.; Wegner, G.; Fang, X.; Chen, C. H.; Lieberwirth, I., Determination of the Diffusion Coefficient of Lithium Ions in Nano-Si. *Solid State Ionics* **2009,** *180* (2-3), 222-225.
44. Mukherjee, R.; Krishnan, R.; Lu, T.-M.; Koratkar, N., Nanostructured Electrodes for High-Power Lithium Ion Batteries. *Nano Energy* **2012,** *1* (4), 518-533.
45. Elgrishi, N.; Rountree, K. J.; McCarthy, B. D.; Rountree, E. S.; Eisenhart, T. T.; Dempsey, J. L., A Practical Beginner's Guide to Cyclic Voltammetry. *J. Chem. Educ.* **2017,** *95* (2), 197-206.
46. Tian, M.; Wu, P., Nature Plant Polyphenol Coating Silicon Submicroparticle Conjugated with Polyacrylic Acid for Achieving a High-Performance Anode of Lithium-Ion Battery. *ACS Appl. Energy Mater.* **2019,** *2* (7), 5066-5073.
47. Kim, J. S.; Choi, W.; Cho, K. Y.; Byun, D.; Lim, J.; Lee, J. K., Effect of Polyimide Binder on Electrochemical Characteristics of Surface-Modified Silicon Anode for Lithium Ion Batteries. *J. Power Sources* **2013,** *244*, 521-526.
48. Lia, J.; Dahn, J. R., An In Situ X-Ray Diffraction Study of the Reaction of Li with Crystalline Si. *J. Electrochem. Soc.* **2007,** *154* (3), A156-A161
49. McDowell, M. T.; Lee, S. W.; Nix, W. D.; Cui, Y., 25th Anniversary Article: Understanding the Lithiation of Silicon and Other Alloying Anodes for Lithium-Ion Batteries. *Adv. Mater.* **2013,** *25* (36), 4966-85.
50. Liao, D.; Kuang, X.; Xiang, J.; Wang, X., A Silicon Anode Material with Layered Structure for the Lithium-Ion Battery. *J. Phys.: Conf. Ser.* **2018,** *986*, 012024-30.
51. Wu, H.; Chan, G.; Choi, J. W.; Ryu, I.; Yao, Y.; McDowell, M. T.; Lee, S. W.; Jackson, A.; Yang, Y.; Hu, L.; Cui, Y., Stable Cycling of Double-Walled Silicon

Nanotube Battery Anodes Through Solid-Electrolyte Interphase Control. *Nat. Nanotechnol.* **2012,** *7* (5), 310-5.
52. Bie, Y.; Yang, J.; Liu, X.; Wang, J.; Nuli, Y.; Lu, W., Polydopamine Wrapping Silicon Cross-linked with Polyacrylic Acid as High-Performance Anode for Lithium-Ion Batteries. *ACS Appl. Mater. Interfaces* **2016,** *8* (5), 2899-904.
53. Wang, C.; Wu, H.; Chen, Z.; McDowell, M. T.; Cui, Y.; Bao, Z., Self-healing Chemistry Enables the Stable Operation of Silicon Microparticle Anodes for High-Energy Lithium-Ion Batteries. *Nat. Chem.* **2013,** *5* (12), 1042-8.
54. Liu, Z.; Han, S.; Xu, C.; Luo, Y.; Peng, N.; Qin, C.; Zhou, M.; Wang, W.; Chen, L.; Okada, S., In situ Crosslinked PVA–PEI Polymer Binder for Long-Cycle Silicon anodes in Li-Ion Batteries. *RSC Adv.* **2016,** *6* (72), 68371-68378.
55. Chen, L.; Xie, X.; Xie, J.; Wang, K.; Yang, J., Binder Effect on Cycling Performance of Silicon/Carbon Composite Anodes for Lithium Ion Batteries. *J. Appl. Electrochem.* **2006,** *36* (10), 1099-1104.
56. Song, T.; Xia, J.; Lee, J. H.; Lee, D. H.; Kwon, M. S.; Choi, J. M.; Wu, J.; Doo, S. K.; Chang, H.; Park, W. I.; Zang, D. S.; Kim, H.; Huang, Y.; Hwang, K. C.; Rogers, J. A.; Paik, U., Arrays of Sealed Silicon Nanotubes as Anodes for Lithium Ion Batteries. *Nano Lett.* **2010,** *10* (5), 1710-6.
57. Peng, B.; Cheng, F.; Tao, Z.; Chen, J., Lithium Transport at Silicon Thin Film: Barrier for High-Rate Capability Anode. *J. Chem. Phys.* **2010,** *133* (3), 034701.
58. Rahman, M. A.; Song, G.; Bhatt, A. I.; Wong, Y. C.; Wen, C., Nanostructured Silicon Anodes for High-Performance Lithium-Ion Batteries. *Adv. Func. Mater.* **2016,** *26* (5), 647-678.
59. Hancock, K.; Becherer, J.; Hagen, M.; Joos, M.; Abert, M.; Müller, D.; Fanz, P.; Straach, S.; Tübke, J., Electrolyte Decomposition and Electrode Thickness Changes in Li-S Cells with Lithium Metal Anodes, Prelithiated Silicon Anodes and Hard Carbon Anodes. *J. Electrochem. Soc.* **2017,** *165* (1), A6091-A6106.
60. Jeong, J.-H.; Kim, K.-H.; Jung, D.-W.; Kim, K.; Lee, S.-M.; Oh, E.-S., High-Performance Characteristics of Silicon Inverse Opal Synthesized by the Simple Magnesium Reduction as Anodes for Lithium-Ion Batteries. *J. Power Sources* **2015,** *300*, 182-189.
61. Schroder, K. W.; Dylla, A. G.; Harris, S. J.; Webb, L. J.; Stevenson, K. J., Role of Surface Oxides in the Formation of Solid-electrolyte Interphases at Silicon Electrodes for Lithium-ion Batteries. *ACS Appl. Mater. Interfaces* **2014,** *6* (23), 21510-24.
62. Koo, B.; Kim, H.; Cho, Y.; Lee, K. T.; Choi, N. S.; Cho, J., A Highly Cross-Linked Polymeric Binder for High-Performance Silicon Negative Electrodes in Lithium Ion Batteries. *Angew. Chem. Int. Ed. Engl.* **2012,** *51* (35), 8762-7.
63. Nguyen, C. C.; Yoon, T.; Seo, D. M.; Guduru, P.; Lucht, B. L., Systematic Investigation of Binders for Silicon Anodes: Interactions of Binder with Silicon Particles and Electrolytes and Effects of Binders on Solid Electrolyte Interphase Formation. *ACS Appl. Mater. Interfaces* **2016,** *8* (19), 12211-20.
64. Li, Q.; Liu, X.; Han, X.; Xiang, Y.; Zhong, G.; Wang, J.; Zheng, B.; Zhou, J.; Yang, Y., Identification of the Solid Electrolyte Interface on the Si/C Composite

Anode with FEC as the Additive. *ACS Appl. Mater. Interfaces* **2019,** *11* (15), 14066-14075.
65. Schroder, K.; Alvarado, J.; Yersak, T. A.; Li, J.; Dudney, N.; Webb, L. J.; Meng, Y. S.; Stevenson, K. J., The Effect of Fluoroethylene Carbonate as an Additive on the Solid Electrolyte Interphase on Silicon Lithium-Ion Electrodes. *Chem. Mater.* **2015,** *27* (16), 5531-5542.
66. Xu, Y.; Swaans, E.; Chen, S.; Basak, S.; R. M. L. Harks, P. P.; Peng, B.; Zandbergen, H. W.; Borsa, D. M.; Mulder, F. M., A High-Performance Li-Ion Anode from Direct Deposition of Si Nanoparticles. *Nano Energy* **2017,** *38*, 477-485.
67. Xie, J.; Imanishi, N.; Zhang, T.; Hirano, A.; Takeda, Y.; Yamamoto, O., Li-Ion Diffusion in Amorphous Si Films Prepared by RF Magnetron Sputtering: A Comparison of Using Liquid and Polymer Electrolytes. *Mater. Chem. Phys.* **2010,** *120* (2-3), 421-425.
68. Chen, Z.; Wang, C.; Lopez, J.; Lu, Z.; Cui, Y.; Bao, Z., High-Areal-Capacity Silicon Electrodes with Low-Cost Silicon Particles Based on Spatial Control of Self-Healing Binder. *Adv. Energy Mater.* **2015,** *5* (8), 1401826-34.
69. Guo, J.; Sun, A.; Chen, X.; Wang, C.; Manivannan, A., Cyclability Study of Silicon–Carbon Composite Anodes for Lithium-Ion Batteries using Electrochemical Impedance Spectroscopy. *Electrochim. Acta* **2011,** *56* (11), 3981-3987.
70. Nguyen, C. C.; Seo, D. M.; Chandrasiri, K.; Lucht, B. L., Improved Cycling Performance of a Si Nanoparticle Anode Utilizing Citric Acid as a Surface-Modifying Agent. *Langmuir* **2017,** *33* (37), 9254-9261.

# CHAPTER IV

# MINIMIZING TWO-DIMENSIONAL $TI_3C_2T_X$ MXENE NANOSHEET LOADING FOR CARBON-FREE SILICON ANODES*

## Introduction

Lithium-ion batteries have become important power sources for small electronics such as mobile phones and laptops.[1, 2] However, current lithium-ion batteries still require improvements in energy density for electric vehicles and large-scale wind/solar power grids.[3, 4] In order to address these issues, researchers are working on improving the performance of the battery's electrodes.[5, 6] Conventionally, graphite is used as an anode material in lithium-ion batteries; however, it has a low theoretical capacity of 350 mAh/g.[6] On the other hand, silicon anodes have a very high theoretical capacity of 3579 mAh/g because they can store up to 3.75 $Li^+$ ions per silicon atom.[7, 8] Further, silicon has a low discharge potential (~0.2 V *vs.* $Li/Li^+$), and it is abundantly available in nature.[3, 9] In spite of these advantages, silicon faces several major drawbacks. Silicon undergoes 300 % volumetric expansion during lithiation which builds up internal stresses and causes pulverization. Silicon nanoparticles (diameter ≤150 nm) alleviate pulverization,[7, 10] but other issues affiliated with volumetric expansion still persist (*e.g.* delamination from the current collector,[1] unstable build-up of the solid electrolyte interphase (SEI),[11, 12] loss of electrical percolation[13]). This manifests as capacity fade and poor Coulombic efficiency.

To address the aforementioned issues, binders and conductive additives - over 30 wt% - are commonly added to silicon anodes.[14] These additives improve the overall function of the electrode, but they dilute the active silicon material. The challenge we

*Reprinted with permission from "Minimizing two dimensional $Ti_3C_2T_x$ MXene Nanosheet Lading in Carbon-Free Silicon Anodes", by Kasturi Sarang, Xioafei Zhao, Dustin Holta, Miladin Radovic, Micah J. Green Eun-Suok Oh, Rafael Verduzco, and Jodie L Lutkenhaus, Nanoscale., 2020, 12, 20699-20709. Copyright (2020) Royal Society of Chemistry.

explore here is the minimization of additives while preserving function and maximizing the amount of active silicon.

Several water-based polymeric binders have been studied for silicon anodes:[15, 16] polyacrylic acid,[17, 18] carboxymethyl cellulose,[19] alginate (Alg),[20] and polydopamine.[21] The general observation is that hydrogen bonding interactions between the binder and the hydroxyl (-OH) groups on silicon the surface bind the electrode together.

Another important electrode component is the conductive additive. Super P carbon black (CB) is the most commonly used conductive additive in silicon anodes.[22] Researchers have also explored several carbonaceous materials such as graphene,[23-25] carbon nanotubes,[22, 26] and carbon nanofibers.[27] However, CB and other carbonaceous materials are hydrophobic, which complicates water-based processing.

Recently, MXenes, have been explored as conducting additives in silicon anodes. MXenes are 2D nanosheets prepared by selectively extracting the "A" element from their corresponding three-dimensional MAX phases, where M represents an early transition metal, A is a group 13-16 element, and X is either a C and/or N.[28, 29] The most commonly examined MXene is $Ti_3C_2T_x$, which has a high conductivity (4600 S/cm), excellent $Li^+$-ion diffusion (~$10^{-10}$–$10^{-9}$ $cm^2/s$), and good mechanical properties.[30, 31] $Ti_3C_2T_x$ nanosheets are also redox active in the potential window of 0-3 V *vs.* $Li/Li^+$.[30, 32] MXenes are hydrophilic due to the presence of terminal hydroxyl (-OH) groups on their surface. These properties have been utilized to make water-based polymer-MXenes composites by simple mixing processes.[33-35] Here, we represent $Ti_3C_2T_x$ nanosheets as "MX" for simplicity.

The literature shows a theme in that huge quantities of MXenes and/or additional additives are needed to prepare functional silicon anodes, effectively lowering the active material (silicon) loading and the total electrode capacity. The capacity values listed in this paragraph are the ones reported for long-term battery cycling test. Kong *et al.*[36] made silicon electrodes with 66 wt% of MXenes along with additional binder and CB. The huge content of additives lowered the silicon content to 13 wt% in their electrode, which lowered the total electrode capacity (24.4 $mAh/g_{total}$ at C-rate of ~0.05 C). On the other hand, Zhu *et al.*[37] made electrodes with 43 wt% of silicon by adding 22 wt% MXenes and additional additives (binder and CB). These electrodes demonstrated a total capacity 740 $mAh/g_{total}$ at C-rate of ~0.1 C. Lastly, Zhang *et al.*[13] used 30 wt% MXenes (Si content = 70 wt%) to make silicon electrodes without adding any binder or additional carbon additives, and they demonstrated a total capacity of 1050 $mAh/g_{total}$ at C-rate of ~0.35 C.

There are a few reports which have utilized different approaches to minimize the dead weight (which includes binder and carbon additives) in silicon anodes.[38-41] We proposed that utilization of MXenes along with a suitable binder (without any additional carbon additives) will reduce this dead weight and ultimately increase the silicon content in electrode.

Here, we explored the minimization of MXene content in the pursuit of maximal silicon loading, while developing a fundamental understanding how MXenes behave in the electrode. Sodium alginate (Alg) was also added to the silicon electrodes because its -OH groups hydrogen bond with silicon[20] and MXenes. To evaluate the battery performance, we used cyclic voltammetry to study the lithiation kinetics of the silicon

anode, galvanostatic charge-discharge cycling to study the stability of the silicon electrode, and electrochemical impedance spectroscopy to determine the electrode impedance. We utilized scanning electron microscopy (SEM) along with energy dispersive X-ray spectroscopy (EDS) to observe the morphologies of electrodes. We also performed X-ray photo electron spectroscopy to characterize the SEI formed after battery cycling. By using MXenes, we increased the silicon content to 80 wt% and eliminated CB to yield a comparatively high capacity for silicon/MXene anodes.

**Materials**

Silicon nanoparticles (98+% purity, 50-70 nm size, 80-120 $m^2/g$ surface area) were acquired from US-research nanomaterials. Sodium alginate (Alg, 15-25 cP, 1 % in $H_2O$), 1 M lithium hexafluorophosphate ($LiPF_6$) in ethylene carbonate (EC):diethyl carbonate (DEC) (1:1) v/v, hydrochloric acid (HCl, ACS reagent 37 % w/w), dimethyl sulfoxide (DMSO, ReagentPlus, >99.5 %) were acquired from Sigma Aldrich. Lithium foil (0.75 mm thick x 19 mm wide), lithium fluoride (LiF, 98+ % purity), fluoroethylene carbonate (FEC), titanium (Ti, 44 µm average particle size, 99.5 % purity), aluminum (Al, 44 µm average particle size, 99.5 % purity), and titanium carbide (TiC) (2-3 µm average particle size, 99.5 % purity) were purchased from Alfa Aesar. Super P carbon black (0.04 µm particle size, 62 $m^2/g$ surface area), copper foil (length x width x thickness = 170 m x 280 mm x 9um) was purchased from MTI corporation. Polypropylene separator (19 mm diameter x 0.025 mm thick) was purchased from Celgard. Poly(vinylidenefluoride) (PVDF) filtration unit with pore size of 0.22 µm was purchased from Milipore (Millipore® SCGVU10RE Stericup™ GV).

## Methods

### *$Ti_3C_2T_x$ MXene nanosheet synthesis and composite binder preparation*

MXene synthesis was adopted from literature[42] and is detailed in Chapter I. In brief, the $Ti_3C_2T_x$ MXene layers were obtained by lithium fluoride + hydrochloric acid etching and DMSO delamination. X-ray diffraction (XRD) analysis (Bruker D8 powder X-ray diffractometer) and X-ray photo electron spectroscopy (XPS) (Omicron ESCA Probe, Omicron Nanotechnology) confirmed the successful synthesis nanosheets (Figure I-12). After synthesis, the MXenes were freeze dried to form a powder and then stored under vacuum at room temperature to prevent their oxidation. The morphology of the delaminated MXene nanosheets was characterized using scanning electron microscopy (SEM), as shown in Figure IV-1a. From atomic force microscopy (AFM, Figure I-13), the lateral nanosheet size was approximately 1 μm.

To prepare the conductive binder, freeze-dried MXenes were added to sodium alginate solution (1 wt% solution in water) and the mixture was bath-sonicated for one minute to form a homogenous dispersion as shown in Figure IV-2a. Two different Alg/MXene ratios were studied; Alg (90 %) + MX (10 %) and Alg (80 %) + MX (20 %).

### *Silicon anode preparation*

To synthesize silicon electrodes using the prepared composite binder, silicon nanoparticles and the composite binder with a mass ratio of Si:conductive binder = 80:20 were ball milled together in water to form a homogenous slurry. Thus, two different slurries were synthesized: Si/Alg/MX = 80/18/2 and 80/16/4 (by mass). The former resulted from the 90 wt% Alg + 10 wt% MXene composite binder, and the latter resulted

from the 80 wt% Alg + 20 wt% MXene composite binder. The slurry was doctor-bladed on copper foil using an automatic film applicator (Elcometer 4340 Automatic applicator) and the resulting film thickness after drying measured was around 8-10 µm. The electrodes were then dried at room temperature for 3-4 h and then under vacuum at room temperature for 2 days. After drying, 16 mm electrodes were punched. The active material loading was kept constant around 0.70±0.05 mg/cm$^2$. For control experiments, two set of electrodes were prepared: Si/Alg=80/20 and Si/Alg/CB=80/16/4. These compositions were chosen to keep the ratio of active material to inactive material constant.

***Four-point probe characterization***

Four-point probe (powered by Keithley 2000, 6221 and two 6514.) was used to determine the electronic conductivity. Four dispersions were prepared: 90 wt% Alg + 10 wt% MXenes or CB, 80 wt% Alg + 20 wt% MXenes or CB. These were drop-cast onto glass slides (3 cm x 3 cm) and dried in vacuum for 2 days.

***Fourier transform infrared spectroscopy***

Attenuated total reflection-Fourier transform infrared (ATR-FTIR) spectra were recorded using an IR Prestige 21 system (Shimadzu Corp.) using IRsolution v. 1.40 software. The solutions/dispersions used included MXenes (1mg/ml), Alg (1 mg/ml), 90 wt% Alg (1mg/ml) + 10 wt% MXenes (1 mg/ml), and 80 wt% Alg (1mg/ml) + 20 wt% MXenes (1 mg/ml). These samples were prepared by drop-casting onto Cu foil (12 mm diameter), followed by drying in vacuum for 2 days. To perform ATR-FTIR spectroscopy on Si/Alg/MX=80/16/4 composition, 12 mm diameter discs were punched from the slurry-cast Si/Alg/MX electrode. Silicon nanoparticles were characterized in its powder form.

***Scanning electron microscopy (SEM) and energy dispersive X-ray spectroscopy (EDS)***

SEM was carried out on a JEOL JSM SEM equipment with an accelerating voltage of 5 kV and a working distance of 15 mm. SEM was performed on fresh and cycled (50 cycles of charge-discharge) electrodes. For the cycled electrodes, the cell was disassembled in the glovebox, and the electrodes were washed with dichloromethane to remove the residual salt. These electrodes were then dried in a glovebox for 2-3 days and then in vacuum oven at room temperature for 3 days. EDS was performed on JEOL JSM SEM equipment with an accelerating voltage of 20 kV and working distance of 8 mm. The data acquisition and data processing for EDS was done using INCA software. For the microscope setup, the probe current and process time were optimized to obtain a deadtime of approximately 45 %. For quant optimization, the measurements were done on a reference copper tape which was placed besides the sample on sample holder.

***X-ray photoelectron spectroscopy***

X-ray photoelectron spectroscopy (XPS) was performed on fresh and cycled (50 cycles of charge-discharge) electrodes. The XPS spectra were obtained using an Omicron ESCA Probe Omicron ESCA Probe (Omicron Nanotechnology) with a monochromated Mg Ka radiation. The survey scans were conducted using a pass energy of 100–1,100 eV with steps of 1.0 eV and 50-ms dwell time. Curve fitting (using CasaXPS software) was conducted using a Gaussian-Lorentzian peak shape after Shirley-type background correction.

***Electrochemical characterization***

For electrochemical characterization, two-electrode cells were assembled inside an argon-filled glovebox (MBraun Labstar 1200). 16 mm punched electrodes were used as working electrodes and lithium metal foil (16 mm) was employed as the counter and reference electrode. Two Celgard polypropylene discs (19 mm diameter, thickness) were used as separators. 1 M $LiPF_6$ in EC:DEC with 10 wt% FEC was used as the electrolyte. Galvanostatic charge-discharge cycling, rate capability, and cyclic voltammetry were performed using an Arbin Instrument (Arbin Instruments, HPT-100mA). The voltage range was 0.01 V to 1 V *vs.* $Li/Li^+$, and the charge-discharge currents were calculated based on the theoretical capacity of silicon (3579 mAh/g). For galvanostatic cycling, the electrodes were cycled in constant current (CC) – constant voltage (CV) mode for the first 5 cycles to condition the electrode. In the CC-CV mode, electrodes were first lithiated at 0.1 C until the potential reached 0.01 V (CC mode) and then the potential was held constant at 0.01 V until the current had decayed to 0.01 C. The capacities are reported based on mass of silicon, unless mentioned. Electrochemical impedance spectroscopy (EIS) was performed on fresh and on cycled electrodes using a Gamry Potentiostat/Galvanostat (Gamry Interface 1000, Gamry Instruments). EIS was performed using a 50 mV AC amplitude from 100kHz to 5 mHz at 0.2 V *vs.* $Li/Li^+$. These electrochemical characterizations were performed thrice on each electrode studied to verify repeatability of results observed.

***Specific energy and power calculations***

Specific energy was calculated by multiplying the first cycle specific discharge capacity ($Ah/kg_{Si}$ or $Ah/kg_{total}$ at that C-rate) by the potential window of silicon anode studied. Specific power was calculated by multiplying current density (A/kg) with the potential window of silicon anode studied. It was noted that some reports consider silicon and the conductive matrix as the active material, but here we considered "only silicon" as the active material.

$$\text{Specific energy } \left(\frac{\text{Wh}}{\text{kg}}\right) = \text{Discharge capacity } \left(\frac{\text{Ah}}{\text{kg}}\right) \times \text{Potential window (V)} \quad \ldots 3.1$$

$$\text{Specific power } \left(\frac{\text{W}}{\text{kg}}\right) = \text{Current density } \left(\frac{\text{A}}{\text{kg}}\right) \times \text{Potential window (V)} \quad \ldots 3.2$$

**Results and discussions**

Composite binders were prepared from freeze-dried MXenes dispersed in a 1 wt% Alg solution in water by bath sonication (Figure IV-2a). Two composite binder compositions were investigated: 90 wt% Alg + 10 wt% MXenes and 80 wt% Alg + 20 wt% MXenes. These compositions were selected because they represented the minimal amount of MXene additives required to achieve reasonable electrochemical performance, shown below. The resulting Alg+Mxene dispersions were stable and homogeneous, whereas a similar CB/Alg mixture did not disperse well, (Figure IV-2b). This result may be attributed to hydrogen bonding between -OH groups on the hydrophilic MXene nanosheet surface and the Alg. In contrast, CB does not possess hydrogen bonding groups and is hydrophobic.

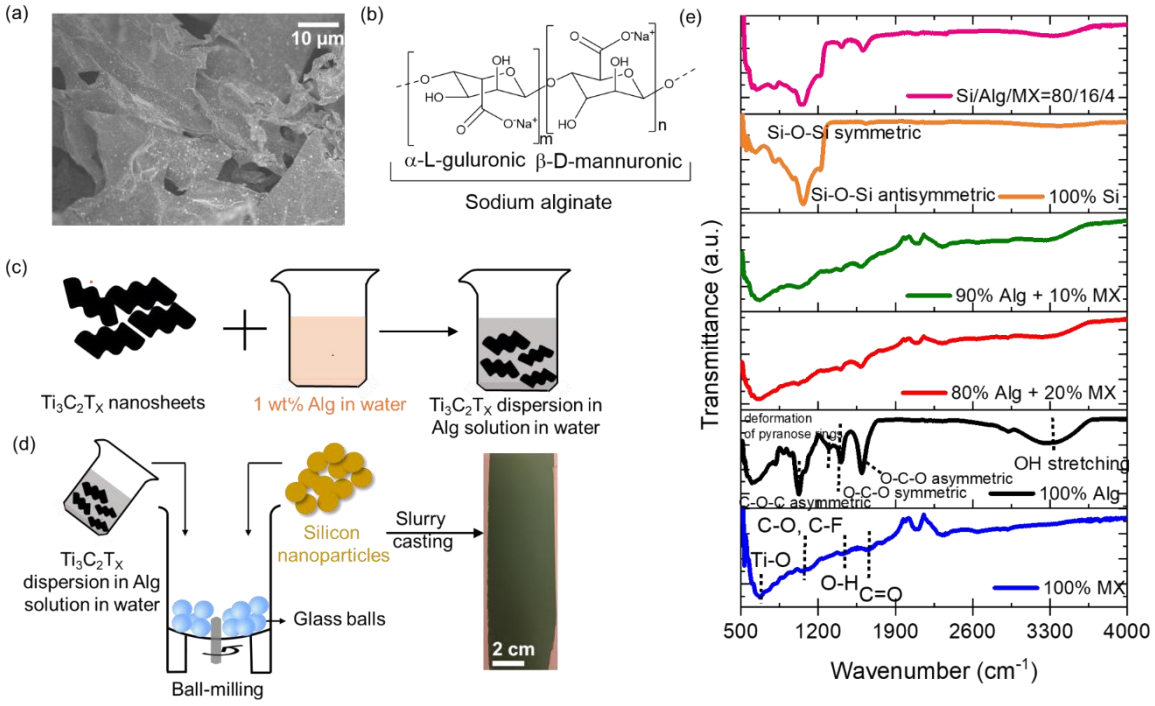


Figure IV-1. (a) Scanning electron microscopy (SEM) image of $Ti_3C_2T_x$ nanosheet, (b) schematic of sodium alginate (Alg), (c) schematic of a MXene dispersion in aqueous Alg solution, (d) schematic of electrode fabrication process by simple slurry casting method, and (e) FTIR spectra of MXenes, silicon nanoparticles, Alg, 90 wt% Alg + 10 wt% MX, 80 wt% Alg + 20 wt% MX, and Si/Alg/MX=80/16/4 wt%.

To further analyze the composite binder, attenuated total reflection – Fourier transform infrared spectroscopy (ATR-FTIR) analysis was performed on drop-cast Alg, drop-cast MXene nanosheets, drop-cast composite binders, silicon nanoparticles, and Si/Alg/MX=80/16/4, Figure IV-1e. The Alg FTIR spectrum demonstrated absorbance peaks at 3300 $cm^{-1}$ (-OH stretching), 1600 $cm^{-1}$ (O-C-O asymmetric vibration), 1420 $cm^{-1}$ (O-C-O symmetric vibration), ~1300 $cm^{-1}$ (deformation of pyranose rings), 1020 $cm^{-1}$ (C-O-C symmetric vibrations), consistent with literature.[20, 43] The MXene FTIR spectrum demonstrated absorbance peaks at 1050 $cm^{-1}$ (C-O), 1100 $cm^{-1}$ (C-F), and 1395 $cm^{-1}$ (O-H), which confirms the presence of terminal surface groups on MXenes, particularly

hydroxyl groups.[44, 45] The FTIR spectra of both Alg+MX composite binders demonstrated peaks from the constituent species as well as a slight reduction in the -OH stretching peak area, which might be attributed to hydrogen bonding between the two species.[46]

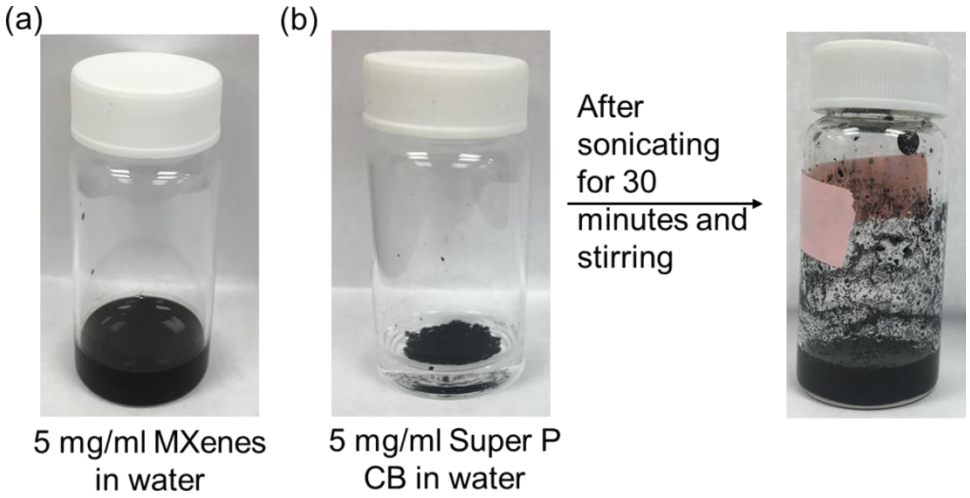


Figure IV-2. (a) Digital image of freeze-dried MXene nanosheets in 1 wt% sodium alginate solution in water. A minute of bath sonication is enough to form a stable dispersion of MXenes in water. (b) Digital image of super P carbon black (CB) in 1 wt% sodium alginate solution in water. Sonication and stirring for 30 minutes was required to somewhat disperse the Super P carbon black.

Silicon-based electrodes were fabricated from the two composite binders to create two electrodes bearing Si/Alg/MX mass compositions of 80/18/2 and 80/16/4. The former resulted from the 90 wt% Alg + 10 wt% MXenes composite binder, and the latter resulted from the 80 wt% Alg + 20 wt% MXene composite binder. In early screening experiments, we determined that the electrode with 4 wt% MXene nanosheets demonstrated higher capacities than the one with 2 wt% MXenes (Figure IV-3). This can be attributed to lower electronic conductivity of 90 wt% Alg + 10 wt% MXenes composite binder ($1 \times 10^{-6}$ S/cm) as compared to 80 wt% Alg + 20 wt% MXenes ($2.62 \times 10^{-4}$ S/cm). This shows that proper

balance between binder and conductive additive is essential to obtain optimum cycling performance. With the purpose of this investigation being to minimize the MXene loading, we did not explore other compositions. Thus, all further experiments focused upon the Si/Alg/MX composition of 80/16/4 (by mass), for which the active material loading was was 0.70±0.05 mg/cm$^2$. Other mass loadings of 0.3 to 2.2 mg/cm$^2$ are discussed further in the text.

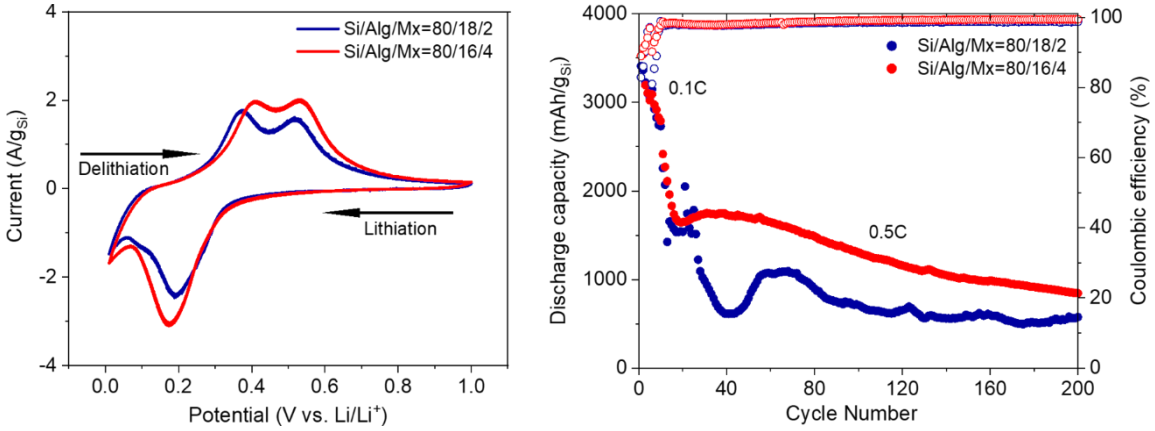


Figure IV-3. (a) Cyclic voltammogram at 0.1 mV/s (3$^{rd}$ cycle for each). Before CV, conditioning was performed at 0.1 C for three cycles. (b) Galvanostatic charge-discharge at 0.1 C in constant current-constant voltage (CC-CV) mode for 1$^{st}$ five cycles followed by 0.5 C in CC mode for the remaining 195 cycles. Electrodes with different MXene content were compared. Electrode with 4 wt% MXenes showed higher capacities than the one with 2 wt% MXenes.

To analyse the interactions between silicon nanoparticles, Alg binder, and MXene nanosheets, FTIR spectroscopy was performed (Figure IV-1e). The FTIR spectrum of Si/Alg/MX contained peaks from each of the three materials. The -OH stretching peak around 3300 cm$^{-1}$ can be attributed to hydrogen bonding interactions among the three species.[46]

The electrochemical performance of silicon electrodes was evaluated in lithium metal half-cells with 1 M $LiPF_6$ in EC:DEC with 10 wt% FEC as the electrolyte. The electrodes were first conditioned by three cycles of galvanostatic charge-discharge at 0.1 C to form an SEI (data not shown). Figure IV-4 shows the subsequent cyclic voltammograms (CVs) (for the third cycle) of Si/Alg=80/20, Si/Alg/CB=80/16/4, and Si/Alg/MX=80/16/4 electrodes at scan rate of 0.1 mV/s. The CV for Si/Alg shows a lithiation peak at 0.1 V and a broad delithiation peak at 0.4 V. Si/Alg also exhibited the lowest anodic current response compared to Si/Alg/CB and Si/Alg/MX, which we attribute to the sluggish kinetics and lower electrochemical activity caused by the absence of conductive additives. The CVs of Si/Alg/CB and Si/Alg/MX show distinct lithiation peaks at 0.2 V and two delithiation peaks at 0.4 and 0.6 V, which are consistent with those found in the literature.[47] Si/Alg/MX demonstrated highest anodic current response as compared to other two electrodes. Also, the potential difference between the lithiation and delithiation peaks for Si/Alg/MX was smaller than other two electrodes. This result indicates that MXene nanosheets provide a better formed electronic network in the electrode which lowers the degree of polarization.[37]

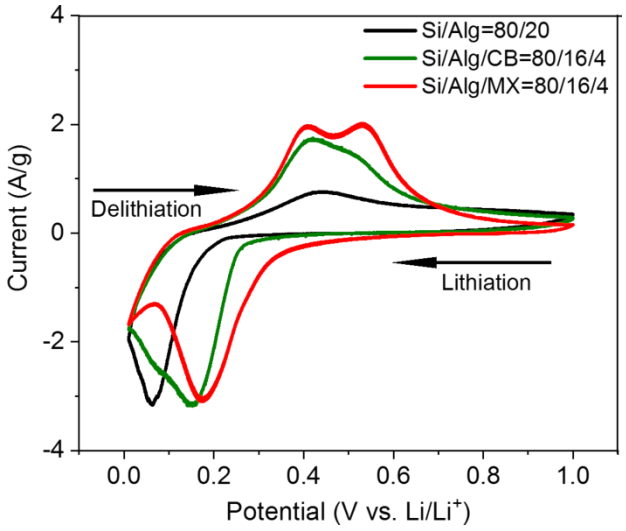


Figure IV-4. Cyclic voltammograms of Si/Alg=80/20, Si/Alg/CB=80/16/4, and Si/Alg/MX=80/16/4 at scan rate of 0.1 mV/s (third cycle is shown here). Cyclic voltammetry was performed for five cycles at 0.1 mV/s and the third cycle for each is shown here. Before CV, conditioning was performed at 0.1 C for three cycles.

MXenes are electrochemically active in the potential window of 0 V to 3 V *vs.* $Li/Li^+$,[31, 32, 48] but no additional redox peaks were observed here for Si/Alg/MX. This absence is attributed to the low MXene concentration (4 wt% in the entire electrode), such that the dominating response was that of silicon.

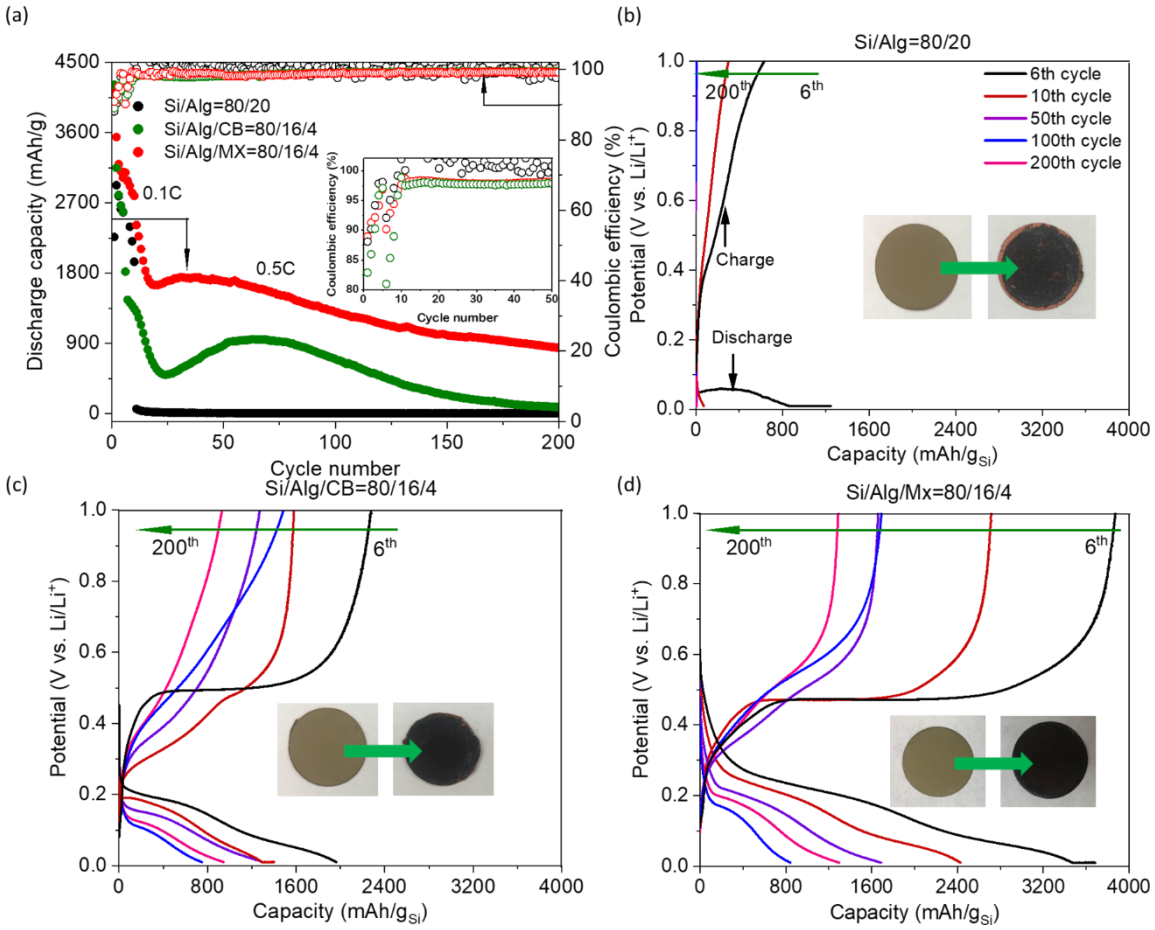


Figure IV-5. (a) Comparison of galvanostatic cycling performance of Si/Alg=80/20, Si/Alg/CB=80/16/4, and Si/Alg/MX=80/16/4 electrodes. Inset shows plot of Coulombic efficiency vs. cycle number for 50 charge-discharge cycles. Voltage profiles at the $6^{th}$ , $10^{th}$ , $50^{th}$ , $100^{th}$ , and $200^{th}$ cycles (all at 0.5 C) for (b) Si/Alg=80/20, (c) Si/Alg/CB=80/16/4, and (d) Si/Alg/MX=80/16/4 electrode. The digital images are of electrodes before and after 200 cycles of charge-discharge. Voltage profile for first cycle at 0.1 C is shown in Figure IV-6.

Next, we evaluated the long-term cycling performance of Si/Alg, Si/Alg/CB, and Si/Alg/MX electrodes, in which the electrodes were cycled at 0.1C (5 times) and then at 0.5 C (195 times). Si/Alg/MX demonstrated the highest capacity throughout cycling, followed by Si/Alg/CB and Si/Alg (Figure IV-5a). All electrodes exhibited a drop in capacity for the first few cycles due to the increase in C-rate and also due to the gradual

build-up of the SEI.[49] Figure IV-6 shows the galvanostatic response of the first cycle plot at 0.1 C; all three electrodes show a broad plateau at ~0.2 V *vs.* $Li/Li^+$ assigned to the conversion of crystalline silicon to lithiated amorphous silicon.[1, 50, 51] Si/Alg, Si/Alg/CB, and Si/Alg/MX demonstrated initial capacities of 2170, 3320, 3800 $mAh/g_{Si}$, respectively. The initial Coulombic efficiency (ICE) of Si/Alg/MX was the highest (~80%), followed by Si/Alg (~78%) and Si/Alg/CB (~64%). The very low ICE of Si/Alg/CB can be attributed to lithium trapping associated with the amorphous carbon.[39]

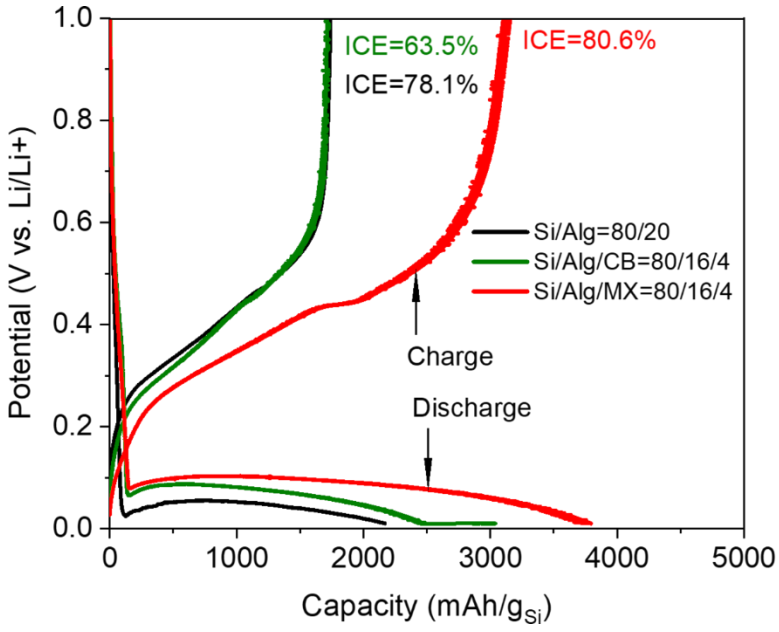


Figure IV-6. Voltage profile of Si/Alg=80/20, Si/Alg/CB=80/16/4, and Si/Alg/MX=80/16/4 for the 1st cycle at 0.1 C. Selected remaining cycles from 6th to 200th cycle at 0.5 C are shown in Figure IV-5b-d.

The galvanostatic voltage responses for selected cycles (6th to 100th) are shown in Figure IV-5b-d. Si/Alg showed a dramatic decrease in capacity after the first cycle owing to delamination from the current collector after 200 cycles (digital images of electrodes in Figure IV-5b-d). Si/Alg/CB showed higher capacities than Si/Alg for 150 cycles which

then dropped to almost 50 $mAh/g_{Si}$ at the end of 200 cycles. On the other hand, Si/Alg/MX showed the highest capacity and most consistent voltage profiles throughout the 200 cycles. The capacities can be further improved by pre-lithiation, tuning silicon particles, modifying MXene surface, modifying electrolyte, and so on which is beyond the scope of his study.

The superior cycling performance for Si/Alg/MX implies that 4 wt% MXenes is sufficient to sustain long term cycling without delamination. We attribute this result to hydrogen bonding interactions among -OH groups on the MXene nanosheet surface, the silicon surface, and Alg binder. The satisfactory capacity for Si/Alg/MX is further attributed to improved electrical connections afforded by the high aspect ratio MXene nanosheets. In contrast, the capacity of the Si/Alg/CB electrode was inferior, which we attribute to insufficient electrical connections because of possible aggregation of the hydrophobic CB particles. Overall, this highlights the importance of fabricating silicon anodes with hydrophilic additives, rather than hydrophobic ones, when water is the processing medium.

To further understand the improved performance of the Si/Alg/MX electrode, we measured the electronic conductivities of Alg/MX and Alg/CB polymer composites (without silicon nanoparticles). This approach isolates the contribution of the additives alone without interference from the silicon active material. The sample with 80 wt% Alg and 20 wt% MXene nanosheets showed a higher electronic conductivity ($2.62 \times 10^{-4}$ S/cm) as compared to the sample consisting of 80 wt% Alg and 20 wt% CB ($1.82 \times 10^{-4}$ S/cm). This result is attributed to the higher conductivity of MXenes (4600 S/cm)[52] in contrast to

CB (50-100 S/cm).[53] This also confirms our observation of higher capacities achieved for Si/Alg/MX as opposed to Si/Alg/CB (Figure IV-5).

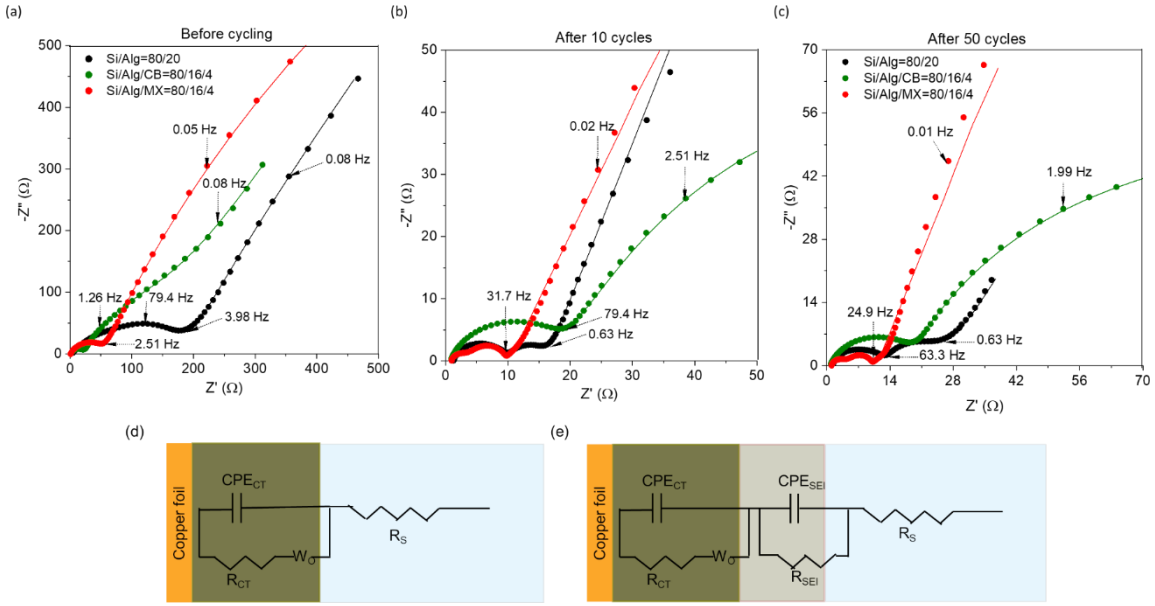


Figure IV-7. Nyquist plot for (a) Si/Alg=80/20, (b) Si/Alg/CB=80/16/4, and (c) Si/Alg/MX=80/16/4 electrode. Electrochemical impedance spectroscopy was performed with a frequency range from 100 kHz to 5 mHz with an amplitude of 10 mV at potential of 0.2 V. Equivalent circuits used for fitting the Nyquist data obtained from EIS (d) before cycling (one time constant) and (e) after cycling (two time constants). The dotted lines represent the experimental data and solid lines represent the equivalent circuit model fit to the data.

We next performed electrochemical impedance spectroscopy (EIS) on Si/Alg, Si/Alg/CB, and Si/Alg/MX electrodes before and after 10 and 50 cycles of charge-discharge to monitor changes in impedance at 0.2 V. Figure IV-7a-c shows Nyquist plots with depressed semicircles in both the high and medium frequency regions and a Warburg tail in the low frequency region. For data before cycling (Figure IV-7a), only one semi-circle was observed, which is indicative of a charge transfer resistance ($R_{CT}$). For data after cycling (Figure IV-7b-c), two semicircles are observed; the one in the high frequency

region is attributed to SEI formation and the one in the medium frequency region is attributed to $R_{CT}$. To analyze the physical significance of electrochemical process occurring in these electrodes an equivalent circuit was employed. The circuit shown in Figure IV-7d was fit to the data before cycling, and the circuit shown in Figure IV-7e was fit to the data after cycling. The equivalent circuits consisted of an ohmic resistance ($R_O$), which is the resistance to $Li^+$ ion conduction through the bulk solution to the electrode-electrolyte interface and to the electronic conduction through the electrode to the copper foil-electrode interface; $R_{CT}$ due to the reaction between the silicon and $Li^+$ ions; a constant phase element (*CPE*) due to the electrode-electrolyte interface; a resistance due to the SEI layer ($R_{SEI}$); a *CPE* due to the SEI layer-electrolyte interface; and a Warburg impedance ($W_O$) related to solid-state $Li^+$ ion diffusion.

Table IV-1. Equivalent circuit fit values for the Nyquist plot obtained from EIS performed on Si/Alg=80/20, Si/Alg/CB=80/16/4, and Si/Alg/MX=80/16/4 electrodes before cycling, after 10 and 50 cycles of charge-discharge.

| Before cycling | | | | | | | |
|---|---|---|---|---|---|---|---|
| | $R_O$ (Ω) | $R_{CT}$ (Ω) | $CPE_{CT}$ ($x10^{-5}$ F) | $R_{SEI}$ (Ω) | $CPE_{SEI}$ ($x10^{-5}$ F) | σ (Ω/s) | $D_{Li^+}$ ($x10^{-12}$ $cm^2/s$) |
| Si/Alg | 3.3 | 116 | 3.5 | - | - | - | - |
| Si/Alg/CB | 0.8 | 104 | 400 | - | - | - | - |
| Si/Alg/MX | 1.2 | 51.4 | 6.3 | - | - | - | - |
| After 10 cycles | | | | | | | |
| Si/Alg | 1.2 | 5.1 | 121 | 7.8 | 4.3 | 9.1 | 3.26 |
| Si/Alg/CB | 0.7 | 17.9 | 8.7 | 107 | 339 | 50.7 | 0.15 |
| Si/Alg/MX | 1.0 | 2.5 | 1.4 | 5.6 | 18.4 | 9.4 | 20.2 |
| After 50 cycles | | | | | | | |
| Si/Alg | 1.2 | 18.9 | 830 | 10.2 | 6.4 | 6.7 | 0.78 |
| Si/Alg/CB | 1.0 | 1.4 | 3.6 | 139 | 329 | 47.3 | 0.08 |
| Si/Alg/MX | 1.0 | 3.0 | 0.9 | 5.4 | 22.5 | 8.4 | 26.9 |

Table IV-1 summarizes the equivalent circuit modelling. Si/Alg/MX demonstrated the lowest $R_{CT}$ as compared to Si/Alg and Si/Alg/CB, both before and after cycling. All electrodes showed a drop in $R_{CT}$ after cycling because of gradual electrolyte penetration.[54] After 10 cycles, the total resistance of Si/Alg/MX was 8.0 Ω and those for Si/Alg and Si/Alg/CB were 12.9 Ω and 28.6 Ω, respectively. After 50 cycles, all electrodes demonstrated an increase in resistance. However, the increase was more pronounced for Si/Alg (65%) and Si/Alg/CB (71%) as compared to Si/Alg/MX (48%). The solid-state diffusion coefficient of each electrode was calculated[55] using EIS and galvanostatic cycling results following previous reports[56]. As seen in Table IV-1, the $Li^+$ ion diffusion coefficient after 50 cycles of the Si/Alg/MX electrode (20.2 x $10^{-12}$ $cm^2/s$) was much higher than that of Si/Alg and Si/Alg/CB electrodes.

The low $R_{CT}$ and high $Li^+$ ion diffusion coefficient for Si/Alg/MX is a result of the higher conductivity of the electrode resulting from a better interconnected network due to MXene nanosheets. The high aspect ratio of the MXene nanosheets[13] allows for better connection between adjacent nanosheets even when only 4 wt% MXene nanosheets were used in the entire electrode. On the other hand, CB has a lower aspect ratio and thus lacks the ability to form a well-developed electronically connected path for such low concentrations. These properties ultimately led to improved performance of Si/Alg/MX over the control electrodes.

Typical scanning electron microscopy (SEM) images of Si/Alg, Si/Alg/CB and Si/Alg/MX electrodes before and after cycling are shown in Figure IV-8. All electrodes

before cycling have a very similar morphology. MXene nanosheets are visible at the Si/Alg/MX surface and in the cross-section, which was further confirmed by the presence of titanium (Ti) in the energy dispersive X-ray spectroscopy (EDS) images (Figure IV-9). After cycling, all electrodes exhibited an SEI layer; however, a more uniform SEI layer was formed on the Si/Alg/MX electrode, as opposed to patchy SEI formation on the other two electrodes. Although MXene nanosheets were not visible in the Si/Alg/MX SEM images after cycling because of the SEI layer, EDS images do show the presence of Ti throughout electrode (Figure IV-9).

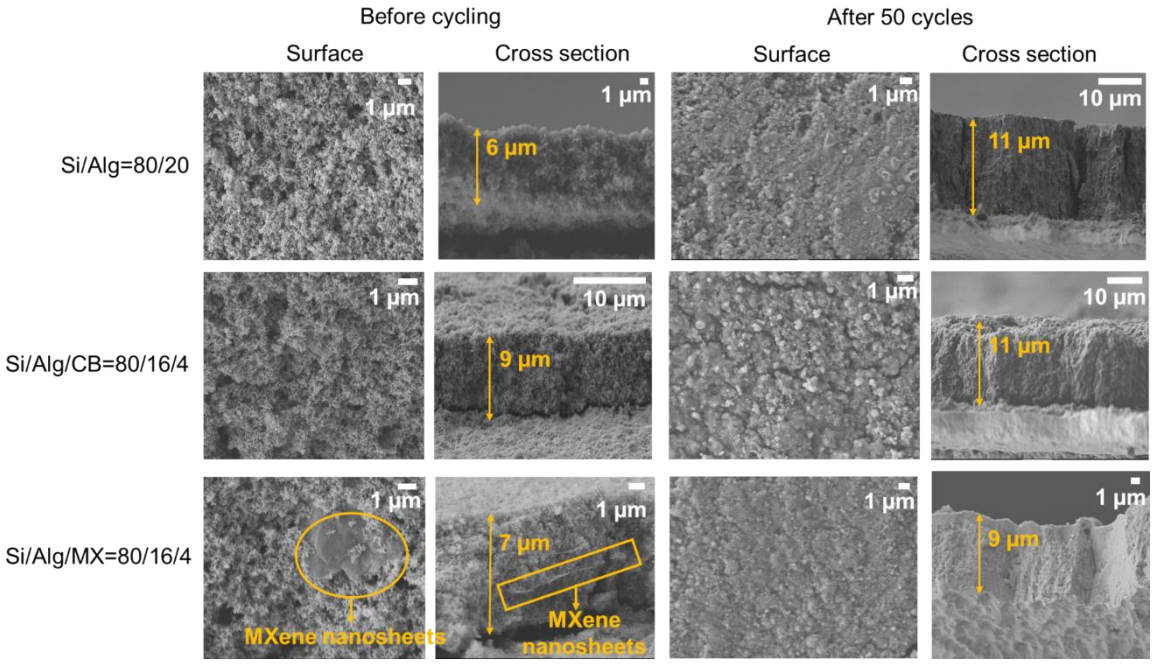


Figure IV-8. Scanning electron microscopy (SEM) images (both surface and cross section) of Si/Alg=80/20, Si/Alg/CB=80/16/4, and Si/Alg/MX=80/16/4 electrodes before and after 50 cycles of charge-discharge.

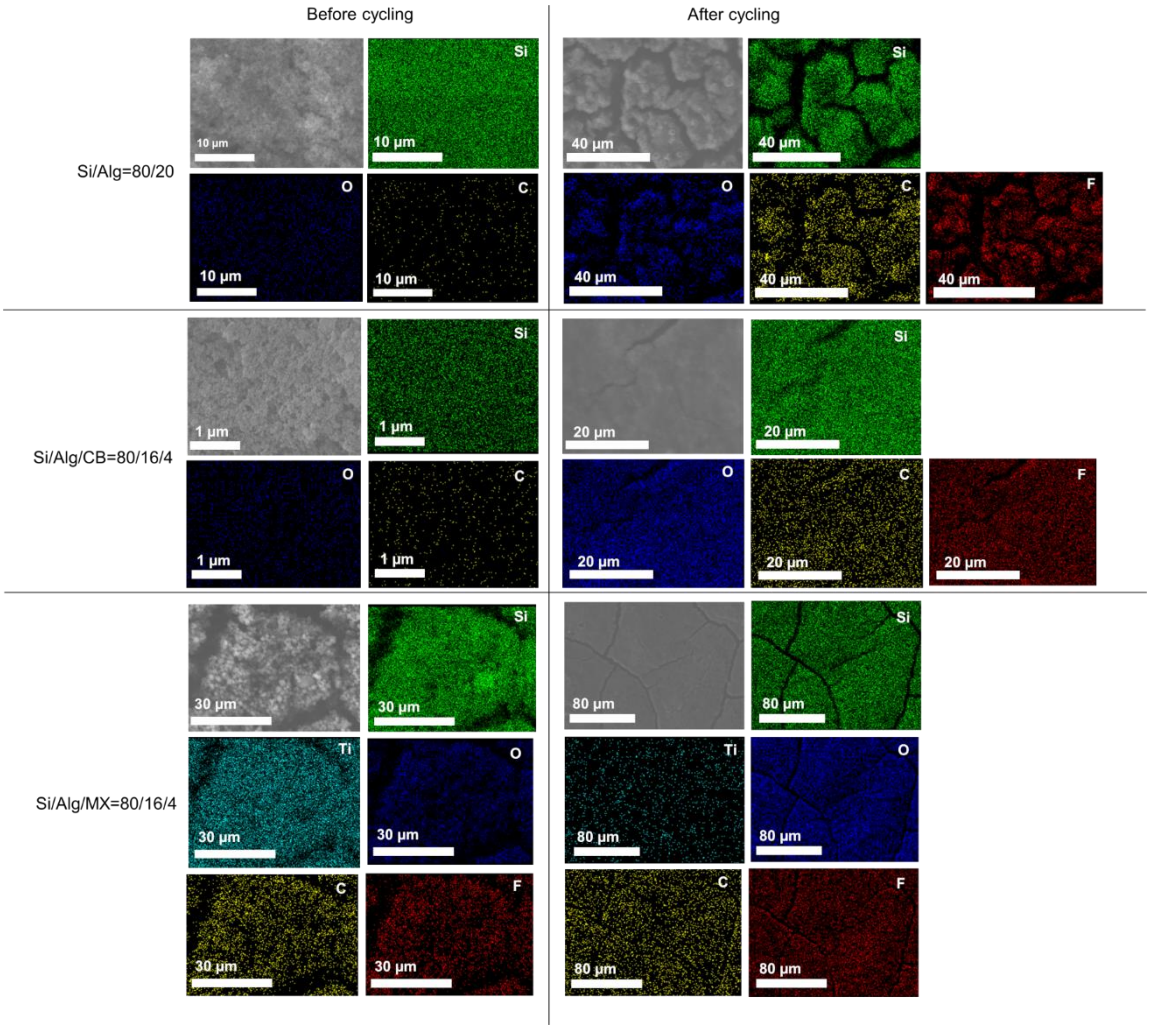


Figure IV-9. Energy dispersive X-ray spectroscopy (EDS) of Si/Alg=80/20, Si/Alg/CB=80/16/4, and Si/Alg/MX=80/16/4 electrodes before and after 50 cycles of charge-discharge.

We also performed X-ray photoelectron spectroscopy (XPS) on our electrodes before and after cycling. Before cycling, XPS survey scans of all electrodes show presence of Si, C, and O elements (Figure IV-10a). The Ti peak is not distinctly observed in the survey scan for Si/Alg/MX probably because the few MXene nanosheets are buried deep into the electrode. After cycling, XPS survey scans of all electrodes show fluorine (F) and

lithium (Li) peaks, which are representative of an SEI layer (Figure IV-10b). We further performed high resolution scans on each of these elements and deconvoluted them which are detailed in the published manuscript.[57]

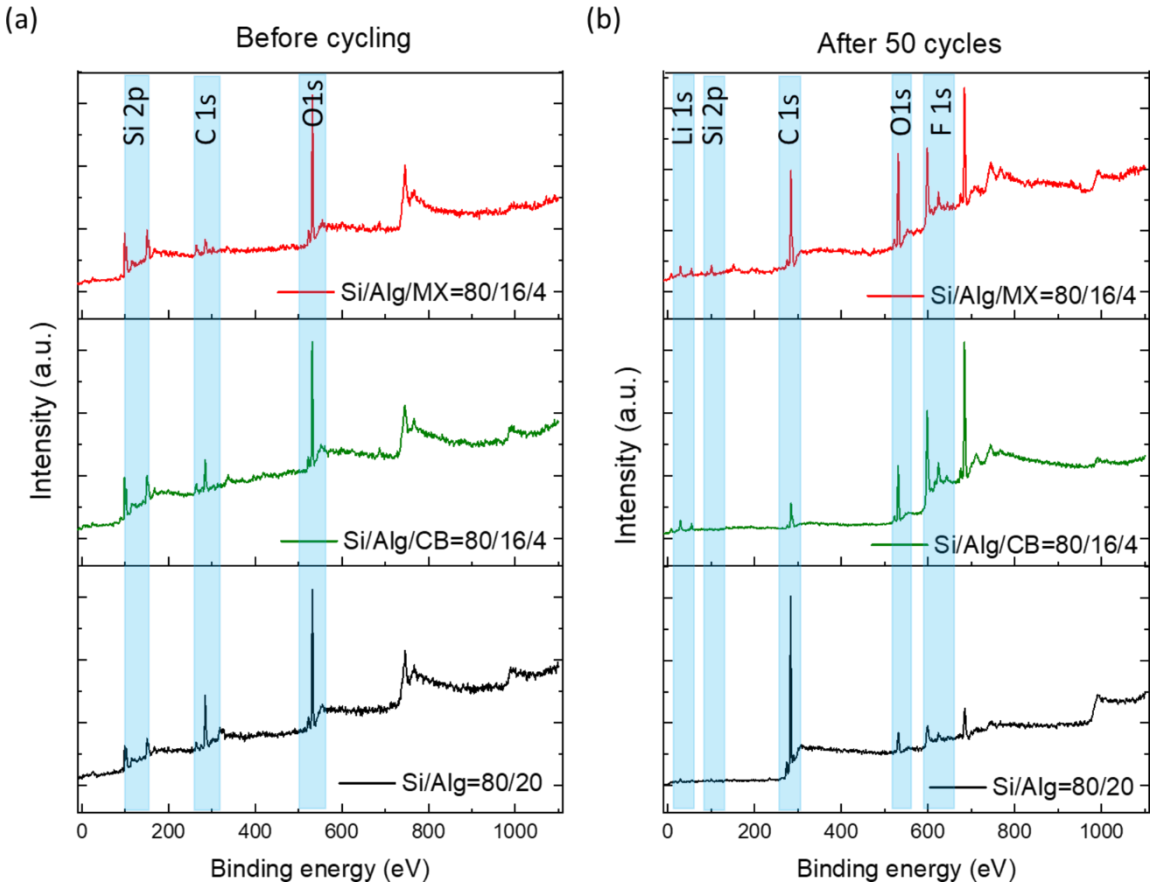


Figure IV-10. X-ray photoelectron spectroscopy survey scans for Si/Alg=80/20, Si/Alg/CB=80/16/4, and Si/Alg/MX=80/16/4 electrodes (a) before and (b) after 50 cycles of charge-discharge.

Figure IV-11 shows the rate performance of the silicon electrodes at different C-rates ranging from 0.1 C to 5 C. The Si/Alg electrode exhibited the poorest rate performance, in which the capacity dropped to 10 mAh/$g_{Si}$ at C-rates above 0.2 C. Comparing Si/Alg/CB and Si/Alg/MX electrodes, the latter showed higher capacities;

specifically, the discharge capacity was 1050 mAh/$g_{Si}$ at 1 C for Si/Alg/MX and 700 mAh/$g_{Si}$ for Si/Alg/CB. All electrodes showed a drop in capacity with increase in C-rate due to diffusion limitation of $Li^+$ ions.[58] The capacity recovery (when C-rate was bought back to 0.1 C) of Si/Alg/MX was around 71%, as compared to 65% for Si/Alg/CB and 60% for Si/Alg. These results emphasize the improved rate capability and higher stability of Si/Alg/MX electrodes. The improved rate performance is also supported by our EIS results (Figure IV-7a-c, Table IV-1), for which Si/Alg/MX electrodes exhibited the lowest $R_{CT}$ and the highest $Li^+$ ion diffusion coefficient.

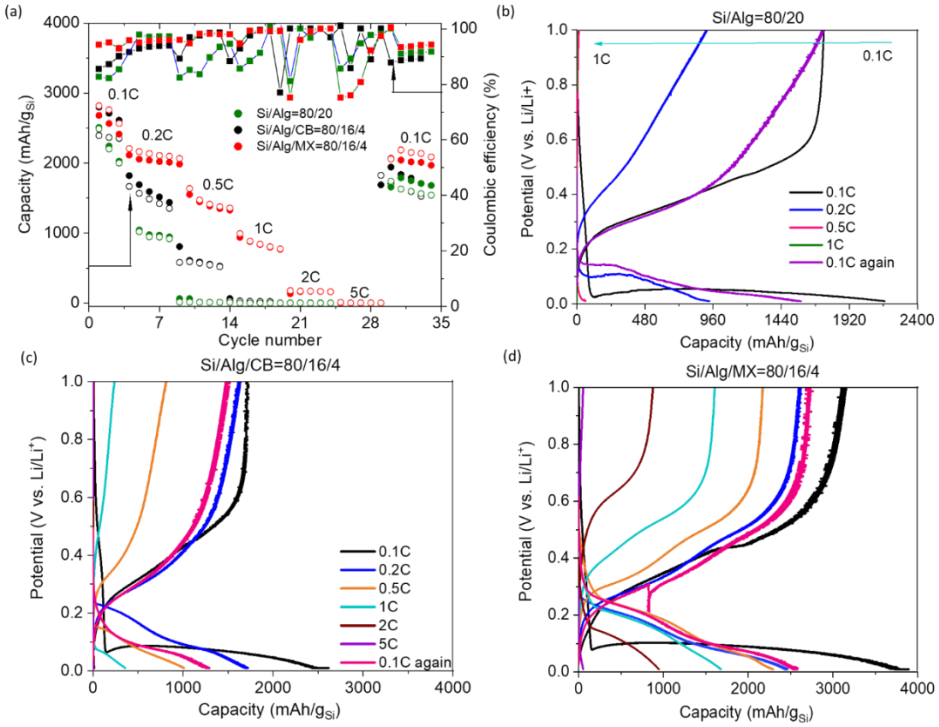


Figure IV-11. (a) Rate performance of silicon electrodes at different C-rates ranging from 0.1 C to 5 C. The C-rate was brought back to 0.1 C again to determine the capacity recovery. Voltage profiles for the 1st cycle at every C-rate for (b) Si/Alg=80/20, (c) Si/Alg/CB=80/16/4, and (d) Si/Alg/MX=80/16/4 electrode. The voltage profiles at 2 C and 5 C for Si/Alg are not shown because very few data points were collected at those C-rates.

We constructed a Ragone plot (Figure IV-12a) to compare the specific energy and power (normalized by total electrode mass) of our silicon electrodes to selected literature.[13, 36, 37, 39, 59-63] We first compare our results to silicon electrodes using reduced graphene oxide (rGO) nanosheets[60-62] or CNTs[39] as either conductive additives. The specific energy corresponding to the specific power of our silicon electrodes with only 4 wt% MXenes was comparable to those reported in literature with much higher rGO contents. However, there were a few exceptions: one reported by Chang *et al.* in which they made Si/rGO=76/24 electrodes, other reported by Assresahegn *et al.* where they made 90 wt% PAA grafted silicon with 10 wt% rGO, and another reported by Wang *et al.* in which CNT-C microscrolls were added to achieve a very high silicon loading of 85 wt%.[39] To the best of our knowledge, there are no reports on silicon anodes with less than 10 wt% rGO as conductive additive probably because of poor dispersibility in water resulting in non-uniform electrode conductivity. Overall, this comparison implies that rGO nanosheets may be replaced with MXene nanosheets for silicon anodes in certain applications. The possible benefit is that MXenes are natively hydrophilic, making them ideal for water-based silicon anode processing. In contrast, rGO is hydrophobic and its formation requires a harsh reduction step.

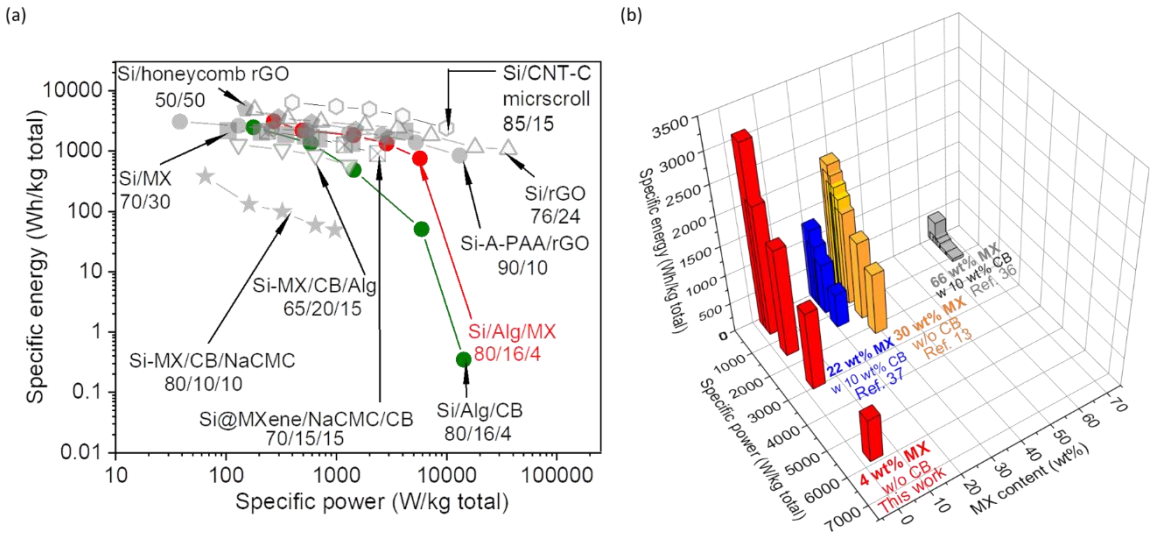


Figure IV-12. (a) Ragone plot of specific energy vs. specific power (W/kg). (b) 3D plot with specific energy, specific power (both based on total electrode mass), and MXene content (wt%).

Next, we compared our results to other reports that used MXenes in the silicon anode.[13, 36, 37, 59] Within those, our electrodes - containing only 4 wt% MXene nanosheets - demonstrated the highest specific energies for the corresponding specific power on a total electrode mass basis. This is more clearly demonstrated in Figure IV-12b, which displays a 3-D plot of specific energy, specific power (both normalized by total electrode mass), and MXene content. The next-best-performing composition was 70 wt% silicon and 30 wt% MXenes, where no polymeric binder was required.[13] In contrast we required 16 wt% Alg binder because such a low MXene concentration (here, 4 wt%) was insufficient to act as a binder alone. Despite adding an insulating binder, our silicon electrodes exhibited superior results because of the high silicon content (80 wt%). Specifically, the Si/Alg/MX=80/16/4 anode yielded the highest specific energy on a *total* electrode mass basis (3100 $Wh/kg_{total}$) as comapred to other silicon-MXene constructs

(~115-2000 $Wh/kg_{total}$) at a corresponding specific power (~270 $W/kg_{total}$). Even lower specific energies were obtained by Zhu *et al.*[37] (22 wt% MXene) and Kong *et al.*[36] (66 wt% MXene) because those electrodes used only 44 wt% and 13 wt% silicon, respectively. These two reports also used hydrophobic carbon additives. From this comparison, we conclude that the large amounts of additives (>30 wt% MXenes, polymer, and/or carbon additive) lowered the active silicon content, which in turn reduced the total electrode's specific energy.

**Conclusions**

Here, we maximized silicon anode capacity by minimizing the amount of two-dimensional $Ti_3C_2T_x$ MXene nanosheet conductive additive. This was accomplished by replacing hydrophobic carbon additives with hydrophilic MXene additives, which facilitated water-based processing. We designed electrodes with a high silicon content of 80 wt%, 16 wt% Alg binder and 4 wt% MXene nanosheets. These electrodes demonstrated stable capacities around 900 $mAh/g_{Si}$ (720 $mAh/g_{total}$) at a high C-rate of 0.5 C, which was higher than a comparable electrode made in-house containing 4 wt% carbon black. Despite having such a low MXene content (4 wt%), our electrodes exhibited specific energies comparable to electrode containing higher amounts of rGO or CNTs.[39, 60-62]The improved electrode performance is attributed to the enhanced conductivity owing to the large lateral MXene nanosheet size. The hydrophilic terminal groups on the MXene nanosheets allowed for slurry casting of homogeneous electrodes using water as the solvent, thus forming uniform electrical networks. Also, the possible hydrogen bonding interactions between hydroxyl groups of MXenes, Alg binder and silicon improved the overall

electrode integrity. Thus, we show that the carbon additives can be eliminated and instead much lower content of MXenes can be used to create homogenous silicon electrodes. These electrodes showed high specific energies without compromising on the electrode integrity for 200 charge-discharge cycles. Our future work will be to further reduce the dead weight of the silicon electrode by utilizing different MXenes or by further lowering the binder content.

**References**


1. Li, J.-Y.; Xu, Q.; Li, G.; Yin, Y.-X.; Wan, L.-J.; Guo, Y.-G., Research Progress Regarding Si-Based Anode Materials Towards Practical Application in High Energy Density Li-Ion Batteries. *Mater. Chem. Front.* **2017,** *1* (9), 1691-1708.
2. Li, M.; Lu, J.; Chen, Z.; Amine, K., 30 Years of Lithium-Ion Batteries. *Adv. Mater.* **2018,** *30* (33), 1-24.
3. Zuo, X.; Zhu, J.; Müller-Buschbaum, P.; Cheng, Y.-J., Silicon Based Lithium-Ion Battery Anodes: A Chronicle Perspective Review. *Nano Energy* **2017,** *31*, 113-143.
4. Salah, M.; Murphy, P.; Hall, C.; Francis, C.; Kerr, R.; Fabretto, M., Pure Silicon Thin-Film Anodes for Lithium-Ion Batteries: A Review. *J. Power Sources* **2019,** *414*, 48-67.
5. Ma, D.; Cao, Z.; Hu, A., Si-Based Anode Materials for Li-Ion Batteries: A Mini Review. *Nano-Micro Lett.* **2014,** *6* (4), 347-358.
6. Franco Gonzalez, A.; Yang, N.-H.; Liu, R.-S., Silicon Anode Design for Lithium-Ion Batteries: Progress and Perspectives. *J. Phys. Chem. C* **2017,** *121* (50), 27775-27787.
7. Obrovac, M. N.; Chevrier, V. L., Alloy Negative Electrodes for Li-Ion Batteries. *Chem. Rev.* **2014,** *114* (23), 11444-502.
8. Iwamura, S.; Nishihara, H.; Ono, Y.; Morito, H.; Yamane, H.; Nara, H.; Osaka, T.; Kyotani, T., Li-rich Li-Si Alloy as a Lithium-Containing Negative Electrode Material Towards High Energy Lithium-Ion Batteries. *Sci. Rep.* **2015,** *5*, 8085.
9. Liu, D.; Liu, Z. J.; Li, X.; Xie, W.; Wang, Q.; Liu, Q.; Fu, Y.; He, D., Group IVA Element (Si, Ge, Sn)-Based Alloying/Dealloying Anodes as Negative Electrodes for Full-Cell Lithium-Ion Batteries. *Small* **2017,** *13* (45), 1702000.
10. Liu, X. H.; Zhong, L.; Huang, S.; Mao, S. X.; Zhu, T.; Huang, J. Y., Size-Dependent Fracture of Silicon Nanoparticles During Lithiation. *ACS Nano* **2012,** *6* (2), 1522-1531.
11. Wang, A.; Kadam, S.; Li, H.; Shi, S.; Qi, Y., Review on Modeling of the Anode Solid Electrolyte Interphase (SEI) for Lithium-Ion Batteries. *npj Comput. Mater.* **2018,** *4*, 15.

12. Peled, E.; Menkin, S., Review—SEI: Past, Present and Future. *J. Electrochem. Soc.* **2017,** *164* (7), A1703-A1719.
13. Zhang, C.; Park, S.-H.; Seral-Ascaso, A.; Barwich, S.; McEvoy, N.; Boland, C. S.; Coleman, J. N.; Gogotsi, Y.; Nicolosi, V., High Capacity Silicon Anodes Enabled by MXene Viscous Aqueous Ink. *Nat. Commun.* **2019,** *10* (1), 849
14. Higgins, T. M.; Park, S. H.; King, P. J.; Zhang, C. J.; McEvoy, N.; Berner, N. C.; Daly, D.; Shmeliov, A.; Khan, U.; Duesberg, G.; Nicolosi, V.; Coleman, J. N., A Commercial Conducting Polymer as Both Binder and Conductive Additive for Silicon Nanoparticle-Based Lithium-Ion Battery Negative Electrodes. *ACS Nano* **2016,** *10* (3), 3702-13.
15. Kwon, T. W.; Choi, J. W.; Coskun, A., The Emerging Era of Supramolecular Polymeric Binders in Silicon Anodes. *Chem. Soc. Rev.* **2018,** *47* (6), 2145-2164.
16. Eshetu, G. G.; Figgemeier, E., Confronting the Challenges of Next-Generation Silicon Anode-Based Lithium-Ion Batteries: Role of Designer Electrolyte Additives and Polymeric Binders. *ChemSusChem* **2019,** *12* (12), 2515-2539.
17. Magasinski, A.; Zdyrko, B.; Kovalenko, I.; Hertzberg, B.; Burtovyy, R.; Huebner, C. F.; Fuller, T. F.; Luzinov, I.; Yushin, G., Toward Efficient Binders for Li-Ion Battery Si-Based Anodes: Polyacrylic Acid. *ACS Appl. Mater. Interfaces* **2010,** *2* (11), 3004-10.
18. Porcher, W.; Chazelle, S.; Boulineau, A.; Mariage, N.; Alper, J. P.; Van Rompaey, T.; Bridel, J. S.; Haon, C., Understanding Polyacrylic Acid and Lithium Polyacrylate Binder Behavior in Silicon Based Electrodes for Li-Ion Batteries. *J. Electrochem. Soc.* **2017,** *164* (14), A3633-A3640.
19. Nguyen, C. C.; Yoon, T.; Seo, D. M.; Guduru, P.; Lucht, B. L., Systematic Investigation of Binders for Silicon Anodes: Interactions of Binder with Silicon Particles and Electrolytes and Effects of Binders on Solid Electrolyte Interphase Formation. *ACS Appl. Mater. Interfaces* **2016,** *8* (19), 12211-20.
20. Kovalenko, I.; Zdyrko, B.; Magasinski, A.; Hertzberg, B.; Milicev, Z.; Burtovyy, R.; Luzinov, I.; Yushin, G., A Major Constituent of Brown Algae for Use in Silicon Anodes. *Science* **2011,** *7* (6052), 75-79.
21. Bie, Y.; Yang, J.; Liu, X.; Wang, J.; Nuli, Y.; Lu, W., Polydopamine Wrapping Silicon Cross-linked with Polyacrylic Acid as High-Performance Anode for Lithium-Ion Batteries. *ACS Appl. Mater. Interfaces* **2016,** *8* (5), 2899-904.
22. Ho, D. N.; Yildiz, O.; Bradford, P.; Zhu, Y.; Fedkiw, P. S., A Silicon-Impregnated Carbon Nanotube Mat as a Lithium-Ion Cell Anode. *J. Appl. Electrochem.* **2017,** *48* (1), 127-133.
23. Luo, J.; Zhao, X.; Wu, J.; Jang, H. D.; Kung, H. H.; Huang, J., Crumpled Graphene-Encapsulated Si Nanoparticles for Lithium Ion Battery Anodes. *J. Phys. Chem. Lett.* **2012,** *3* (13), 1824-9.
24. Lee, J. K.; Smith, K. B.; Hayner, C. M.; Kung, H. H., Silicon Nanoparticles-Graphene Paper Composites for Li Ion Battery Anodes. *Chem. Commun. (Camb)* **2010,** *46* (12), 2025-7.
25. Tang, H.; Zhang, J.; Zhang, Y. J.; Xiong, Q. Q.; Tong, Y. Y.; Li, Y.; Wang, X. L.; Gu, C. D.; Tu, J. P., Porous Reduced Graphene Oxide Sheet Wrapped Silicon

Composite Fabricated by Steam Etching for Lithium-Ion Battery Application. *J. Power Sources* **2015,** *286*, 431-437.
26. Cui, L.-F.; Hu, L.; Choi, J. W.; Cui, Y., Light-Weight Free-Standing Carbon Nanotube-Silicon Films for Anodes of Lithium Ion Batteries. *ACS Nano* **2010,** *4* (7), 3671-3678.
27. Li, W.; Li, M.; Shi, J. A.; Zhong, X.; Gu, L.; Yu, Y., Carbon Nanofiber Interlayer: A Highly Effective Strategy to Stabilize Silicon Anodes for Use in Lithium-Ion Batteries. *Nanoscale* **2018,** *10* (26), 12430-12435.
28. Naguib, M.; Mochalin, V. N.; Barsoum, M. W.; Gogotsi, Y., 25th Anniversary Article: MXenes: A New Family of Two-Dimensional Materials. *Adv. Mater.* **2014,** *26* (7), 992-1005.
29. Verger, L.; Natu, V.; Carey, M.; Barsoum, M. W., MXenes: An Introduction of Their Synthesis, Select Properties, and Applications. *Trends Chem.* **2019,** *1* (7), 656-669.
30. Zhang, X.; Zhang, Z.; Zhou, Z., MXene-Based Materials for Electrochemical Energy Storage. *J. Energy Chem.* **2018,** *27* (1), 73-85.
31. Sun, S.; Liao, C.; Hafez, A. M.; Zhu, H.; Wu, S., Two-Dimensional MXenes for Energy Storage. *Chem. Eng. J.* **2018,** *338*, 27-45.
32. Kim, S. J.; Naguib, M.; Zhao, M.; Zhang, C.; Jung, H.-T.; Barsoum, M. W.; Gogotsi, Y., High Mass Loading, Binder-Free MXene Anodes for High Areal Capacity Li-Ion Batteries. *Electrochim. Acta* **2015,** *163*, 246-251.
33. Ling, Z.; Ren, C. E.; Zhao, M. Q.; Yang, J.; Giammarco, J. M.; Qiu, J.; Barsoum, M. W.; Gogotsi, Y., Flexible and Conductive MXene Films and Nanocomposites with High Capacitance. *Proc. Natl. Acad. Sci. U. S. A., Early Ed.* **2014,** *111* (47), 16676-81.
34. Sobolciak, P.; Ali, A.; Hassan, M. K.; Helal, M. I.; Tanvir, A.; Popelka, A.; Al-Maadeed, M. A.; Krupa, I.; Mahmoud, K. A., 2D $Ti_3C_2T_x$ (MXene)-Reinforced Polyvinyl Alcohol (PVA) Nanofibers with Enhanced Mechanical and Electrical Properties. *PLoS One* **2017,** *12* (8), e0183705.
35. Naguib, M.; Saito, T.; Lai, S.; Rager, M. S.; Aytug, T.; Parans Paranthaman, M.; Zhao, M.-Q.; Gogotsi, Y., $Ti_3C_2T_x$(MXene)–Polyacrylamide Nanocomposite Films. *RSC Adv.* **2016,** *6* (76), 72069-72073.
36. Kong, F.; He, X.; Liu, Q.; Qi, X.; Sun, D.; Zheng, Y.; Wang, R.; Bai, Y., Enhanced Reversible Li-ion Storage in Si@$Ti_3C_2$ MXene Nanocomposite. *Electrochem. Commun.* **2018,** *97*, 16-21.
37. Zhu, X.; Shen, J.; Chen, X.; Li, Y.; Peng, W.; Zhang, G.; Zhang, F.; Fan, X., Enhanced Cycling Performance of Si-MXene Nanohybrids as Anode for High Performance Lithium Ion Batteries. *Chem. Eng. J.* **2019,** *378*, 122212.
38. Zeng, W.; Wang, L.; Peng, X.; Liu, T.; Jiang, Y.; Qin, F.; Hu, L.; Chu, P. K.; Huo, K.; Zhou, Y., Enhanced Ion Conductivity in Conducting Polymer Binder for High-Performance Silicon Anodes in Advanced Lithium-Ion Batteries. *Adv. Energy Mater.* **2018,** *8* (11), 1702314.
39. Wang, H.; Fu, J.; Wang, C.; Wang, J.; Yang, A.; Li, C.; Sun, Q.; Cui, Y.; Li, H., A Binder-Free High Silicon Content Flexible Anode for Li-Ion Batteries. *Energy Environ. Sci.* **2020,** *13* (3), 848-858.

40. Wang, L.; Liu, T.; Peng, X.; Zeng, W.; Jin, Z.; Tian, W.; Gao, B.; Zhou, Y.; Chu, P. K.; Huo, K., Highly Stretchable Conductive Glue for High-Performance Silicon Anodes in Advanced Lithium-Ion Batteries. *Adv. Func. Mater.* **2018,** *28* (3), 1704858-66.
41. Dufficy, M. K.; Khan, S. A.; Fedkiw, P. S., Galactomannan Binding Agents for Silicon Anodes in Li-Ion Batteries. *J. Mater. Chem. A* **2015,** *3* (22), 12023-12030.
42. Alhabeb, M.; Maleski, K.; Anasori, B.; Lelyukh, P.; Clark, L.; Sin, S.; Gogotsi, Y., Guidelines for Synthesis and Processing of Two-Dimensional Titanium Carbide ($Ti_3C_2T_x$ MXene). *Chem. Mater.* **2017,** *29* (18), 7633-7644.
43. Fenoradosoa, T. A.; Ali, G.; Delattre, C.; Laroche, C.; Petit, E.; Wadouachi, A.; Michaud, P., Extraction and Characterization of an Alginate from the Brown Seaweed Sargassum Turbinarioides Grunow. *J. Appl. Phycol.* **2009,** *22* (2), 131-137.
44. Xu, S.; Wei, G.; Li, J.; Ji, Y.; Klyui, N.; Izotov, V.; Han, W., Binder-Free $Ti_3C_2T_x$ MXene Electrode Film for Supercapacitor Produced by Electrophoretic Deposition Method. *Chem. Eng. J.* **2017,** *317*, 1026-1036.
45. Wang, L.; Chen, L.; Song, P.; Liang, C.; Lu, Y.; Qiu, H.; Zhang, Y.; Kong, J.; Gu, J., Fabrication on the Annealed $Ti_3C_2T_x$ MXene/Epoxy Nanocomposites for Electromagnetic Interference Shielding Application. *Composites, Part B* **2019,** *171*, 111-118.
46. Wu, X.; Hao, L.; Zhang, J.; Zhang, X.; Wang, J.; Liu, J., Polymer-$Ti_3C_2T_x$ Composite Membranes to Overcome the Trade-Off in Solvent Resistant Nanofiltration for Alcohol-Based System. *J. Membr. Sci.* **2016,** *515*, 175-188.
47. Jerliu, B.; Huger, E.; Dorrer, L.; Seidlhofer, B. K.; Steitz, R.; Horisberger, M.; Schmidt, H., Lithium Insertion into Silicon Electrodes Studied by Cyclic Voltammetry and Operando Neutron Reflectometry. *Phys. Chem. Chem. Phys.* **2018,** *20* (36), 23480-23491.
48. Jun, B.-M.; Kim, S.; Heo, J.; Park, C. M.; Her, N.; Jang, M.; Huang, Y.; Han, J.; Yoon, Y., Review of MXenes as New Nanomaterials for Energy Storage/Delivery and Selected Environmental Applications. *Nano Research* **2018,** *12* (3), 471-487.
49. Lia, J.; Dahn, J. R., An In Situ X-Ray Diffraction Study of the Reaction of Li with Crystalline Si. *J. Electrochem. Soc.* **2007,** *154* (3), A156-A161.
50. Wu, H.; Yu, G.; Pan, L.; Liu, N.; McDowell, M. T.; Bao, Z.; Cui, Y., Stable Li-Ion Battery Anodes by In-Situ Polymerization of Conducting Hydrogel to Conformally Coat Silicon Nanoparticles. *Nat. Commun.* **2013,** *4*, 1943.
51. Feng, K.; Li, M.; Liu, W.; Kashkooli, A. G.; Xiao, X.; Cai, M.; Chen, Z., Silicon-Based Anodes for Lithium-Ion Batteries: From Fundamentals to Practical Applications. *Small* **2018,** *14* (8), 1702737.
52. Zhang, C.; Ma, Y.; Zhang, X.; Abdolhosseinzadeh, S.; Sheng, H.; Lan, W.; Pakdel, A.; Heier, J.; Nüesch, F., Two-Dimensional Transition Metal Carbides and Nitrides (MXenes): Synthesis, Properties, and Electrochemical Energy Storage Applications. *Energy Environ. Mater.* **2020,** *3* (1), 29-55.

53. Sánchez-González, J.; Macías-García, A.; Alexandre-Franco, M. F.; Gómez-Serrano, V., Electrical Conductivity of Carbon Blacks Under Compression. *Carbon* **2005,** *43* (4), 741-747.
54. Zhao, Y.; Yang, L.; Zuo, Y.; Song, Z.; Liu, F.; Li, K.; Pan, F., Conductive Binder for Si Anode with Boosted Charge Transfer Capability via n-Type Doping. *ACS Appl. Mater. Interfaces* **2018,** *10* (33), 27795-27800.
55. Xie, J.; Imanishi, N.; Zhang, T.; Hirano, A.; Takeda, Y.; Yamamoto, O., Li-Ion Diffusion in Amorphous Si Films Prepared by RF Magnetron Sputtering: A Comparison of Using Liquid and Polymer Electrolytes. *Mater. Chem. Phys.* **2010,** *120* (2-3), 421-425.
56. Sarang, K. T.; Li, X.; Miranda, A.; Terlier, T.; Oh, E.-S.; Verduzco, R.; Lutkenhaus, J. L., Tannic Acid as a Small-Molecule Binder for Silicon Anodes. *ACS Appl. Energy Mater.* **2020,** *3* (7), 6985-6994.
57. Sarang, K. T.; Zhao, X.; Holta, D.; Radovic, M.; Green, M. J.; Oh, E. S.; Lutkenhaus, J. L., Minimizing Two-Dimensional $Ti_3C_2T_x$ MXene Nanosheet Loading in Carbon-Free Silicon Anodes. *Nanoscale* **2020,** *12* (40), 20699-20709.
58. Luo, W.; Chen, X.; Xia, Y.; Chen, M.; Wang, L.; Wang, Q.; Li, W.; Yang, J., Surface and Interface Engineering of Silicon-Based Anode Materials for Lithium-Ion Batteries. *Adv. Energy Mater.* **2017,** *7* (24), 1701083.
59. Tian, Y.; An, Y.; Feng, J., Flexible and Freestanding Silicon/MXene Composite Papers for High-Performance Lithium-Ion Batteries. *ACS Appl. Mater. Interfaces* **2019,** *11* (10), 10004-10011.
60. Tang, H.; Tu, J.-p.; Liu, X.-y.; Zhang, Y.-j.; Huang, S.; Li, W.-z.; Wang, X.-l.; Gu, C.-d., Self-Assembly of Si/Honeycomb Reduced Graphene Oxide Composite Film as a Binder-free and Flexible Anode for Li-Ion Batteries. *J. Mater. Chem. A* **2014,** *2* (16), 5834-5840.
61. Assresahegn, B. D.; Ossonon, B. D.; Bélanger, D., Graphene Nanosheets and Polyacrylic Acid Grafted Silicon Composite Anode for Lithium Ion Batteries. *J. Power Sources* **2018,** *391*, 41-50.
62. Chang, J.; Huang, X.; Zhou, G.; Cui, S.; Hallac, P. B.; Jiang, J.; Hurley, P. T.; Chen, J., Multilayered Si Nanoparticle/Reduced Graphene Oxide Hybrid as a High-Performance Lithium-Ion Battery Anode. *Adv. Mater.* **2014,** *26* (5), 758-64.
63. Yan, Y.; Zhao, X.; Dou, H.; Wei, J.; Sun, Z.; He, Y. S.; Dong, Q.; Xu, H.; Yang, X., MXene Frameworks Promote the Growth and Stability of LiF-Rich Solid-Electrolyte Interphases on Silicon Nanoparticle Bundles. *ACS Appl. Mater. Interfaces* **2020,** *12* (16), 18541-18550.

# CHAPTER V

# CRUMPLED $Ti_3C_2T_X$ MXENE ENCAPSULATED SILICON PARTICLES

## Introduction

The development of high energy density lithium-ion batteries is required to address the critical needs of applications like next generation electronics and electric vehicles.[1] Through careful engineering, energy density of lithium-ion batteries has gradually increased; but the current lithium-graphite ($LiC_6$) intercalation chemistries are approaching capacity limits.[2] To further increase the energy density, other high capacity anode materials with alloying chemistries are being researched.[3] Amongst those, silicon is regarded an ideal anode because of its superior theoretical specific capacity of 3579 mAh/g ($Li_{15}Si_4$), low working potential (~0.5 V *vs.* $Li/Li^+$) and abundance in nature.[4]

Despite these advantages, silicon has not yet dominated the market because of two major issues. First, silicon particles undergo >300% volumetric expansion on full lithium insertion (lithiation), and contracts significantly on lithium extraction (delithiation).[5] This causes pulverization and loss of contact with active materials and electrode framework. Secondly, due to low electrochemical potential, solid electrolyte interphase (SEI) layer deposits on anode due to reductive decomposition of electrolyte.[6] Usually, a thin SEI layer formed during the first cycle prevents further electrolyte decomposition by passivating the surface. However, in case of silicon anodes, the SEI layer breaks due to huge volume changes which exposes new surfaces to electrolyte causing continuous SEI buildup on anode surface.[7] The excessive growth of SEI increases cell resistance, lowers Coulombic efficiency, and consumes electrolyte which eventually causes battery failure.[7]

Pioneering studies have shown that the pulverization problem caused by the large volume expansion can be minimized when the silicon particles are smaller than a critical size (<150 nm)[8] and the electrode is well-constructed with interior void space or pre-formed porosity to buffer the volume change.[9] Based on these findings, several approaches have been reported in literature which are utilizing nanowires,[10] nanotubes,[11] core-shell structures,[9] and porous structures.[12] Specifically, in the core-shell structure, the active material is encapsulated within a conducting carbon layer, with some empty space provided between the carbon layer and the active material to buffer the volume changes during lithiation. Similar to core-shell structures, Luo *et al.* first showed evidence of a crumpled paper morphology where they reported crumpling graphene sheets around silicon nanoparticles.[13] However, graphene or other conductive carbon have poor interaction with silicon owing to lack of hydrogen bonding groups.

MXene, a new category of two-dimensional (2D) materials first reported in 2011 by Gogotsi and co-workers, has attracted more attention in the field of energy storage because of their unprecedented combinations of properties such as excellent electronic conductivity and compositional adaptability.[14, 15] Titanium carbide ($Ti_3C_2T_x$) is one of the MXene material, which has a structure similar to graphene, but provides faster $Li^+$ transport ($\approx 10^{-10}$–$10^{-9}$ $cm^2/s$) due to lower lithium diffusion barrier of $Ti_3C_2$ (0.07 eV) than that of graphene (0.3 eV).[16, 17] Additionally, the surface of MXene has abundant hydrogen bonding groups (-OH, -O) which can probably improve interaction with silicon active material.

Several Si/MXene composites have been reported previously wherein silicon particles are sandwiched between MXene nanosheets via physical blending,[18-21] vacuum filtration,[22] electrostatic interactions,[23] and in-situ magnesiothermic/aluminothermic reductions from MXene nanosheets/$SiO_2$ composites.[24, 25] Recently, core-shell structure using MXene nanosheets and silicon particles were also reported.[26, 27] Xia *et al*. made the core-shell structures by wrapping MXene nanosheets on porous silicon nanospheres coated with a sacrificial poly(methylmethacrylate) layer.[26] The electrodes demonstrated a long-term cycling capacity of ~500 mAh/g (350 mAh/$g_{total}$) at 2000$^{th}$ cycle at ~0.2 C. These core-shell structures were synthesized using large number of steps involving harsh chemical and temperature conditions. On the other hand, Yan *et al.* made a core-shell structures of MXenes around silicon nanoparticles via spray dryer.[27] The electrodes showed capacities of 400 mAh/$g_{total}$ at 500$^{th}$ cycle at ~0.5 C. Both these studies utilized 30 wt% of binders and carbon additives, thus reducing the total electrode capacity.

Previous reports on core-shell structures for lithium-ion batteries have also reported addition of large amount of binders during electrode processing so as to construct a continuous, conductive network and to disperse and fix these particles.[28] This reduces the silicon content in the entire electrode which overall reduces the total electrode capacity. Except the recent paper reported by Wang *et al.* where they have achieved 85 wt% of Si loading in the entire electrode[28], rest of the papers still report low silicon loading in the range of 22-45 wt%.

Here, we designed a core-shell architecture by crumpling MXenes around silicon particles using a simple one-step spray drying process. These crumpled particles were

blended with poly(vinylidene fluoride) (PVDF) to fabricate electrodes with the aim to minimize the dead weight in the electrode. We determined the optimum content of MXenes and silicon particles to maximize the cycling capacity, which was 68 wt% silicon and 32 wt% MXenes. To evaluate the battery performance, we performed galvanostatic cycling to determine electrode's capacity and stability at higher C-rates and over large number of cycles. We performed electrochemical impedance spectroscopy to determine the electrode's impedance, and cyclic voltammetry at different scan rates to deconvolute charge-storage mechanism. We utilized scanning electron microscopy, along with energy dispersive X-ray spectroscopy to observe the morphologies and elemental distribution, respectively. We also utilized X-ray photoelectron spectroscopy to evaluate the SEI formed on the electrode after cycling. Additionally, we directly compared the crumpled electrode's performance with the uncrumpled electrode correlate the observed performance to electrode architecture.

**Materials**

Silicon nanoparticles (98+% purity, 50-70 nm size, 80-120 $m^2/g$ surface area) were purchased from US-research nanomaterials. Poly(vinylidene fluoride) powder (Solef 5130) was purchased from Solvay. 1 M lithium hexafluorophosphate ($LiPF_6$) in ethylene carbonate (EC):diethyl carbonate (DEC) (1:1 v/v), hydrochloric acid (HCl, ACS reagent 37 % w/w), dimethyl sulfoxide (DMSO, ReagentPlus, >99.5 %), sodium ascorbate (>99% assay), and 1-methyl-2-pyrrolidinone (ACS reagent, >99% purity) were purchased from Sigma Aldrich. Lithium foil (0.75 mm thick x 19 mm wide), lithium fluoride (LiF, 98+ % purity), fluoroethylene carbonate (FEC), titanium (Ti, 44 µm average particle size, 99.5

% purity), aluminum (Al, 44 µm average particle size, 99.5 % purity), and titanium carbide (TiC) (2-3 µm average particle size, 99.5 % purity) were purchased from Alfa Aesar. Super P carbon black (CB) (0.04 µm particle size, 62 $m^2/g$ surface area), copper foil (length x width x thickness = 170 m x 280 mm x 9 um) were purchased from MTI corporation. Polypropylene separator (19 mm diameter x 0.025 mm thick) was purchased from Celgard.

**Methods**

***Preparation of $Ti_3C_2T_x$ MXenes crumpled around silicon nanoparticles***

$Ti_3C_2T_x$ MXene nanosheets were synthesized following a procedure available in literature[29] and also detailed in the Chapter I. The as-synthesized MXene nanosheet colloidal solution was treated with equal molar amount of sodium ascorbate (NaASc) (for *e.g.* to 1 M colloidal solution of MXene nanosheets, 1 M NaASc was added) to minimize its oxidation and improve its stability in water.[30] Three different dispersions were prepared: MX=1 mg/ml + Si=0.6 mg/ml, MX=1 mg/ml + Si=0.4 mg/ml, and MX=0.4 mg/ml + Si=1 mg/ml. These dispersions were bath sonicated for 10 min followed by vortex mixing for 2 min to ensure formation of a uniform and stable dispersion. These dispersions were passed through a spray dryer (Buchi B-290 mini spray dryer) to generate the crumpled product (Figure V-1). For the spray drying process, a pump flow rate of 10 % (of maximum possible flow rate), atomizer air pressure of 60 psi, and inlet temperature of 200 °C was used. The dispersion was atomized to form micrometer-sized droplets which were then mixed with in-house air that flowed through a vertical path and the product was collected in a vessel after the cyclone separator. During spray drying, the

dispersions were stirred at 50 rpm to minimize settling of silicon nanoparticles. The as-synthesized crumpled product was stored under vacuum at room temperature until further use.

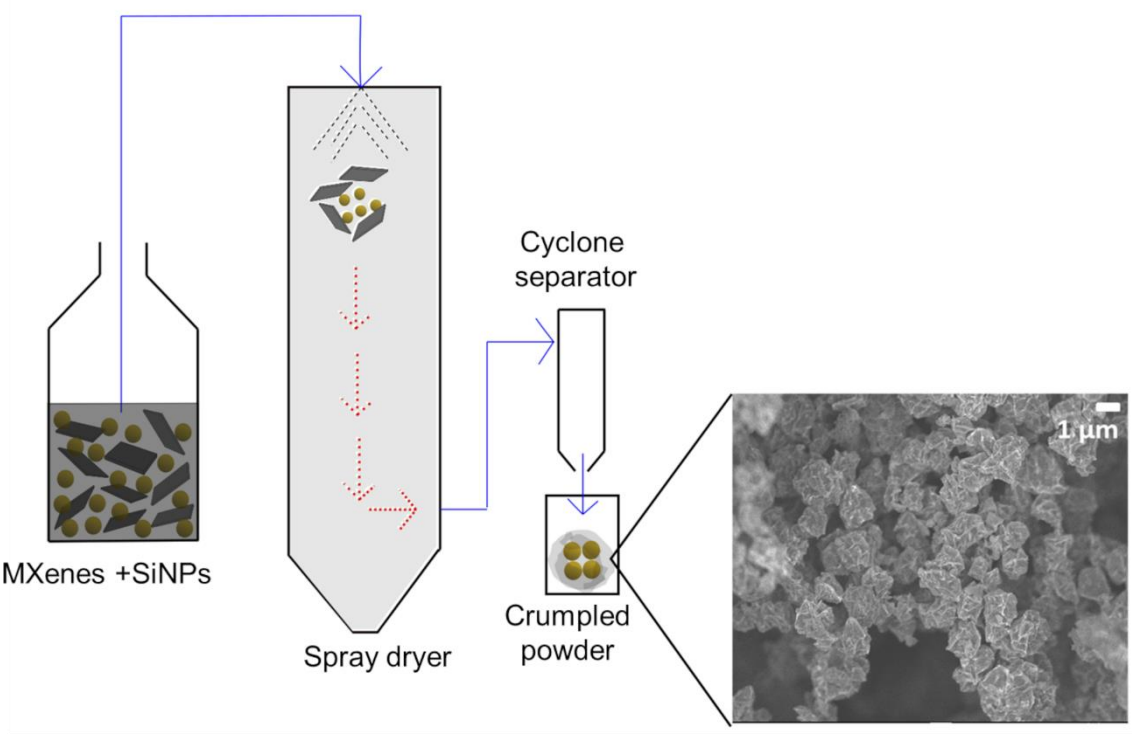


Figure V-1. Schematic of spray dryer assembly used to crumple MXene nanosheets around silicon nanoparticles and a SEM image of the crumpled product. A mixture of MXene nanosheets and silicon nanoparticles is spray dried to obtain crumpled product at the end of cyclone separator.

***Scanning electron microscopy (SEM) and energy dispersive X-ray spectroscopy (EDS)***

The morphologies of the crumpled product and fabricated electrodes were characterized using SEM (JEOL JSM SEM) together with EDS. For SEM, an accelerating voltage of 5 kV and a working distance of 15 mm was applied. For EDS, an was applied. The EDS data was analyzed using the INCA software. Prior to characterization, the

samples were coated with platinum (3 nm) using a sputter coater (208 HR by Cressington). The size of crumpled particles was determined by analysing SEM using Image J software.

***X-ray photoelectron spectroscopy (XPS)***

XPS was performed (Omicron ESCA Probe, Omicron Nanotechnology) using a monochromated Mg source X-ray beam. XPS survey scans were performed with an analyzer pass energy of 100-1100 eV (1.0 eV steps, 50 ms dwell time). All spectra were calibrated with the C 1s photoemission peak for $sp^2$-hybridized carbon at 284.5 eV and the full width half maximum (FWHM) was constrained. Curve fitting (using CasaXPS software) was conducted using a Gaussian-Lorentzian peak shape after Shirley-type background correction. Spectra for all components were calibrated based on the adventitious carbon peak (C-C, 284.5 eV). Three major constraints were applied for fitting. First, the components of Ti 2p ($2p_{3/2}$ and $2p_{1/2}$) were constrained to an area ratio of 2:1 $2p_{3/2}$:$2p_{1/2}$. Secondly, full width half maximum (FWHM) values were constrained. Lastly, all binding energies (eV) were verified with previous literature results.[30-32]

***Silicon anode preparation***

The working silicon electrode was prepared by casting slurries using a film applicator (Elcometer 4340 Automatic applicator) of crumpled product and PVDF as binder in NMP. No additional carbon black was added. First, a dispersion of 9 wt% PVDF in NMP was made by stirring and heating at 90 °C overnight. The desired amount of PVDF solution was mixed with crumpled product using a mortar and pestle to form uniform slurries. These slurries were then cast onto copper foil and dried at 50 °C overnight, followed by vacuum at room temperature for 3 days. 16 mm electrodes were punched

using a precision disc cutter (MTI). The loading of composite material (*i.e.* MX/Si capsule) ranged from 1-1.5 mg/cm$^2$. Higher loadings of 1.8, 2.2, and 2.8 mg/cm$^2$ were also made.

***Electrochemical characterization***

These silicon working electrodes were used to make half cells in an argon-filled glovebox (MBRaun, Labstar 1200). Lithium metal was used as the counter/reference electrode, 1 M $LiPF_6$ in EC:DEC (1:1 v/v) with 10 wt% FEC was used as the electrolyte, and two 3501 Celgard separator were used.

Galvanostatic charge-discharge (GCD) tests and rate performance tests were performed using battery testing equipment (Arbin Instrument, HPT-100mA) in a voltage window of 0.01 V to 1 V *vs.* $Li/Li^+$. For GCD tests, the cells were cycled at 0.1 C in constant current-constant voltage (CC-CV) mode for the first five cycles, followed by cycling at 0.5 C in CC mode for the remaining 195 cycles. In CV mode, the voltage was held constant at 0.01 V until the current decayed to 0.01 C. For the rate performance tests, the cells were cycled at different C-rates of 0.05 C, 0.1C, 0.2 C, 0.5 C, 1 C, 2 C, and 3 C (at 0.05 C- three cycles, remaining C-rates – five cycles each), all in CC mode. The charge-discharge rates were calculated based on theoretical capacity of silicon (3579 mAh/g). All capacities, unless specified are reported based on the mass of Si/MXene capsule. We also carried long term cycling tests (500 cycles) at a constant C-rate of 0.1 C for selected electrodes. Cyclic voltammetry was performed on Solartron Potentiostat/Galvanostat Instrument (Solartron, Electrochemical Interface 1287) at different scan rates of 0.1, 0.2, 0.3, 0.4, 0.5, 0.7, and 0.9 mV/s (each for three cycles). Electrochemical impedance

spectroscopy (EIS) was performed on Gamry Potentiostat/Galvanostat Instrument (Gamry Instruments, Electrochemical Interface 1000) with 50 mV amplitude and 100 kHz−5 mHz frequency range at a DC potential of 0.2 V *vs.* $Li/Li^+$. Prior to EIS testing, the cell was conditioned at 0.2 V for 2 h.

**Results and discussions**

Spray drying was used to create MXene nanosheets crumpled around silicon nanoparticles, as shown in Figure V-1. Briefly, $Ti_3C_2T_x$ MXene colloidal dispersion was treated with sodium ascorbate[30] to protect the MXene nanosheets from oxidation that might occur during spray drying. To this colloidal dispersion, the desired amount of silicon nanoparticles was added and then spray dried to obtain three sets of crumpled products. The crumpled products were assigned names according to the relative weight percentages of MXene and silicon nanoparticles particles in the dispersions used for spray drying: MX/Si=68/32, MX/Si=50/50, and MX/Si=32/68. SEM and EDS were performed on the crumpled products to observe the morphology and distribution of MXenes and silicon nanoparticles. SEM images confirm the successful crumpling of MXene nanosheets around the silicon nanoparticles. The particle sizes were 1-2.5 μm for all 3 compositions, Figure V-2a. For comparison, our particle sizes and distributions are smaller than a previous report by Yan *et al.* (2-7 μm);[27] we attribute this to our past studies on optimizing the spray drying conditions.[33] EDS confirms the presence of titanium (from MXenes) and silicon, as expected (Figure V-2b).

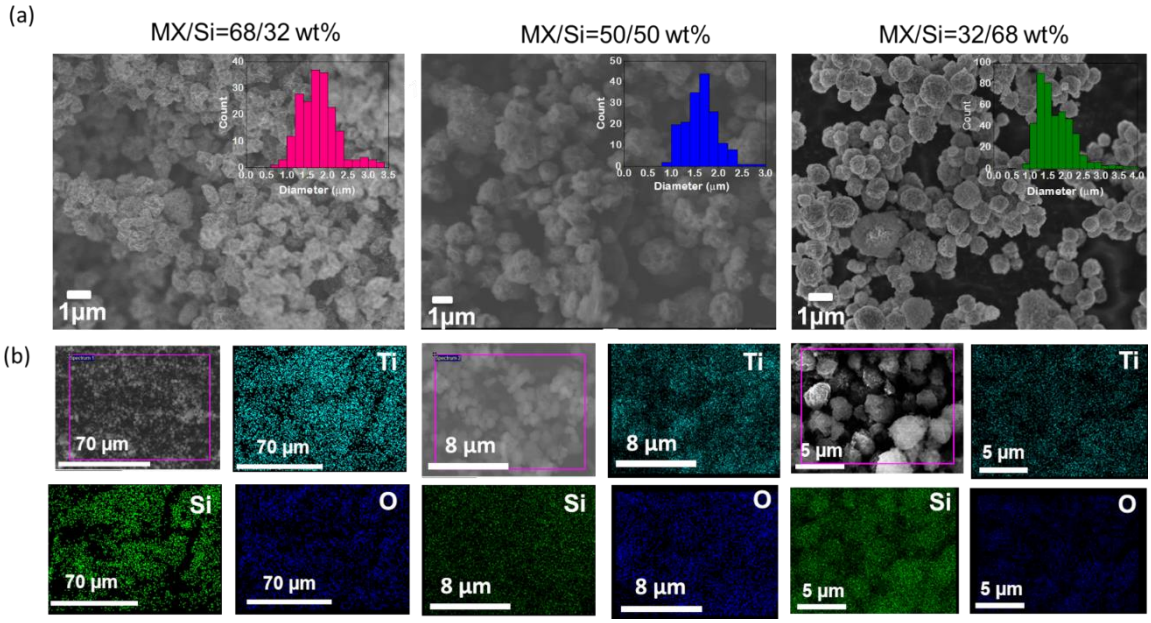


Figure V-2. (a) Scanning electron microscopy (SEM) images of three different sets of spray-dried mixtures; MX/Si=68/32, MX/Si=50/50, and MX/Si=32/68. The values represent the weight% of that component in the dispersion before spray drying. Inset shows histograms of crumpled particle sizes. (c) Energy dispersive X-ray spectroscopy (EDS) of the crumpled particles.

Knowing the average capsule diameter, MXene sheet thickness, and silicon nanoparticle diameter, it is possible to estimate the number of silicon nanoparticles per capsule Assuming perfect spheres of diameters 1.5 μm and 60 nm for the capsule and the silicon nanoparticles, as well as a 63% packing fraction, we estimate an upper bound of ~9800 silicon nanoparticles per capsule. As this represents an upper bound, we expect the actual silicon nanoparticle loading to decrease as the MXene weight fraction increases (and the particle size remains the same).

XPS was also performed on the crumpled products (Figure V-3). The survey scan and the elemental composition for all three crumpled products shows presence of both titanium and Si. The deconvoluted C1s, O1s, F1s, Ti2p, Si 2p for MX/Si=68/32 crumpled

powder is shown in Figure V-4. The deconvoluted C 1s, O 1s, F1s, and Ti 2p spectra shows presence of several peaks attributed to MXene nanosheets.[30, 31] The peaks were deconvoluted following our previous reports.[30] The presence of $TiO_2$ (~460 eV) in the deconvoluted Ti spectra implies that there was some oxidation of MXene nanosheets.[31] The deconvoluted O spectra shows presence of Si-O-Ti peak (~531 eV) which was observed in a previous report as well.[26] The typical Si-O and Si-Si peaks at 102.3 eV and 99.8 eV, respectively, were observed in the deconvoluted Si spectra.

Both EDS and XPS analysis did not show a trend in Si and Ti atomic%. Also, the compositions obtained via both the techniques are very different, which is probably because the technique used to get these compositions in very different. There is also a possibility that because of the thick MXene layer in the crumpled particles, the X-ray or the electrons might not penetrate entirely, giving an error in during composition measurement.

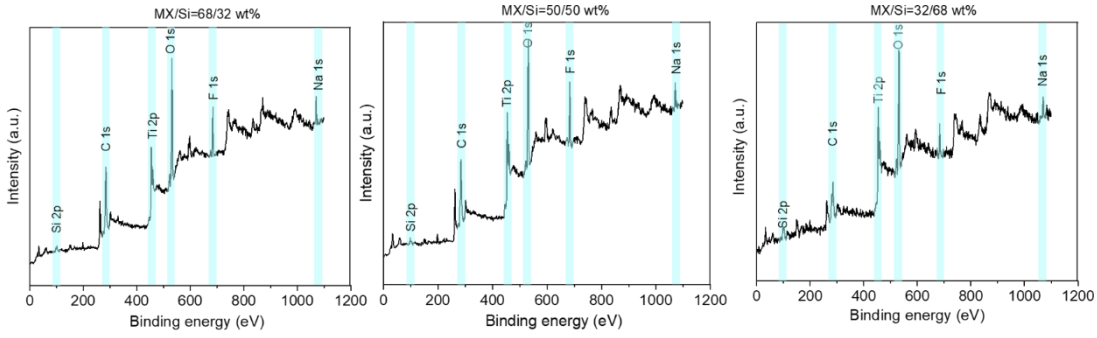


| | MX/Si=68/32 wt% | | | | | | MX/Si=50/50 wt% | | | | | | MX/Si=32/68 wt% | | | | | |
|---|---|---|---|---|---|---|---|---|---|---|---|---|---|---|---|---|---|---|
| Element | Ti | Si | C | O | F | Na | Ti | Si | C | O | F | Na | Ti | Si | C | O | F | Na |
| Atomic% | 14 | 2.23 | 24.6 | 40.8 | 11.8 | 5.53 | 27.8 | 1.41 | 21.9 | 31.6 | 12.1 | 5.15 | 33.1 | 5.08 | 16.0 | 33.8 | 7.58 | 4.39 |

Figure V-3. X-ray photoelectron spectroscopy (XPS) survey scan of crumpled MX/Si=68/32, MX/Si=50/50, and MX/Si=32/68 crumpled product. The table shows the atomic% of elements present in these crumpled product.

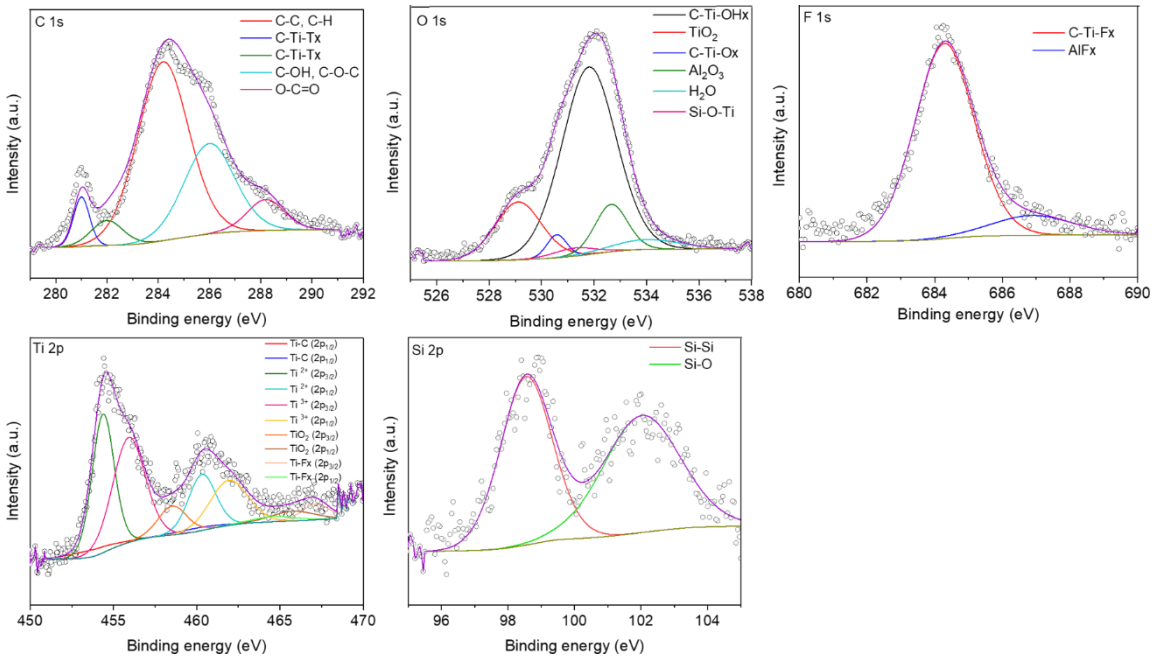


Figure V-4. Deconvoluted C 1s, O 1s, F 1s, Ti 2p, and Si 2p peaks of crumpled MX/Si=68/32 wt% powder.

First, we performed initial screening to determine the minimal amount of PVDF binder required to form a carbon-free, crumpled MXSi anode. The three sets of crumpled products were mixed with varying amounts of PVDF and slurry cast from NMP (organic solvent was used because MXenes uncrumple in the presence of water[31]). In the absence of PVDF, the electrodes crumbled and could not be cycled, so electrodes containing 5, 10, and 20 wt% PVDF were examined. The electrodes were assembled in two-electrode half cells with lithium metal as the counter/reference electrode and 1 M $LiPF_6$ in EC:DEC (1:1

v/v) with 10 wt% FEC as the electrolyte. Galvanostatic charge-discharge (GCD) was performed at 0.1 C in constant current-constant voltage (CC-CV) mode first for five

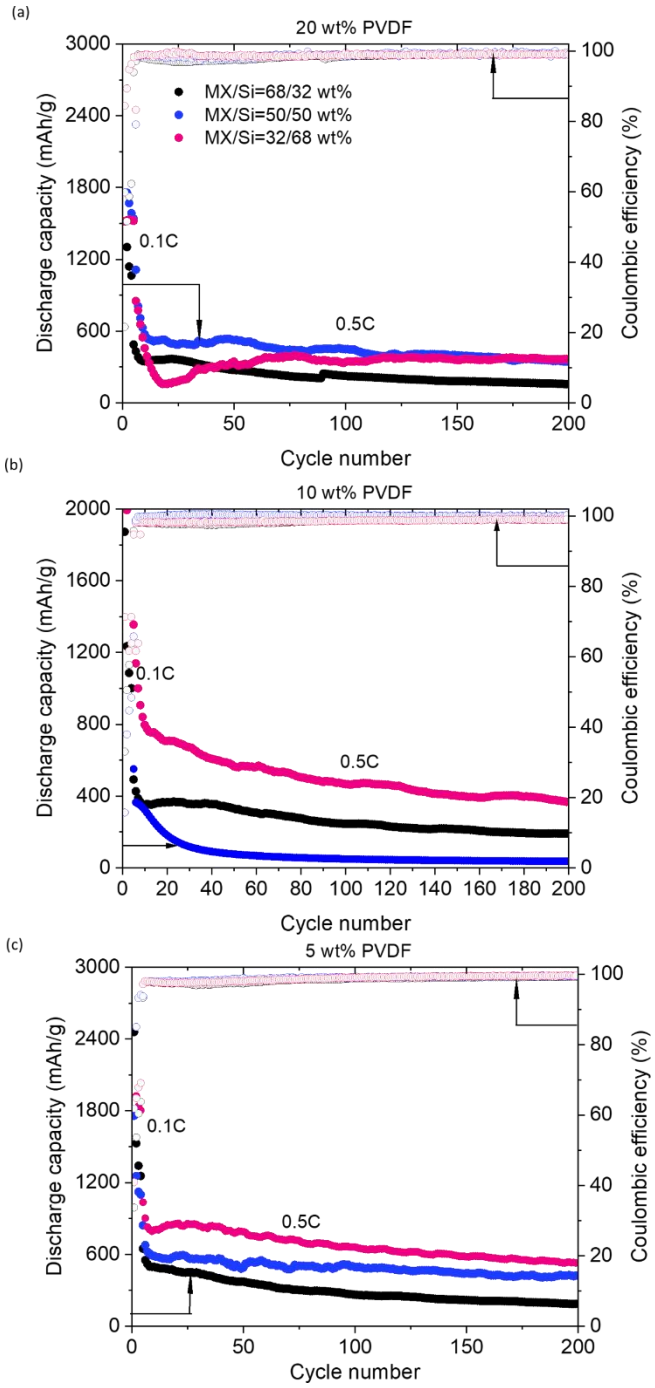


Figure V-5. Galvanostatic charge-discharge of MX/Si=68/32, MX/Si=50/50, and MX/Si=32/68 electrodes with (a) 20 wt%, (b) 10 wt%, and (c) 5 wt% PVDF. The electrodes were made using a simple slurry casting method using NMP as the solvent. No additional Super P CB was added. Galvanostatic charge-discharge was performed at 0.1

C in constant current-constant voltage (CC-CV) mode for first 5 cycles, followed by cycling at 0.5 C in CC mode for remaining 195 cycles.

cycles, followed by cycling at 0.5 C in CC mode for 195 cycles. All capacities, unless specified, are reported based on mass of MX/Si capsule. As the PVDF content in the electrode increased from 5 to 20 wt% (Figure V-5), a drop in discharge capacity was observed due to PVDF's insulating nature. This observation was further confirmed using electrochemical impedance spectroscopy (EIS) on MX/Si=68/32 electrodes containing 5, 10, or 20 wt% PVDF after 100 cycles (Figure V-6). The diameter of depressed semi-circle and thus the resistance was lowest for the electrode containing 5 wt% PVDF; thus we concluded that, 5 wt% PVDF was sufficient to maintain electrode's integrity while minimizing the charge transfer resistance, and all further studies used that PVDF composition.

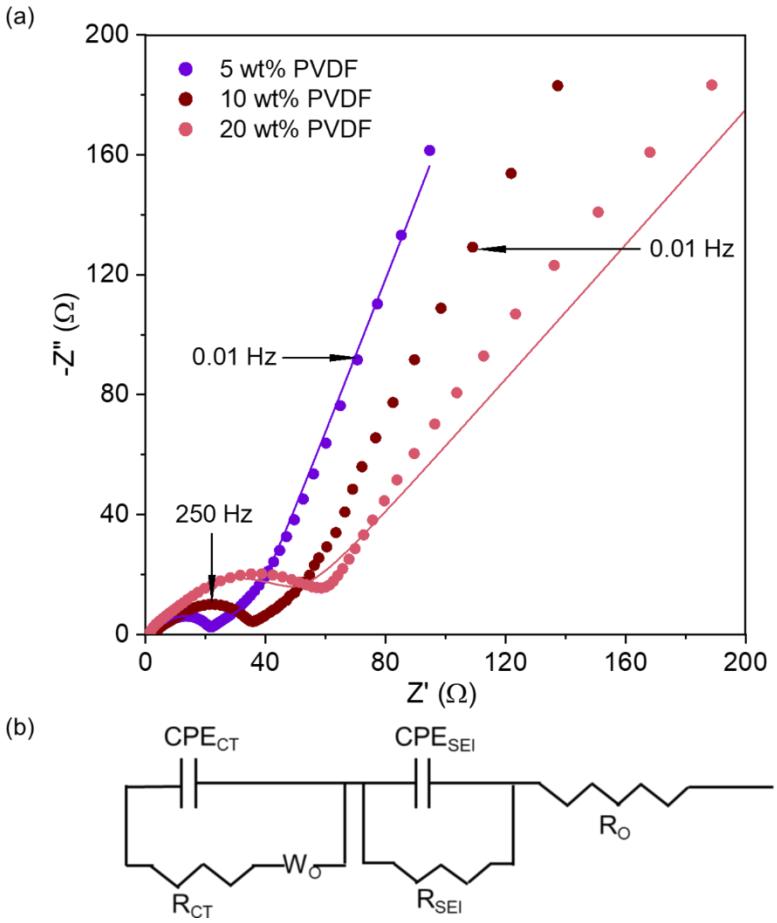


Figure V-6. Nyquist plot for a representative MX/Si=50/50 electrode for PVDF content of 20, 10, and 5 wt% obtained from electrochemical impedance spectroscopy (EIS) performed after 100 cycles of charge-discharge. EIS was performed with a frequency range from 100 kHz to 5 mHz with an amplitude of 10 mV around a potential of 0.2 V. (b) Equivalent circuit model used to fit the EIS data. The points represent the experimental data and solid lines represent the equivalent circuit model to fit to the data.

Figure V-7 presents GCD, EIS, and SEM analysis for MX/Si=68/32, MX/Si=50/50, and MX/Si=32/68 anodes containing 5 wt% PVDF binder. The anodes were cycled as described before with the goal of determining the effect of varying the MXene/Si ratio. Figure V-7a shows the galvanostatic cycling performance of MX/Si=68/32, MX/Si=50/50, and MX/Si=32/68 electrodes, and the corresponding

voltage profiles are shown in Figure V-8. For the first cycle (Figure V-8a), a flat plateau at 0.1 V was present due to the conversion of crystalline silicon (*c*-Si) to lithiated amorphous (*a*-$Li_xSi$). The initial discharge capacities for MX/Si=68/32, MX/Si=50/50, and MX/Si=32/68 electrodes were 2710 mAh/g, 2628 mAh/g, 2610 mAh/g, respectively; likewise, the initial Coulombic efficiencies (ICEs) were 56.8%, 68.8%, 71.3%. It should be noted that the capacities reported here are based on the mass of MX/Si capsule. The ICE increased as the MXene content decreased and as the silicon content increased. Reasons for reduced ICE may include trapping of $Li^+$ ions by the surface functional groups on MXene nanosheets.[34] The voltage profiles for selected remaining cycles at 0.5 C are shown in Figure V-8b-d; two plateaus were observed, which is consistent with lithiation and delithiation of silicon.[5]

The $Li^+$ ion diffusion through the MXenes takes place via hoping mechanism as detailed in a computational study by Tang *et al*.[16] The ion diffusion barrier and hoping characteristics highly depend on the distribution of surface functional groups. Thus, the $Li^+$ ion diffusion mechanism in MXenes for our case might be slightly different than that predicted by Tang *et al.* Nevertheless, based on this report we believe that the $Li^+$ ions diffuse through the MXene shell and reach silicon surface for energy storage.

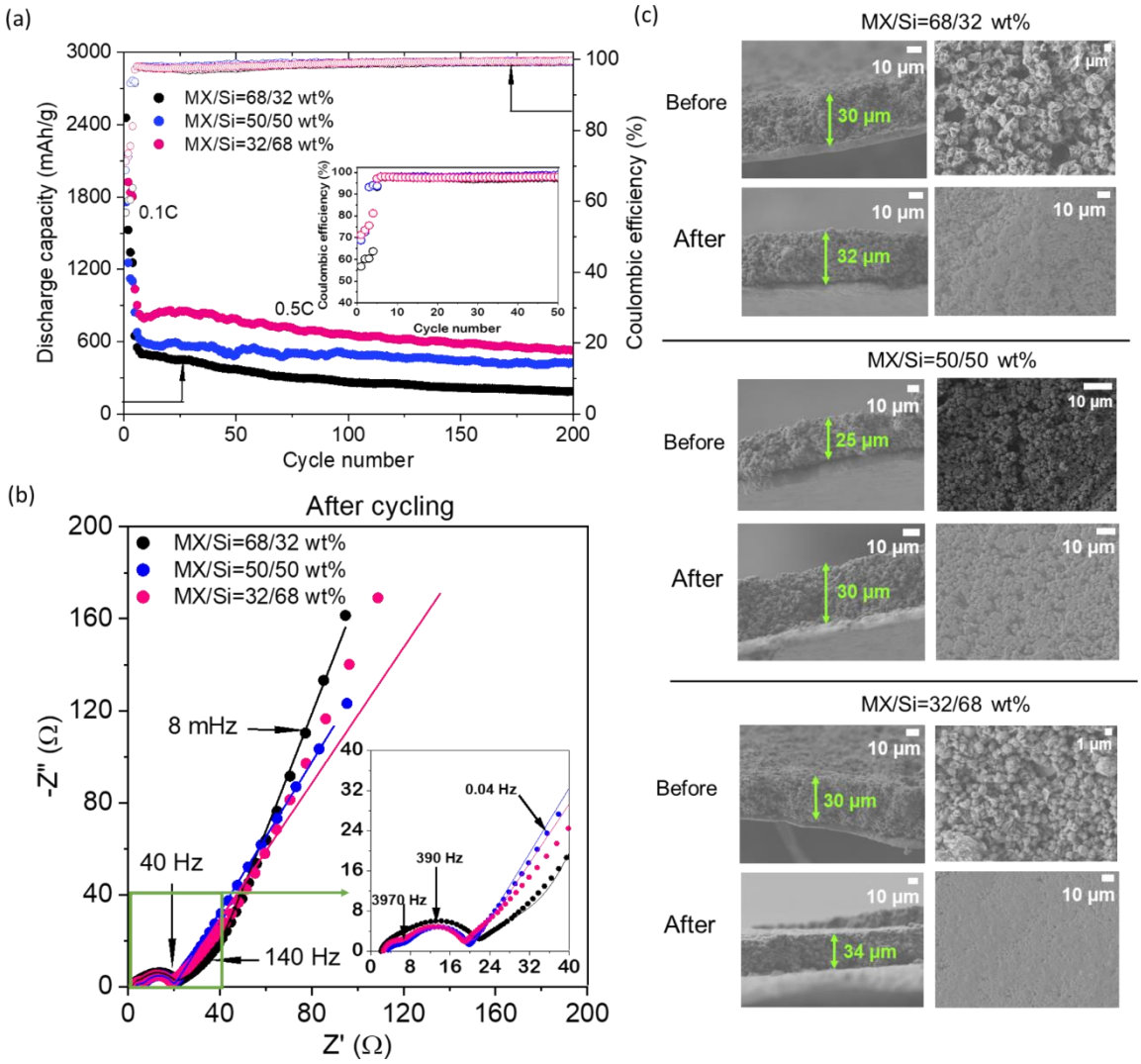


Figure V-7. (a) Galvanostatic charge-discharge for 200 cycles MX/Si=68/32, MX/Si=50/50, and MX/Si=32/68 electrodes with 5 wt% PVDF. Inset shows plot of Coulombic efficiency vs. cycle number for 50 charge-discharge cycles. (b) Nyquist plots (after 100 cycles of charge-discharge). The solid lines represent the equivalent circuit fit to the data. The inset shows a zoomed-in image of the green box. (c) SEM images of electrodes (surface and cross section) before and after 100 cycles. The cross-section SEM images also shows the electrode thickness.

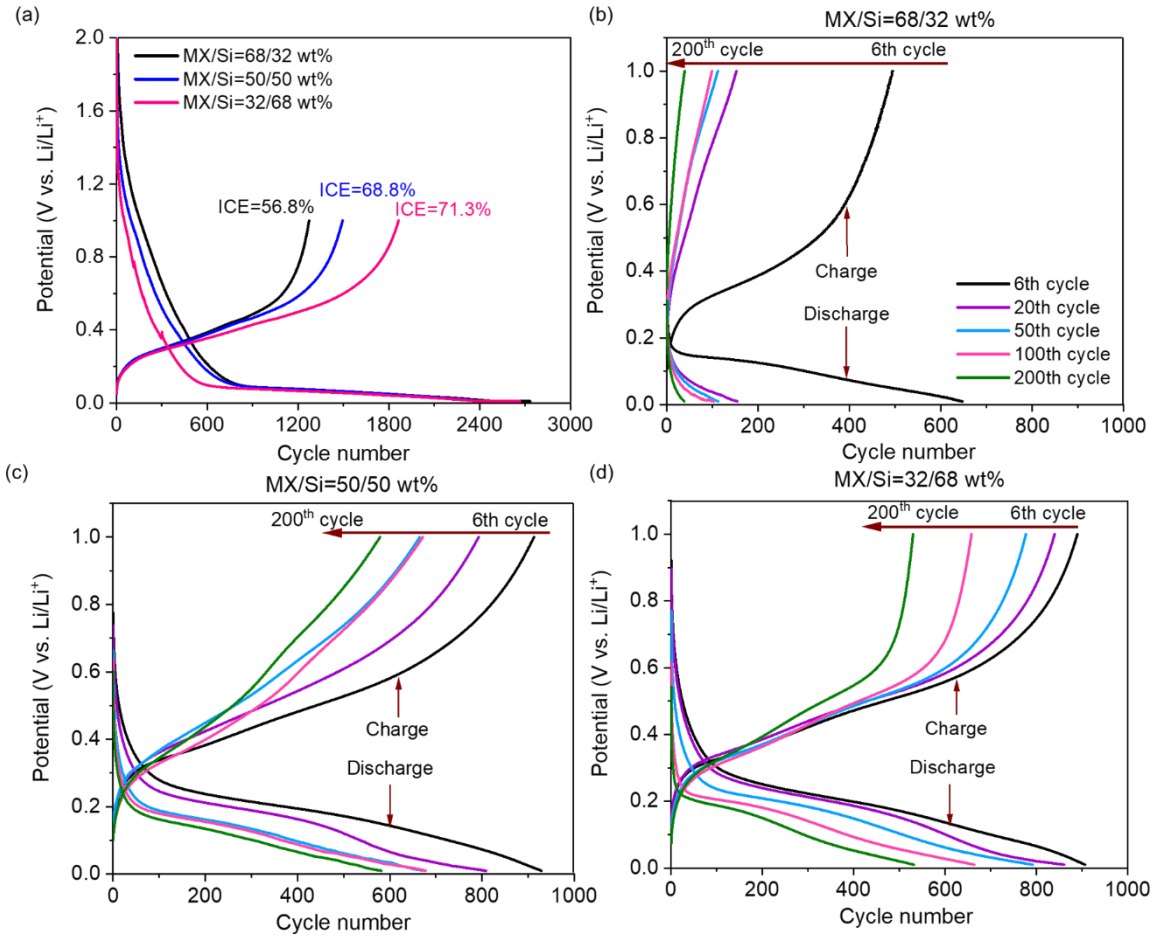


Figure V-8. (a) First cycle voltage profiles of MX/Si=68/32, MX/Si=50/50, and MX/Si=32/68 electrodes at 0.1 C. Initial columbic efficiencies (ICE) are also shown on graph. Voltage profiles at 6$^{th}$, 20$^{th}$, 50$^{th}$, 100$^{th}$, and 200$^{th}$ cycle of (b) MX/Si=68/32, (c) MX/Si=50/50, and (d) MX/Si=32/68 electrode.

The three electrodes were then cycled galvanostatically at 0.1C for the first 5 cycles, and then at 0.5C for 195 cycles. At the conclusion of cycling, the MX/Si=32/68 electrode showed the highest discharge capacity at 0.5 C (580 mAh/g), followed by MX/Si=50/50 and MX/Si=68/32 electrode (420 mAh/g and 200 mAh/g, respectively). This result is in accordance with that observed by Yan *et al.*, in which the highest capacity after cycling was ~620 mAh/g (0.5 C-rate and 200 cycles) for a composition of

Si@MXene/Super P CB/NaCMC (sodium carboxymethyl cellulose)=70/15/15 by mass (with 70 wt% Si and 30 wt% MXenes).[27]

Table V-1. Equivalent circuit fit values for the Nyquist plot (Figure V-7b) obtained from electrochemical impedance spectroscopy performed on crumpled MX/Si=68/32, MX/Si=50/50, and MX/Si=32/68, and uncrumpled electrodes all with 5 wt% PVDF.

| Electrode | Ohmic resistance ($R_O$) | $R_{CT}$ (Ω) | $CPE_{CT}$ (μF) | $R_{SEI}$ (Ω) | $CPE_{SEI}$ (μF) | σ | $D_{Li^+}$ ($cm^2/s$) |
|---|---|---|---|---|---|---|---|
| MX/Si=68/32 | 2.1 | 13.2 | 56.6 | 4.1 | 16.5 | 11.4 | $1.92 \times 10^{-11}$ |
| MX/Si=50/50 | 3.0 | 12.9 | 177 | 4.0 | 78.2 | 12.2 | $9.03 \times 10^{-11}$ |
| MX/Si=32/68 | 2.6 | 14.7 | 259 | 2.0 | 5.51 | 17.2 | $2.17 \times 10^{-11}$ |
| Uncrumpled MX/Si=32/68 | 1.0 | 27.7 | 110 | 125.0 | 4100 | 12.9 | $2.67 \times 10^{-12}$ |

EIS was performed on these electrodes after 100 charge-discharge cycles. The Nyquist plots in Figure V-7b show a generalized EIS response for the three electrodes consisting of two semicircles in the high and medium frequency regions (attributed to the SEI resistance ($R_{SEI}$) and the charge transfer resistance ($R_{CT}$), respectively) followed by a Warburg tail in the low frequency region (attributed to $Li^+$ ion diffusion). The values of $R_{SEI}$, $R_{CT}$, and the $Li^+$ ion diffusion coefficient were obtained by fitting an equivalent circuit (Figure V-6b, Table V-1) to the data. The combined $R_{CT}$ + $R_{SEI}$ values for MX/Si=68/32, MX/Si=50/50, and MX/Si=32/68 electrodes were 17.3 Ω, 16.9 Ω, and 16.7 Ω, respectively. A very minor difference in total resistance was observed for the three electrode compositions tested within which MX/Si=32/68 showed the lowest resistance, which could be a possible explanation for the higher capacities demonstrated by that

electrode composition. The individual $R_{CT}$ and $R_{SEI}$ values for all three electrodes are shown in Table V-1. $R_{CT}$ was lowest for the electrode with the highest MXene content (68 wt%), and $R_{CT}$ increased with decreasing MXene content. $R_{SEI}$, on the other hand, was lowest for the electrode with the lowest MXene content (32 wt%). These results suggest that increasing the MXene loading improves charge transfer, but probably traps large amount of $Li^+$ ions during cycling.[34] We also calculated solid state $Li^+$ ion diffusion coefficient ($D_{Li^+}$) for the electrodes from the Warburg tail in the EIS data. We did not observe a distinct trend in this data, the values were pretty much close to each other: $D_{Li^+}$ for MX/Si=68/32 is 1.92 x $10^{-11}$ $cm^2/s$, MX/Si=50/50 is 9.03 x $10^{-11}$ $cm^2/s$, and MX/Si=32/68 is 2.17 x $10^{-11}$ $cm^2/s$. Therefore, the amount of MXene additive should be balanced to provide sufficient binding and conductive pathways for the silicon nanoparticles, while minimizing the value of $R_{SEI}$. Within this study, the MX/Si=32/68 anode appears to capture this balance.

To further understand the morphology and the SEI development for the electrodes, we performed cross-sectional and surface-SEM analysis (Figure V-7c) on MX/Si=68/32, MX/Si=50/50, and MX/Si=32/68 electrodes before and after 100 cycles. All electrodes showed similar surface morphologies before cycling, consisting of tightly packed MX/Si capsules. This result indicates that the crumpled structure remained intact even after the vigorous mixing required for slurry preparation and electrode processing. Cross-sectional SEM images allowed for the assessment of volume expansion, assuming expansion only through the thickness of electrode; specifically, MX/Si=68/32, MX/Si=50/50, and MX/Si=32/68 electrodes expanded by 10, 20, and 13 %, respectively after 100 cycles. We

did not observe a trend in increase in electrode thickness via SEM analysis. Since it is difficult to measure electrode thickness of the entire electrode due to sample size limitation in SEM, we also measured thicknesses using a Zetasizer (TESA µ-Hite). The MX/Si=68/32, MX/Si=50/50, and MX/Si=32/68 electrodes expanded by 22%, 28%, and 32%, respectively. Here, we observed a trend wherein more the MXenes in the capsules, lower is the increase in electrode thickness after cycling. This trend can be explained as follows: higher the MXene content, lower the content of silicon particles in each capsule, better the ability of capsule to retain silicon's expansion within the capsule. The surface SEM post-cycling for all three electrodes demonstrates a different morphology than the one observed before cycling; the difference being that a SEI layer is observed on electrodes after cycling that coats the MX/Si capsules which were distinctly observed before cycling.

Thus, our analysis shows that MX/Si=32/68 electrode showed highest discharge capacity attributed low charge transfer resistance, improved Coulombic efficiency, and low increase in electrode's thickness after cycling. This is due to proper balance of MXene nanosheets and silicon in the electrode. This can be attributed to the optimum ratio of MX and silicon that allowed expansion of silicon particles within the capsule without diluting the active silicon material with unnecessarily huge amounts MXenes. All further electrochemical characterizations are performed on MX/Si=32/68 electrode.

As stated previously, we made electrodes of loading in the range of 1-1.5 mg/cm$^2$. To recap, here loading refers to the mass of MX/Si capsule/area of electrode. We note that high mass loadings (>1.5 mg/cm$^2$) are required for practical applications.[35] Thus, we made

electrodes with silicon loading of 1.8, 2.2 and 2.8 mg/cm$^2$. We performed peel test to determine the adhesion of these electrodes to the current collector (Figure V-9a). We observed that as the loading was increased, the adhesion decreased, evident from extent of electrode peeling off from the Cu foil current collector. Nonetheless, we made cells and observed that as the loading was increased the capacity decreased, where electrode with loading of 1.8 mg/cm$^2$ and 2.8 mg/cm$^2$ demonstrated capacities of 400 mAh/g and 280 mAh/g, respectively (Figure V-9b). Thus, we choose to make electrodes with an optimum mass loading of 1-1.5 mg/cm$^2$.

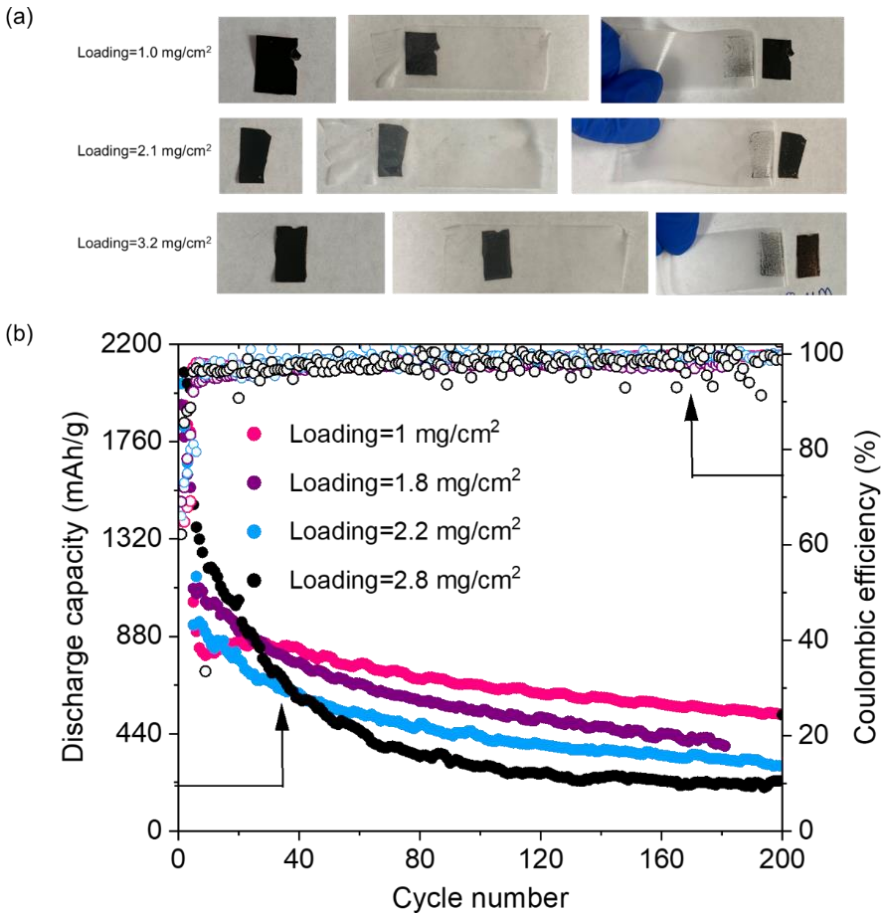


Figure V-9. (a) Peel test on MX/Si=32/68 electrode for different mass loadings. Here mass loading is based on mass of MX/Si capsule. (b) Galvanostatic cycling of MX/Si=32/68 electrode for different Si/MXene capsule loading. For loading of 1 mg/cm$^2$, we cycled the electrode in CC-CV mode for first cycle at 0.1 C, followed by cycling at 0.5 C for remaining cycles. For loading greater than 1 mg/cm$^2$, we cycled electrodes at low C-rates of 0.1 C (first cycles in CC-CV mode at 0.1 C).

Figure V-10a-b shows the rate performance of MX/Si=32/68 electrode performed at different C-rates from 0.05 C to 3 C. The initial discharge capacity of the electrode at 0.05 C-rate was 1120 mAh/g and it reduced to a capacity value of ~780 mAh/g at the 5$^{th}$ cycle at 0.2 C. As the C-rate was further increased to 0.5 C, the capacity reduced further to a value of ~420 mAh/g. The drop in capacity at high C-rates can be attributed to

diffusion imitation of $Li^+$ ions.[21] Almost 85% capacity was received when the C-rate was brought back to 0.5 C. This 15% loss in capacity can be attributed to some electrical disconnection and/or due to SEI formation.[36, 37]

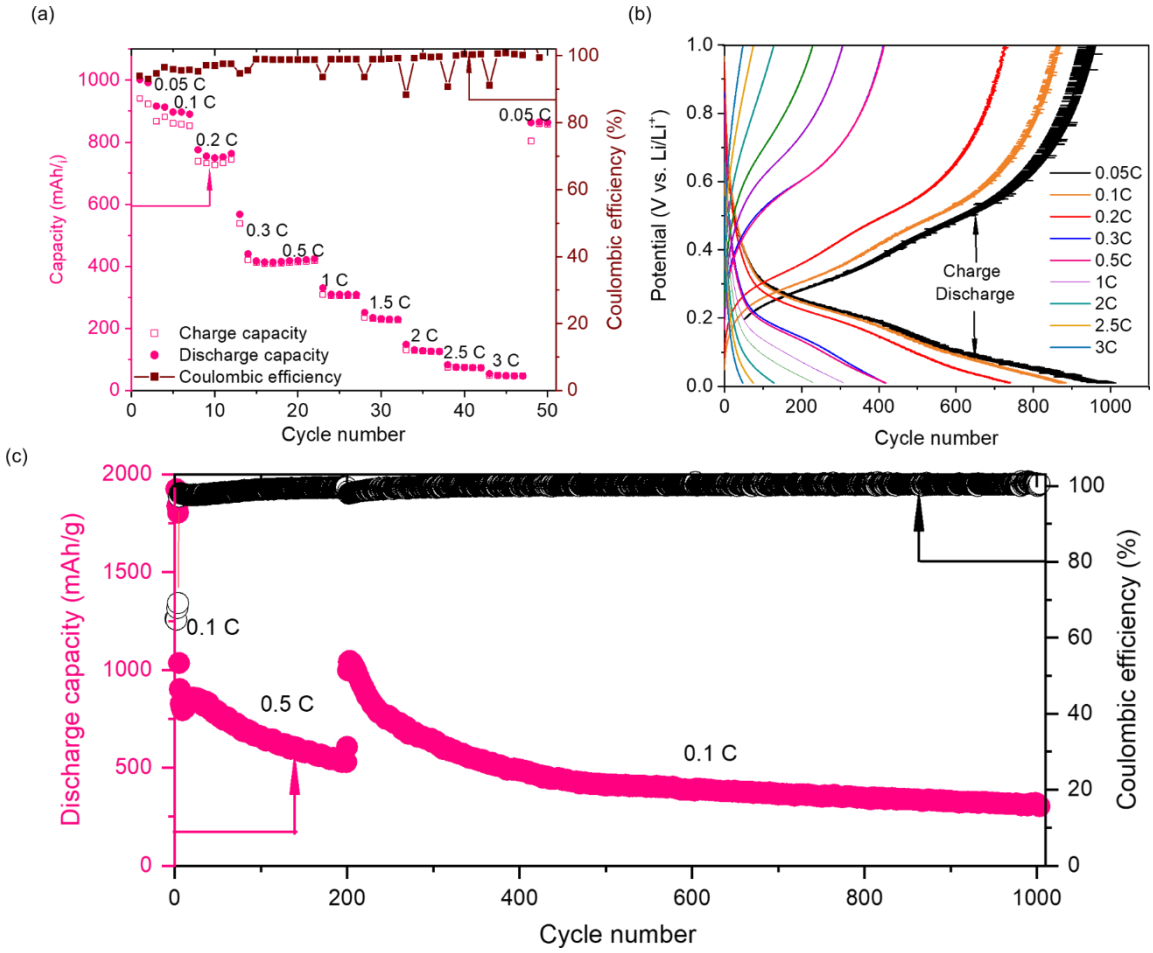


Figure V-10. (a) Galvanostatic cycling and (b) voltage profiles at different C-rates ranging from 0.05 C to 3 C for MX/Si=32/68 electrode. Voltage profile for the third cycle at each C-rate is shown. The electrode was cycled three times at 0.05 C-rate and five times each at the remaining C-rates. The C-rate was brought back to 0.05 C to determine capacity recovery. (c) Long-term galvanostatic cycling of MX/Si=32/68 electrode at C-rate of 0.1 C for first five cycles in CC-CV mode, followed by cycling at 0.5 C in CC mode for 195 cycles, and then cycling at 0.1 C in CC mode for the remaining 800 cycles.

To evaluate the MX/Si=32/68 electrode's stability over large number of cycles, we performed GCD in CC-CV mode for first five cycles, followed by cycling at 0.5 C in CC mode for 195 cycles, and then cycling at 0.1 C for the remaining 800 cycles (Figure V-10c). The C-rate was switched to 0.1 C after 200 cycles so as to minimize the degradation of lithium metal during long term cycling which occurs at high C-rates.[38] The electrode showed a discharge capacity value of ~580 mAh/g at 200$^{th}$ cycle at 0.5 C. When the C-rate was lowered to 0.1 C, the capacity increased to 1015 mAh/g, which then stabilized to a value of ~400 mAh/g. The initial Coulombic efficiency (CE) value was 65.5% which increased to 97% within the first 10 cycles and then stabilized to a value to ~99.8% at the final cycle. This long-term cycling stability and high CE values can be attributed to stable SEI formation and suppressed volumetric expansion due to effective wrapping of MXene nanosheets around silicon nanoparticles.

Next, we compared the galvanostatic cycling performance of our electrodes to the core-shell structured electrodes reported in literature. We found that our electrodes demonstrated higher capacities than Ref. [26], [39], [40], [41], [42], [43], [44], [45] and lower capacities than [27, 28], [46], [35], [13], [47], [48], [49], [50], [51] (capacities compared at similar C-rates). We specifically compared our electrode's performance to those reported Yan *et al*. They fabricated electrodes using spray-dried Si/MXene capsules with 15 wt% NaCMC binder and 15 wt% Super P carbon black (CB) conductive additives and reported a capacity of ~400 mAh/$g_{total}$ at 500$^{th}$ cycle.[27] We made electrodes by adding just 5 wt% PVDF binder to our Si/MXene capsules (no carbon was added) and also observed a similar discharge capacity of ~380 mAh/$g_{total}$ at 1000$^{th}$ cycle at the same C-rate. We believe that usage of excessive binders

and conductive additives can be avoided to further increase the total electrode capacity. This capacity can be further improved by pre-lithiation, modifying silicon surface, modifying electrolyte, which is beyond the scope of this study.

We compared performance of spray-dried MX/Si capsules with rGO/Si capsules. For this, we first synthesized GO using previous reports[52] and fabricated crumpled rGO/Si=32/68 electrodes following the same procedure as we used to make MX/Si=32/68 electrodes. Prior to electrode processing, an additional step to make reduced GO was performed by heating the crumpled product at 200 °C for 2 h. The SEM images (Figure V-11a, b) of rGO/Si=32/68 crumpled product shows rGO/Si capsules with some exposed silicon nanoparticles outside the capsules. This implies that 32 wt% of GO amount was not sufficient to encapsulate all silicon nanoparticles which can be probably attributed to lower lateral size of GO (150-600 nm) as compared to our MXene nanosheets (1- 1.5 µm).[21] The GCD data shows that rGO/Si=32/68 electrode showed poorer capacities (350 mAh/g) than MX/Si=32/68 electrode (580 mAh/g) (Figure V-11c). The EIS data further showed that higher resistances for rGO/Si=32/68 electrode as compared to MX/Si=32/68 electrode (Figure V-11d). This can be attributed to excessive SEI formation on the exposed silicon nanoparticles in rGO/Si=32/68 electrode. Also, rGO have less surface hydroxyl groups which reduces favourable hydrogen bonding interactions with silicon's surface. Lastly, rGO has higher $Li^+$ ion diffusion barrier than MXenes[16, 17] which further increases $Li^+$ ion diffusion, thus has poor capacities during cycling. Thus, we show that for the same electrode composition, MXenes performed better than GO.

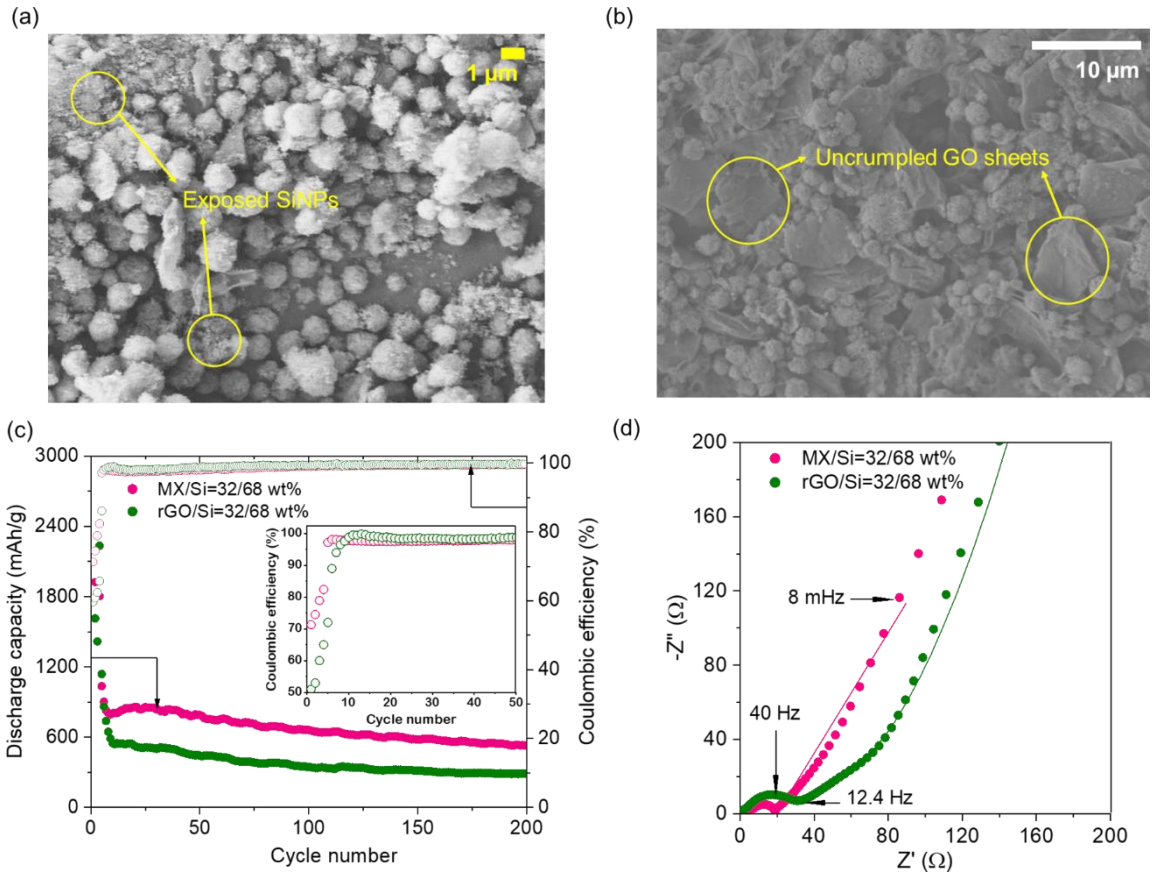


Figure V-11. SEM image of (a) crumpled rGO/Si=32/68 powder and (b) the slurry-cast crumpled rGO/Si=32/68 electrode on Cu foil. (c) Galvanostatic charge-discharge of rGO/Si=32/68 and MX/Si=32/68 electrode for 200 cycles. Inset shows a plot of Coulombic efficiency vs. cycle number for 50 charge-discharge cycles. (d) Nyquist plot of rGO/Si=32/68 and MX/Si=32/68 electrode after 100 cycles of charge-discharge obtained by EIS.

Figure V-12a shows cyclic voltammogram (CV) at different scan rates. As the scan rate was increased, the separation between anodic and cathodic peaks increased, and at scan rates >0.4 mV/s, the peaks became slightly indistinguishable. This can be attributed to diffusion limitation of $Li^+$ ions at high scan rates.[53]

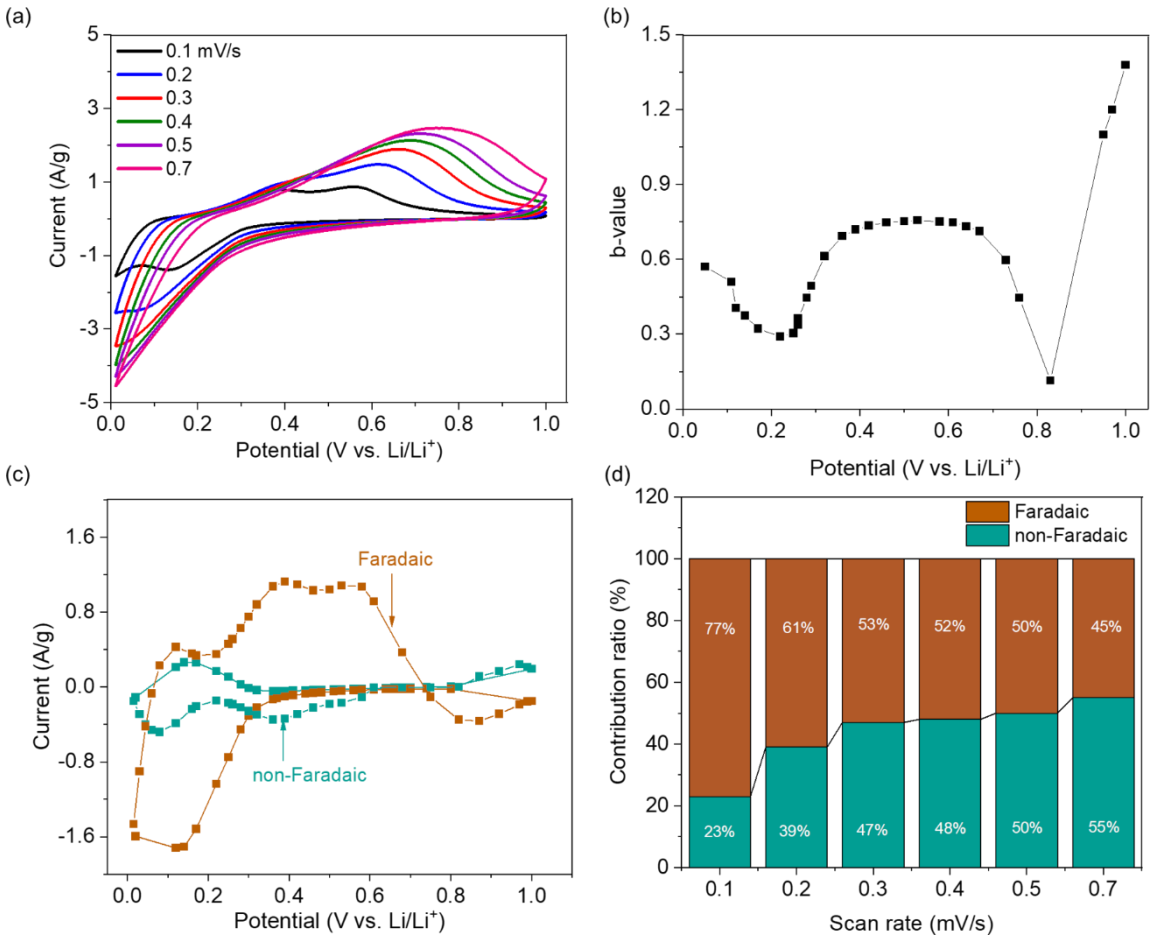


Figure V-12. (a) Cyclic voltammogram of MX/Si=32/68 electrode at different scan rates of 0.1, 0.2, 0.3, 0.4, 0.5, and 0.7 mV/s. Cells were conditioned at 0.1 C for three cycles before performing cyclic voltammetry. (b) b-values at selected different potentials. (c) Cyclic voltammogram at 0.1 mV/s. Faradaic and non-Faradaic contributions are shown in brown and cyan, respectively. (d) Contribution ratio of the Faradaic and non-Faradaic charge storage at different scan rates.

It is well-known that silicon is associated with alloying reactions and MXene is recognized as a pseudocapacitive materials due to its surface redox reactions.[54] To further understand this behavior, we calculated *b*-values at different potentials as shown in Figure V-12b following previous reports.[34] The *b*-values are calculated using the following equation (Eqn 5.1)

$$i(V)=av^{b} \quad \ldots(5.1)$$

where, both *a* and *b* are adjustable values, *v* is scan rate, and *i(V)* is current at a given voltage. *b*-Value can be derived from the slope of the log(*v*) − log(*i(V)*) plots. Generally, b = 0.5 implies a Faradaic response (or a diffusion-controlled behaviour), while b = 1 relates to a non-Faradaic response (or a capacitive process free of diffusion limitations). As seen in Figure V-12b, the *b*-value was close to 0.5 in the voltage window of 0.3 to 0.7 V *vs.* $Li/Li^{+}$ which response was mostly Faradaic in nature. However, at potentials >0.7 V *vs.* $Li/Li^{+}$, the *b*-value was closer to 1, which implies the response was non-Faradaic.

The Faradaic and non-Faradaic charge storage contributions at specific scan rates can be calculated quantitatively according to Eqn 5.2.

$$i(V)=a1\times v+a2\times v^{\frac{1}{2}} \ldots \quad (5.2)$$

where $a2 \times v^{1/2}$ and $a1 \times v$ are Faradaic and non-Faradaic response current, respectively. As seen in Figure V-12d, 77% of the total $Li^{+}$ ion storage capability is coming from Faradaic response at low scan rate of 0.1 mV/s. As the scan rate was increased, the non-Faradaic effect of the composite electrode is gradually enhanced, reaching 55% at 0.9 mV/s. These results suggest that the energy storage process of the MX/Si=32/68 electrode is in accordance with the battery-capacitive dual-model energy storage (DMES) mechanism, which is beneficial to long-cycling stability.

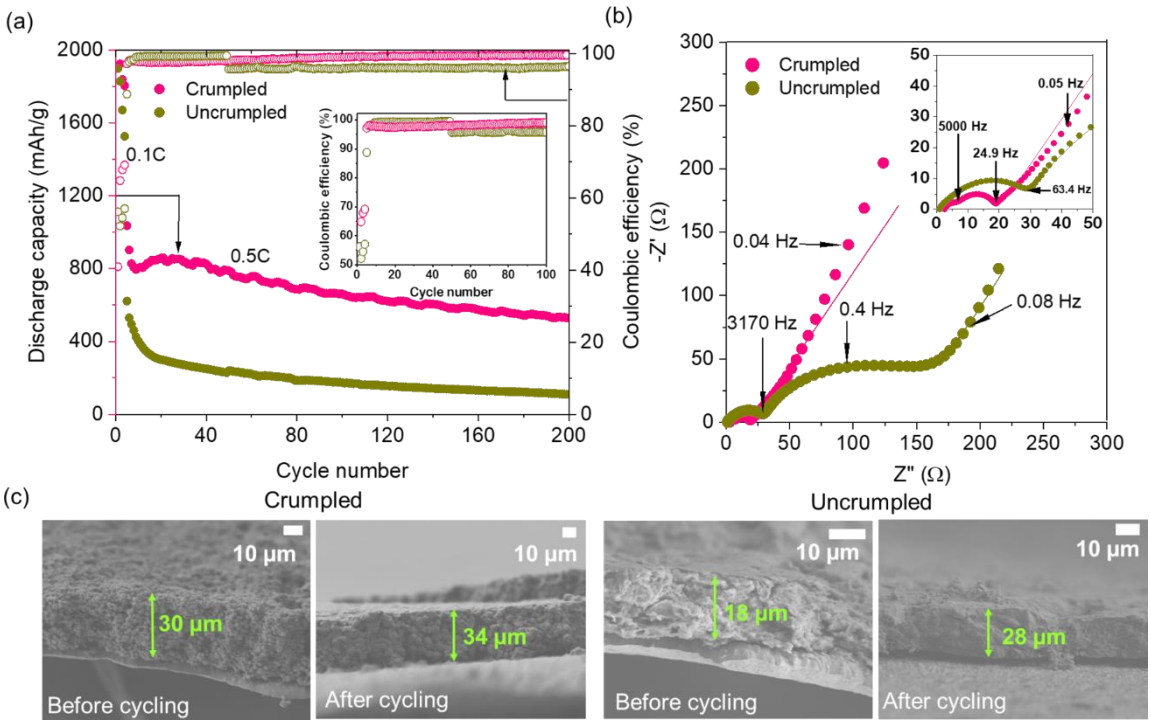


Figure V-13. (a) Galvanostatic charge-discharge of MX/Si=32/68 crumpled and non-crumpled electrode for 200 cycles. Inset shows a plot of Coulombic efficiency vs. cycle number for 100 cycles. (b) EIS (after 100 cycles of charge-discharge) of MX/Si=32/68 crumpled and non-crumpled electrode. Inset shows zoomed in part of the Nyquist plot. (c) Cross-section SEM images of MX/Si=32/68 crumpled and non-crumpled electrode before and after 100 cycles of charge-discharge.

We compared the performance of crumpled MX/Si=32/68 architecture to a non-crumpled one. To make the non-crumpled electrode, 65 wt% silicon nanoparticles, 30 wt% MXene nanosheets, and 5 wt% PVDF were mixed to form a slurry which was cast on Cu foil. The same electrode fabrication and battery assembly procedures were followed. We observed that the crumpled electrode showed higher capacities (580 mAh/g) than the non-crumpled one (~200 mAh/g) (Figure V-13a). This observation was further supported by EIS, where the $R_{CT}$+$R_{SEI}$ of the non-crumpled electrode (153 Ω) was higher than the crumpled electrode (16.7 Ω) (Figure V-13b, Table V-1). The surface SEM images of the

uncrumpled electrode revealed patchy SEI layer as compared to the smooth SEI layer observed on crumpled electrode (Figure V-14). The cross-section SEM images after cycling (after 100 cycles of charge-discharge) reveal that the electrode thickness increased by ~55% for the non-crumpled electrode as opposed to the crumpled electrode (13%) (Figure V-13c). This shows that crumpled electrode was able to alleviate the volumetric expansion to some extent and thus maintain the electrode's integrity. On contrast, non-crumpled electrode showed an enormous increase in electrode's thickness after cycling. This can be attributed to excessive SEI buildup owing to exposure of silicon particles to the electrolyte, inability of the flat MXene nanosheets to sustain volumetric expansion of silicon particles, electrical disconnection of lithiated silicon particles. All these factors are responsible for poor capacities of the uncrumpled electrode.

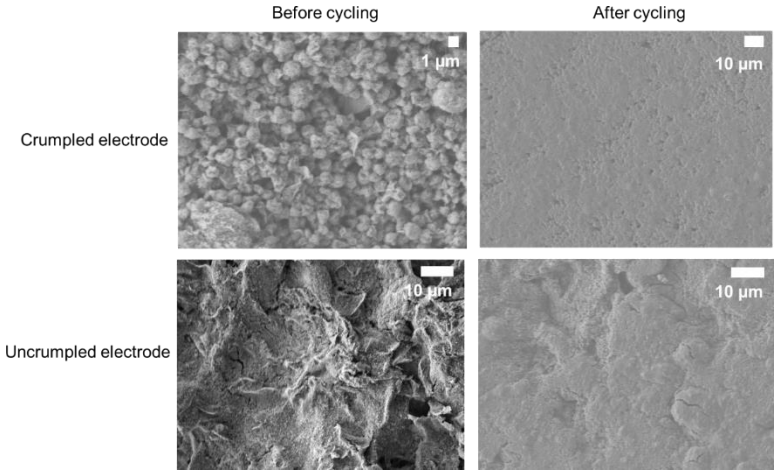


Figure V-14. Surface SEM images of crumpled and uncrumpled electrode before and after 100 cycles of charge-discharge.

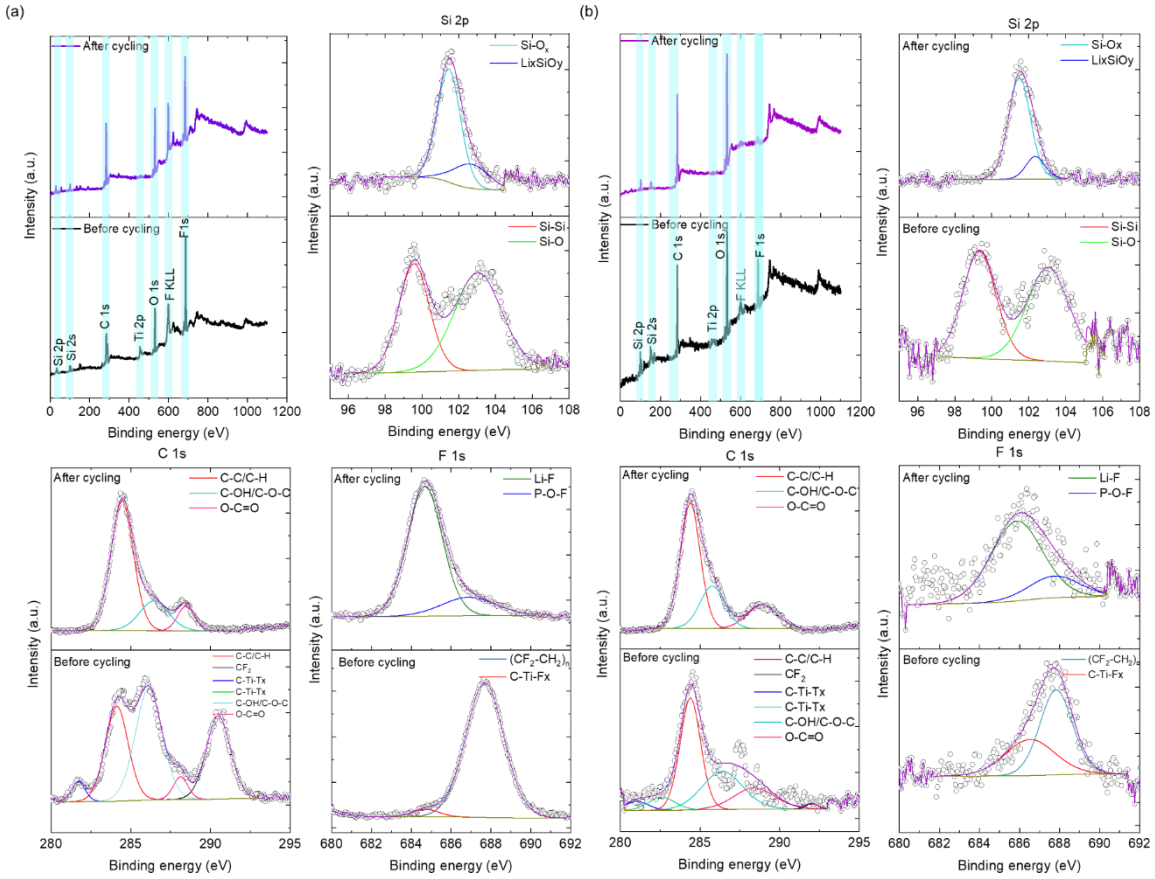


Figure V-15. Survey scan and deconvoluted Si 2p, C 1s, and F 1s peaks obtained using X-ray photoelectron spectroscopy for (a) crumpled and (b) uncrumpled MX/Si=32/68 electrode before and after 100 cycles of charge-discharge.

To evaluate the SEI layer formed on the crumpled and uncrumpled MX/Si=32/68 electrode's surface after cycling, we performed XPS analysis before and after 100 cycles (Figure V-15and Figure V-16). We first analyzed the peaks observed for both crumpled and uncrumpled electrodes before cycling. The XPS survey scan of both the electrodes before cycling reveal presence of C 1s, O 1s, F 1s, Si 2p, and Ti 2p; with the atomic%

listed in Table V-2. The deconvoluted C 1s spectra shows presence of $CF_2$ (~292 eV) peak attributed to bonds present in PVDF binder along with C-C/C-H (284.5 eV), symmetric C-Ti-Tx (~281.7 eV, 280 eV), C-OH/C-O-C (~286.1), and O-C=O (~288.1 eV) peaks from MXene nanosheets. The deconvoluted O 1s spectra for crumpled MX/Si=32/68 electrode shows peaks attributed to MXene nanosheets (C-Ti-$OH_x$ ~531.2 eV, C-Ti-$O_x$ ~530 eV, $TiO_2$ ~529.8 eV, $Al_2O_3$ ~532.7 eV, and $H_2O$ ~533 eV) and a peak attributed to possible bond formation between silicon particles and MXene nanosheets (Si-O-Ti ~531.2 eV). We did not observe Si-O-Ti peak for the case of uncrumpled electrode. The deconvoluted F 1s peak shows presence of C-F (~687.8 eV) and C-Ti-$F_x$ (~684.7 eV), and that for deconvoluted Si 2p peak shows presence of Si-Si (~99.8 eV) and Si-O (~103 eV) peaks. The deconvoluted Ti 2p peak shows several bonds which are typically present in MXene nanosheets.[31] The Ti peak was not distinctly observed for the case of uncrumpled electrode and thus we did not deconvolute it further. The deconvoluted peaks were verified from previous reports.[30, 55]

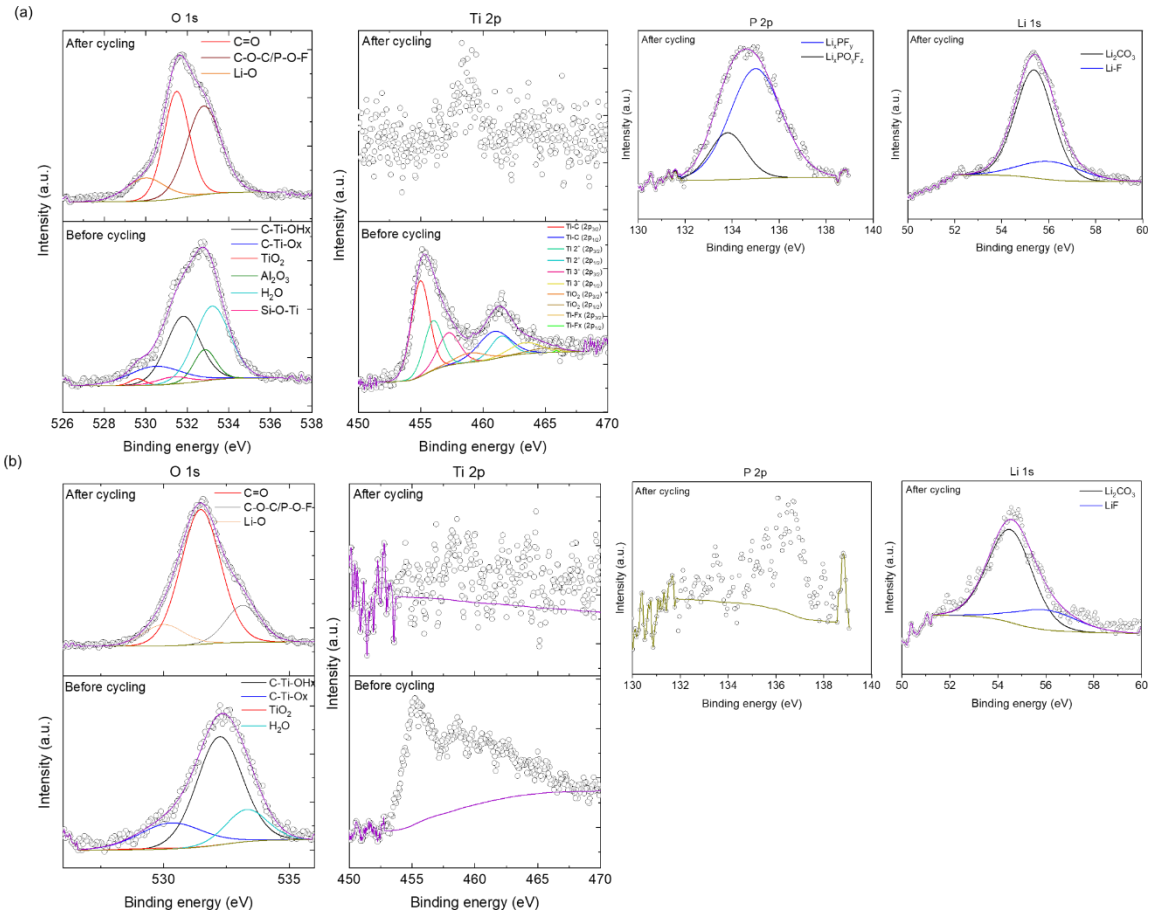


Figure V-16. Deconvoluted O 1s and Ti 2p before and after cycling, and P 2p and Li 1s after cycling for (a) crumpled and (b) uncrumpled MX/Si=32/68 electrode.

We then analyzed the peaks observed for both crumpled and uncrumpled electrode after cycling. The XPS survey scan of both electrodes after cycling shows presence of Li 1s and P 2p, which is attributed to the SEI layer, in addition to the peaks observed before cycling. We further deconvoluted the peaks to evaluate the SEI composition. The deconvoluted peaks of Li, F, and P revealed presence of LiF, $Li_2CO_3$, POF, and $Li_xSiO_y$, $Li_xPO_yF_z$, $Li_xPF_y$, $SiO_x$ from the decomposition of EC, DEC, FEC, and $LiPF_6$ salt, which are typically observed in silicon anode's SEI layer as reported previously.[55-58] We

observed a drop in atomic% of Si, Ti, F and C, which is because of electrode getting buried under the SEI layer. For the case of crumpled electrodes, we observed a drop in Si and Ti content by 72.5% and 82.5%, respectively. For the case of uncrumpled electrodes, we observed a higher drop in Si and Ti content, 82.1% and 85.7%, respectively (Table V-2). This could be a possible indication of more SEI formation on uncrumpled electrodes as compared to the crumpled electrodes. This is further supported by the EIS data (Table V-1and Figure V-13b) where uncrumpled electrodes after cycling showed higher $R_{SEI}$ (125 Ω) as compared to crumpled electrodes (2 Ω).

Table V-2. Atomic% of different elements in crumpled and uncrumpled MX/Si=32/68 electrode before and after cycling.

| Elements | Atomic% | | | |
|---|---|---|---|---|
| | Crumpled electrode | | Uncrumpled electrode | |
| | Before cycling | After cycling | Before cycling | After cycling |
| C 1s | 50.7 | 36.7 | 47.0 | 43.2 |
| O 1s | 15.5 | 13.6 | 21.4 | 20.9 |
| F 1s | 20.3 | 11.5 | 8.51 | 1.79 |
| Si 2p | 11.3 | 3.10 | 22.4 | 4.00 |
| Ti 2p | 2.11 | 0.37 | 0.70 | 0.10 |
| Li 1s | - | 33.1 | - | 29.7 |
| P 2p | - | 1.50 | - | 0.30 |

Finally, we compared the long-term cycling performance and rate performance of our electrodes to those reported in literature. First, we compared the cycling performance of our electrodes to other reports that used non MXene core-shell geometries (Figure V-17a) and to Si/MXene electrodes (Figure V-17b). Generally, we observed that our

crumpled MX/Si electrodes (data in pink) were able to achieve higher capacities at higher current densities (with a few exceptions[35, 46]). To be specific, our crumpled electrodes achieved specific energy of 550 Wh/$kg_{total}$ at specific power of 1720 W/$kg_{total}$ at 200$^{th}$ cycle. Particularly, we noticed that we were able to obtain higher silicon content in our electrodes, with a few exceptions.[18, 21, 28] The previously reported flat MX/Si electrode showed higher capacities than our electrodes, probably because of lower electrode loading (<1 mg/$cm^2$) for the former. Yan *et al.*, reported that there crumpled MX/Si electrodes can sustain much higher current densities (~2 A/g) and achieve capacities of ~400 mAh/$g_{total}$.[27] On the other hand, our crumpled electrodes can sustain current densities upto ~1.7 A/g and achieve capacities of ~550 mAh/$g_{total}$.

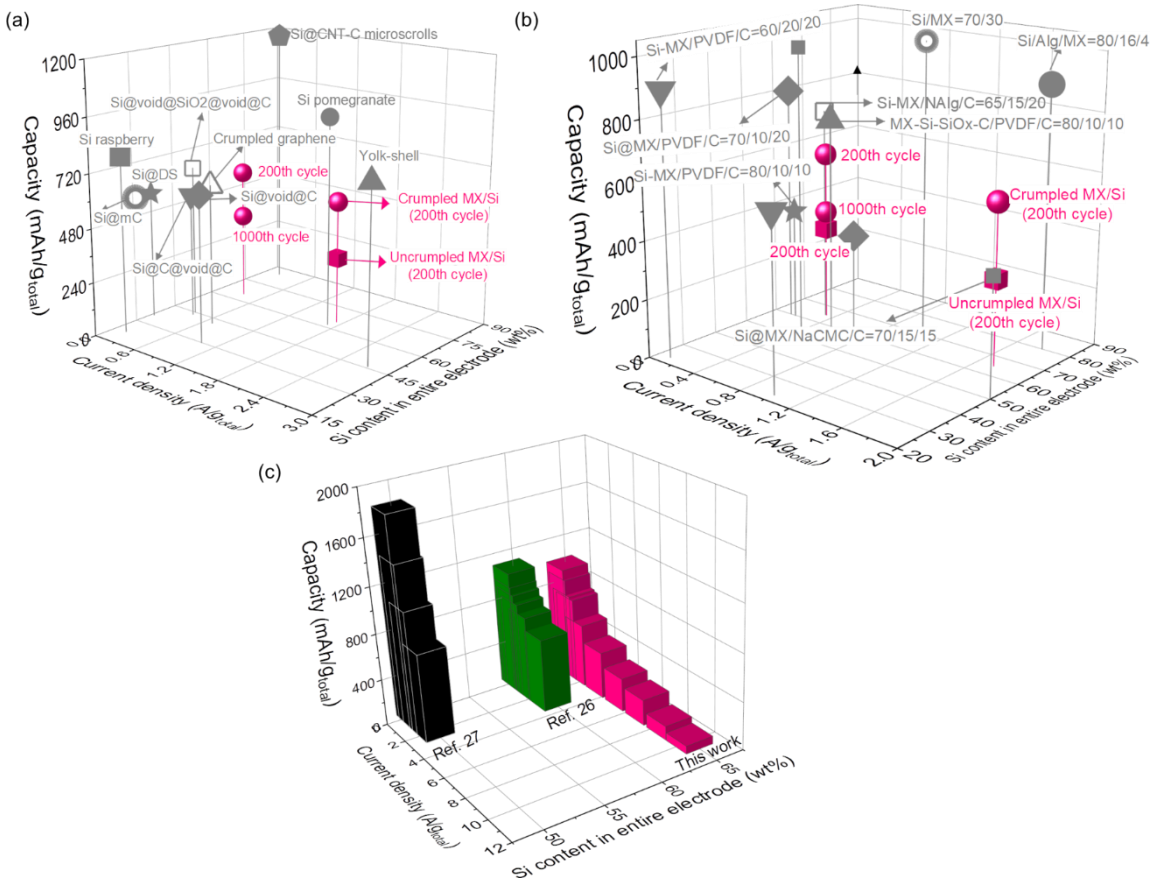


Figure V-17. (a) 3D plot of cycling electrode capacity (at n$^{th}$ cycle) (mAh/g$_{total}$), current density (A/g$_{total}$), and silicon content in entire electrode comparing (a) yolk-shell type electrode architectures available in literature and (b) Si/MXene electrode architectures. (c) 3D plot of rate performance comparing yolk-shell type Si/MXene architectures available in literature. Here mass of total electrode is considered.

Next, we compared the rate performance with previously reported core-shell MX/Si electrodes (Figure V-17c). Here, the electrode performance reported by Yan *et al*. was exceptional. But, our electrodes showed comparable performance to those reported by Xia *et al*.[26] However, we noted that our electrode can sustain higher current densities (upto ~15 A/g). Thus, we our electrodes can possibly find application in devices which require high power over high capacities, with volume constrain.

## Conclusions

Here, we made MXene/Si core-shell type structure using a one-step spray drying procedure. The spray drying technique is scalable and can be easily applied to other anodes where volumetric expansion and excessive SEI formation is an issue. We optimized the Si/MX content in the capsule as well the PVDF binder content in the electrode to increase the active material loading. The high capacities observed for Si/MX=32/68 wt% electrode with 5 wt% PVDF binder is attributed to balance of MXene and silicon nanoparticles in a capsule. This balance allowed for achieving high silicon loading without diluting the active material toa large extent. We show that our crumpled electrodes demonstrated specific capacity of 550 mAh/$g_{total}$ at a current density of 1.7 A/$g_{tota}$l (or 0.5 C-rate) at 200$^{th}$ cycle for electrode loading of 1.5 mg/cm$^2$. We further showed that our crumpled electrodes showed a decent cycling capacity of ~400 mAh/$g_{total}$ at 200$^{th}$ cycle at current density of 0.3 A/$g_{total}$ (or 0.1 C-rate). b-Value analysis revealed that electrodes exhibited dual energy storage mechanism, wherein silicon and MXenes stored Faradaic and non-Faradaic energy, respectively. We showed that MXenes are better than rGO by presenting SEM and cycling data which revealed that MXenes wrapped the silicon particles more effective than rGO due to larger lateral size of the former which overall helped in achieving higher cycling capacities. An in-house comparison of crumpled architecture to the uncrumpled architecture revealed the advantages of effective wrapping of silicon particles by MXene nanosheets which minimized SEI formation and improved cycle life of anode. XPS and EIS analysis showed that large amounts of SEI had formed on cycled uncrumpled electrodes as compared to the crumpled electrodes. Compared to previous literature on

yolk-shell and flat Si/MX electrodes, our electrodes showed comparable cycling performance. Practically, our crumpled electrodes had showed comparable capacities at higher power. Our crumpled electrodes had second highest silicon content in the entire electrode as compared to other reported yolk-shell electrodes. Thus, by reducing the unnecessary inactive material content, the active material content can be further increased. Thus to conclude, our crumpled electrodes can be possibly used in devices requiring high power.

**References**


1. Li, J.-Y.; Xu, Q.; Li, G.; Yin, Y.-X.; Wan, L.-J.; Guo, Y.-G., Research Progress Regarding Si-Based Anode Materials Towards Practical Application in High Energy Density Li-Ion Batteries. *Mater. Chem. Front.* **2017,** *1* (9), 1691-1708.
2. Choi, J. W.; Aurbach, D., Promise and Reality of Post-Lithium-Ion Batteries With High Energy Densities. *Nat. Rev. Mater.* **2016,** *1* (4), 1-16.
3. Aricò, A.; Bruce, P.; Scrosati, B., Nanostructured Materials for Advanced Energy Conversion and Storage Devices. *Nat. Mater.* **2005,** *4*, 366–377.
4. Choi, S.; Wang, G., Advanced Lithium-Ion Batteries for Practical Applications: Technology, Development, and Future Perspectives. *Adv. Mater. Technol.* **2018,** *3* (9), 1700376.
5. McDowell, M. T.; Lee, S. W.; Nix, W. D.; Cui, Y., 25th Anniversary Article: Understanding the Lithiation of Silicon and Other Alloying Anodes for Lithium-Ion Batteries. *Adv. Mater.* **2013,** *25* (36), 4966-85.
6. Franco Gonzalez, A.; Yang, N.-H.; Liu, R.-S., Silicon Anode Design for Lithium-Ion Batteries: Progress and Perspectives. *J. Phys. Chem. C* **2017,** *121* (50), 27775-27787.
7. Casimir, A.; Zhang, H.; Ogoke, O.; Amine, J. C.; Lu, J.; Wu, G., Silicon-Based Anodes for Lithium-Ion Batteries: Effectiveness of Materials Synthesis and Electrode Preparation. *Nano Energy* **2016,** *27*, 359-376.
8. Liu, X. H.; Zhong, L.; Huang, S.; Mao, S. X.; Zhu, T.; Huang, J. Y., Size-Dependent Fracture of Silicon Nanoparticles During Lithiation. *ACS Nano* **2016,** *6* (2), 1522-1531.
9. Ashuri, M.; He, Q.; Shaw, L. L., Silicon as a Potential Anode Material for Li-Ion Batteries: Where Size, Geometry and Structure Matter. *Nanoscale* **2016,** *8* (1), 74-103.
10. Zamfir, M. R.; Nguyen, H. T.; Moyen, E.; Lee, Y. H.; Pribat, D., Silicon Nanowires for Li-Based Battery Anodes: A Review. *J. Mater. Chem. A* **2013,** *1* (34), 9566.

11. Wu, H.; Chan, G.; Choi, J. W.; Ryu, I.; Yao, Y.; McDowell, M. T.; Lee, S. W.; Jackson, A.; Yang, Y.; Hu, L.; Cui, Y., Stable Cycling of Double-Walled Silicon Nanotube Battery Anodes Through Solid-Electrolyte Interphase Control. *Nat. Nanotechnol.* **2012,** *7* (5), 310-5.
12. Ryu, J.; Hong, D.; Lee, H.-W.; Park, S., Practical Considerations of Si-Based Anodes for Lithium-Ion Battery Applications. *Nano Research* **2017,** *10* (12), 3970-4002.
13. Luo, J.; Zhao, X.; Wu, J.; Jang, H. D.; Kung, H. H.; Huang, J., Crumpled Graphene-Encapsulated Si Nanoparticles for Lithium Ion Battery Anodes. *J. Phys. Chem. Lett.* **2012,** *3* (13), 1824-9.
14. Naguib, M.; Mochalin, V. N.; Barsoum, M. W.; Gogotsi, Y., 25th Anniversary Article: MXenes: A New Family of Two-Dimensional Materials. *Adv. Mater.* **2014,** *26* (7), 992-1005.
15. Naguib, M.; Kurtoglu, M.; Presser, V.; Lu, J.; Niu, J.; Heon, M.; Hultman, L.; Gogotsi, Y.; Barsoum, M. W., Two-dimensional nanocrystals produced by exfoliation of Ti3 AlC2. *Adv. Mater.* **2011,** *23* (37), 4248-53.
16. Tang, Q.; Zhou, Z.; Shen, P., Are MXenes Promising Anode Materials for Li Ion Batteries? Computational Studies on Electronic Properties and Li Storage Capability of $Ti_3C_2$ and $Ti_3C_2X_2$ (X = F, OH) Monolayer. *J. Am. Chem. Soc.* **2012,** *134* (40), 16909-16916.
17. Kong, F.; He, X.; Liu, Q.; Qi, X.; Zheng, Y.; Wang, R.; Bai, Y., Effect of $Ti_3AlC_2$ Precursor on the Electrochemical Properties of the RResulting MXene $Ti_3C_2$ for Li-Ion Batteries. *Ceram. Int.* **2018,** *44* (10), 11591-11596.
18. Zhang, C. J.; Park, S. H.; Seral-Ascaso, A.; Barwich, S.; McEvoy, N.; Boland, C. S.; Coleman, J. N.; Gogotsi, Y.; Nicolosi, V., High Capacity Silicon Anodes Enabled by MXene Viscous Aqueous Ink. *Nat. Commun.* **2019,** *10* (1), 849.
19. Kong, F.; He, X.; Liu, Q.; Qi, X.; Sun, D.; Zheng, Y.; Wang, R.; Bai, Y., Enhanced reversible Li-ion storage in Si@Ti3C2 MXene nanocomposite. *Electrochem. Commun.* **2018,** *97*, 16-21.
20. Zhu, X.; Shen, J.; Chen, X.; Li, Y.; Peng, W.; Zhang, G.; Zhang, F.; Fan, X., Enhanced Cycling Performance of Si-MXene Nanohybrids as Anode for High Performance Lithium Ion Batteries. *Chem. Eng. J.* **2019,** *378*, 122212.
21. Sarang, K. T.; Zhao, X.; Holta, D.; Radovic, M.; Green, M. J.; Oh, E. S.; Lutkenhaus, J. L., Minimizing two-dimensional Ti3C2Tx MXene nanosheet loading in carbon-free silicon anodes. *Nanoscale* **2020**.
22. Tian, Y.; An, Y.; Feng, J., Flexible and Freestanding Silicon/MXene Composite Papers for High-Performance Lithium-Ion Batteries. *ACS Appl. Mater. Interfaces* **2019,** *11* (10), 10004-10011.
23. Zhang, F.; Jia, Z.; Wang, C.; Feng, A.; Wang, K.; Hou, T.; Liu, J.; Zhang, Y.; Wu, G., Sandwich-like Silicon/$Ti_3C_2T_x$ MXene Composite by Electrostatic Self-Assembly for High Performance Lithium Ion Battery. *Energy* **2020,** *195*, 117047.
24. Hui, X.; Zhao, R.; Zhang, P.; Li, C.; Wang, C.; Yin, L., Low-Temperature Reduction Strategy Synthesized Si/$Ti_3C_2$ MXene Composite Anodes for High-Performance Li-Ion Batteries. *Adv. Energy Mater.* **2019,** *9* (33), 1901065.

25. Zhang, Y.; Mu, Z.; Lai, J.; Chao, Y.; Yang, Y.; Zhou, P.; Li, Y.; Yang, W.; Xia, Z.; Guo, S., MXene/Si@SiO x@C Layer-by-Layer Superstructure with Autoadjustable Function for Superior Stable Lithium Storage. *ACS Nano* **2019,** *13* (2), 2167-2175.
26. Xia, M.; Chen, B.; Gu, F.; Zu, L.; Xu, M.; Feng, Y.; Wang, Z.; Zhang, H.; Zhang, C.; Yang, J., $Ti_3C_2T_x$ MXene Nanosheets as a Robust and Conductive Tight on Si Anodes Significantly Enhance Electrochemical Lithium Storage Performance. *ACS Nano* **2020,** *14* (4), 5111-5120.
27. Yan, Y.; Zhao, X.; Dou, H.; Wei, J.; Sun, Z.; He, Y. S.; Dong, Q.; Xu, H.; Yang, X., MXene Frameworks Promote the Growth and Stability of LiF-Rich Solid-Electrolyte Interphases on Silicon Nanoparticle Bundles. *ACS Appl. Mater. Interfaces* **2020,** *12* (16), 18541-18550.
28. Wang, H.; Fu, J.; Wang, C.; Wang, J.; Yang, A.; Li, C.; Sun, Q.; Cui, Y.; Li, H., A Binder-Free High Silicon Content Flexible Anode for Li-Ion Batteries. *Energy Environ. Sci.* **2020,** *13* (3), 848-858.
29. Alhabeb, M.; Maleski, K.; Anasori, B.; Lelyukh, P.; Clark, L.; Sin, S.; Gogotsi, Y., Guidelines for Synthesis and Processing of Two-Dimensional Titanium Carbide ($Ti_3C_2T_x$ MXene). *Chem. Mater.* **2017,** *29* (18), 7633-7644.
30. Zhao, X.; Vashisth, A.; Prehn, E.; Sun, W.; Shah, S. A.; Habib, T.; Chen, Y.; Tan, Z.; Lutkenhaus, J. L.; Radovic, M.; Green, M. J., Antioxidants Unlock Shelf-Stable $Ti_3C_2T$ (MXene) Nanosheet Dispersions. *Matter* **2019,** *1* (2), 513-526.
31. Shah, S. A.; Habib, T.; Gao, H.; Gao, P.; Sun, W.; Green, M. J.; Radovic, M., Template-Free 3D Titanium Carbide ($Ti_3C_2T_X$) MXene Particles Crumpled by Capillary Forces. *Chem. Commun. (Camb)* **2016,** *53* (2), 400-403.
32. Echols, I. J.; An, H.; Zhao, X.; Prehn, E. M.; Tan, Z.; Radovic, M.; Green, M. J.; Lutkenhaus, J. L., pH-Response of Polycation/$Ti_3C_2T_x$ MXene Layer-By-Layer Assemblies for Use as Resistive Sensors. *Mol. Syst. Des. Eng.* **2020,** *5* (1), 366-375.
33. Parviz, D.; Metzler, S. D.; Das, S.; Irin, F.; Green, M. J., Tailored Crumpling and Unfolding of Spray-Dried Pristine Graphene and Graphene Oxide Sheets. *Small* **2015,** *11* (22), 2661-8.
34. Cheng, R.; Hu, T.; Zhang, H.; Wang, C.; Hu, M.; Yang, J.; Cui, C.; Guang, T.; Li, C.; Shi, C.; Hou, P.; Wang, X., Understanding the Lithium Storage Mechanism of $Ti_3C_2T_x$ MXene. *J. Phys. Chem. C* **2018,** *123* (2), 1099-1109.
35. Liu, N.; Lu, Z.; Zhao, J.; McDowell, M. T.; Lee, H. W.; Zhao, W.; Cui, Y., A Pomegranate-Inspired Nanoscale Design for Large-Volume-Change Lithium Battery Anodes. *Nat. Nanotechnol.* **2014,** *9* (3), 187-92.
36. Radvanyi, E.; Porcher, W.; De Vito, E.; Montani, A.; Franger, S.; Jouanneau Si Larbi, S., Failure mechanisms of nano-silicon anodes upon cycling: an electrode porosity evolution model. *J. Phys. Chem. Chem. Phys.* **2014,** *16* (32), 17142-53.
37. Yoon, T.; Nguyen, C. C.; Seo, D. M.; Lucht, B. L., Capacity Fading Mechanisms of Silicon Nanoparticle Negative Electrodes for Lithium Ion Batteries. *J. Electrochem. Soc.* **2015,** *162* (12), A2325-A2330.

38. Choi, S.; Kwon, T.-w.; Coskun, A.; Choi, J. W., Highly Elastic Binders Integrating Polyrotaxanes for Silicon Microparticles Anode in Li Ion Batteries. *Science* **2017,** *357*, 279-283.
39. Yang, L. Y.; Li, H. Z.; Liu, J.; Sun, Z. Q.; Tang, S. S.; Lei, M., Dual Yolk-Shell Structure of Carbon and Silica-Coated Silicon for High-Performance Lithium-Ion Batteries. *Sci. Rep.* **2015,** *5*, 10908.
40. Sun, Z.; Song, X.; Zhang, P.; Gao, L., Controlled Synthesis of Yolk–Mesoporous Shell Si@$SiO_2$ Nanohybrid Designed for High Performance Li Ion Battery. *RSC Adv.* **2014,** *4* (40), 20814-20820.
41. Sun, Z.; Tao, S.; Song, X.; Zhang, P.; Gao, L., A Silicon/Double-Shelled Carbon Yolk-Like Nanostructure as High-Performance Anode Materials for Lithium-Ion Battery. *J. Electrochem. Soc.* **2015,** *162* (8), A1530-A1536.
42. Xie, J.; Tong, L.; Su, L.; Xu, Y.; Wang, L.; Wang, Y., Core-Shell Yolk-Shell Si@C@Void@C Nanohybrids as Advanced Lithium Ion Battery Anodes with Good Electronic Conductivity and Corrosion Resistance. *J. Power Sources* **2017,** *342*, 529-536.
43. Su, L.; Xie, J.; Xu, Y.; Wang, L.; Wang, Y.; Ren, M., Preparation and Lithium Storage Performance of Yolk-Shell Si@void@C Nanocomposites. *J. Phys. Chem. Chem. Phys.* **2015,** *17* (27), 17562-5.
44. Ma, Y.; Tang, H.; Zhang, Y.; Li, Z.; Zhang, X.; Tang, Z., Facile Synthesis of Si-C Nanocomposites with Yolk-Shell Structure as an Anode for Lithium-Ion Batteries. *J. Alloys Compd.* **2017,** *704*, 599-606.
45. Zhou, X.-y.; Tang, J.-j.; Yang, J.; Xie, J.; Ma, L.-l., Silicon@Carbon Hollow Core–Shell Heterostructures Novel Anode Materials for Lithium Ion Batteries. *Electrochim. Acta* **2013,** *87*, 663-668.
46. Liu, N.; Wu, H.; McDowell, M. T.; Yao, Y.; Wang, C.; Cui, Y., A Yolk-Shell Design for Stabilized and Scalable Li-Ion Battery Alloy Anodes. *Nano Lett.* **2012,** *12* (6), 3315-21.
47. Tao, H.; Fan, L. Z.; Song, W. L.; Wu, M.; He, X.; Qu, X., Hollow Core-Shell Structured Si/C Nanocomposites as High-Performance Anode Materials for Lithium-Ion Batteries. *Nanoscale* **2014,** *6* (6), 3138-42.
48. Yang, J.; Wang, Y.-X.; Chou, S.-L.; Zhang, R.; Xu, Y.; Fan, J.; Zhang, W.-x.; Kun Liu, H.; Zhao, D.; Xue Dou, S., Yolk-Shell Silicon-Mesoporous Carbon Anode with Compact Solid Electrolyte Interphase Film for Superior Lithium-Ion Batteries. *Nano Energy* **2015,** *18*, 133-142.
49. Lin, D.; Lu, Z.; Hsu, P.-C.; Lee, H. R.; Liu, N.; Zhao, J.; Wang, H.; Liu, C.; Cui, Y., A High Tap Density Secondary Silicon Particle Anode Fabricated by Scalable Mechanical Pressing for Lithium-Ion Batteries. *Energy Environ. Sci.* **2015,** *8* (8), 2371-2376.
50. Ma, C.; Wang, Z.; Zhao, Y.; Li, Y.; Shi, J., A Novel Raspberry-like Yolk-Shell Structured Si/C Micro/Nano-Spheres as High-Performance Anode Materials for Lithium-Ion Batteries. *J. Alloys Compd.* **2020,** *844*, 156201.
51. Chen, S.; Gordin, M. L.; Yi, R.; Howlett, G.; Sohn, H.; Wang, D., Silicon Core-Hollow Carbon Shell Nanocomposites With Tunable Buffer Voids for High

Capacity Anodes of Lithium-Ion Batteries. *J. Phys. Chem. Chem. Phys.* **2012,** *14* (37), 12741-5.
52. Hummers, W. S.; Offeman, R. E., Preparation of Graphitic Oxide. *J. Am. Chem. Soc.* **2002,** *80* (6), 1339-1339.
53. Wu, J. J.; Bennett, W. R., Fundamental Investigation of Silicon Anode. *2012 IEEE Energytech* **2012**, 1-5.
54. Li, J.; Yuan, X.; Lin, C.; Yang, Y.; Xu, L.; Du, X.; Xie, J.; Lin, J.; Sun, J., Achieving High Pseudocapacitance of 2D Titanium Carbide (MXene) by Cation Intercalation and Surface Modification. *Adv. Energy Mater.* **2017,** *7* (15), 1602725.
55. Li, Q.; Liu, X.; Han, X.; Xiang, Y.; Zhong, G.; Wang, J.; Zheng, B.; Zhou, J.; Yang, Y., Identification of the Solid Electrolyte Interface on the Si/C Composite Anode with FEC as the Additive. *ACS Appl. Mater. Interfaces* **2019,** *11* (15), 14066-14075.
56. Xu, Y.; Swaans, E.; Chen, S.; Basak, S.; R. M. L. Harks, P. P.; Peng, B.; Zandbergen, H. W.; Borsa, D. M.; Mulder, F. M., A High-Performance Li-Ion Anode from Direct Deposition of Si Nanoparticles. *Nano Energy* **2017,** *38*, 477-485.
57. Veith, G. M.; Doucet, M.; Sacci, R. L.; Vacaliuc, B.; Baldwin, J. K.; Browning, J. F., Determination of the Solid Electrolyte Interphase Structure Grown on a Silicon Electrode Using a Fluoroethylene Carbonate Additive. *Sci Rep* **2017,** *7* (1), 6326.
58. Schroder, K. W.; Celio, H.; Webb, L. J.; Stevenson, K. J., Examining Solid Electrolyte Interphase Formation on Crystalline Silicon Electrodes: Influence of Electrochemical Preparation and Ambient Exposure Conditions. *J. Phys. Chem. C* **2012,** *116* (37), 19737-19747.

# CHAPTER VI

# SUMMARY AND FUTURE DIRECTIONS

## Summary

Silicon anodes were successfully fabricated and their device performance was shown. We critically evaluated three major issues with silicon anodes, which is delamination, low energy density due to excessive dead weight, and unstable solid electrolyte interphase (SEI) formation.

Delamination in silicon anodes occurs due to huge volume changes during lithiation and delithiation. This issue can be minimized by adding binder to the silicon anode. We evaluated redox-active polymer, poly(fluorene-*alt*-naphthalene diimide) (PFNDI) as a binder for silicon anodes. As a binder, PFNDI exhibited poor performance, which was attributed to its poor adhesion to the silicon particles and its non-redox activity within silicon working potential window of 0.01 V to 1 V *vs.* $Li/Li^+$.

Typically, high molecular weight long chain polymeric binders are added to silicon anode in order to minimize delamination during battery cycling. On the other hand, we showed that small molecules, such as tannic acid, can be used as binder. Tannic acid (TA) is a small, branched, water-soluble polyphenol with a large number of hydroxyl (-OH) functional groups, and it performed comparably to many polymeric binders and excelled in an in-house comparison to poly(vinylidene fluoride) (PVDF) and poly(acrylic acid) (PAA). We showed that the optimum electrode composition of 70 wt% silicon, 10 wt% TA, 20 wt% CB balanced both electronic conductivity and active material accessibility and this electrode demonstrated a discharge capacity of 850 mAh/g at the $600^{th}$ cycle at

0.5 C. We showed that density of functional groups on a binder is an important parameter, and higher the value, better is the binding ability to silicon. Along with density of functional groups, the architecture of binder is important, and branching increases the point of contact to silicon, further improving the binding ability. Additionally, by using a representative molecules of tannic acid, we isolated the effects of hydrogen bonding without the effects of large-scale particle-to-particle bridging caused by high molecular weight polymers.

Owing to the poor electronic conductivity of silicon, huge amounts of carbon conductive additives (30-50 wt%), along with binder (5-25 wt%), are added to improve the electronic network and mechanical integrity of the anode, respectively. These additives are considered as "dead weight" because they do not store energy. Excessive usage of these additives dilutes the silicon active material, which overall reduces the total energy density of the anode. We showed that the carbon additives can be replaced with much lower amount of $Ti_3C_2T_x$ MXene nanosheets to overall improve the total capacity of the anode. We designed electrodes with a high silicon content of 80 wt%, 16 wt% Alg binder and 4 wt% MXene nanosheets. These electrodes demonstrated stable capacities around 900 mAh/$g_{Si}$ (720 mAh/$g_{total}$) at a high C-rate of 0.5 C, which was higher than a comparable electrode made in-house containing 4 wt% carbon black. Despite having such a low MXene content (4 wt%), our electrodes exhibited specific energies comparable to electrode containing higher amounts of rGO, CNTs or MXenes. The stable electrode performance even with a minimal MXene content is attributed to several factors: (1) highly uniform silicon electrodes due to the dispersibility of MXenes in water, (2) the high

MXene aspect ratio that enables improved electrical connections, and (3) hydrogen bonding among MXenes, sodium alginate, and silicon particles.

The one major issue with silicon anode which was not evaluated in the previous chapters is the formation of unstable SEI. This occurs because of continuous exposure of silicon to electrolyte during battery cycling because of volume changes. This is a critical problem because SEI formation drastically drops the cycling capacities and Coulombic efficiencies. Adding binder would probably wrap the silicon particles and minimize its exposure to electrolyte, however, the excessive volume changes would still cause SEI buildup due to breakage of binder protective layer. On the other hand, a "yolk-shell" type structure will ensure that minimum exposure of silicon particles to electrolyte. We made a yolk-shell structure by crumpling/encapsulating silicon particles using MXene nanosheets via a spray dryer. This method is fairly easy and straightforward compared to the traditional method of creating such a structure, which involves multiple steps of forming and removing sacrificial layer. We optimized the Si/MX content in the capsule as well the PVDF binder content in the electrode to increase the active material loading. The high capacities observed for Si/MX=32/68 wt% electrode with 5 wt% PVDF binder is attributed to balance of MXene and silicon nanoparticles in a capsule. We show that our crumpled electrodes demonstrated specific capacity of 550 $mAh/g_{total}$ at a current density of 1.7 $A/g_{total}$ (or 0.5 C-rate) at $200^{th}$ cycle for electrode loading of 1.5 $mg/cm^2$. We reduced the cross-section expansion after cycling to 13%, which is lowest compared to our previous studies on silicon anodes. An in-house comparison of crumpled architecture to the uncrumpled architecture revealed the advantages of effective wrapping of silicon

particles by MXene nanosheets which minimized SEI formation and improved cycle life of anode.

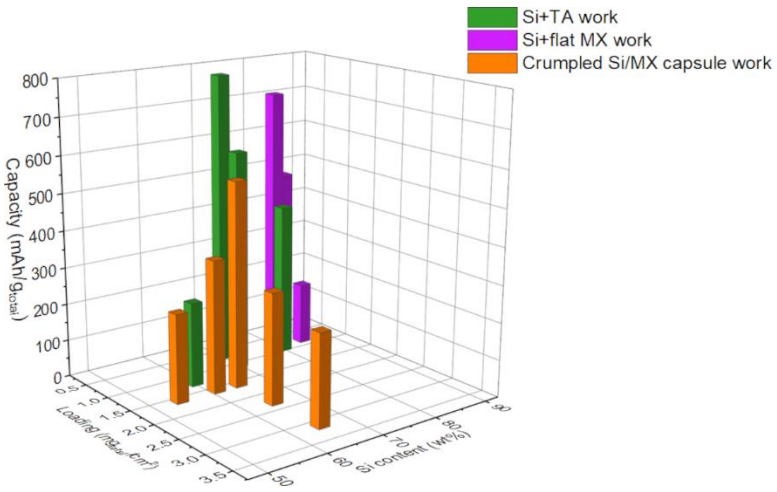


Figure VI-1. Summary of cycling data form Chapter III, IV, and V.

Figure VI-1 summarizes the data from Chapter III, IV, and V. We plotted a 3D graph with capacity (mAh/$g_{total}$), loading ($mg_{total}/cm^2$), and silicon content (wt%). Battery performance depends on wide range of parameters, but we chose to represent electrode loading and silicon content as we believe that these two are critical parameters to achieve high energy density silicon anodes. For Si+TA work (Chapter III), we were able to achieve optimum cycling performance with silicon content of 70 wt%. However, when we tried to either increase or decrease the silicon content, the cycling capacities dropped. Also, as we increases the electrode loading, we observed a slight drop in the cycling capacities. This can be attributed to increased cell resistance due to formation of thicker electrodes. For the Si+low MX work (Chapter IV), when we replaced the carbon additives with MXene nanosheets, we were able to increase the silicon content to 80 wt% without affecting cycling capacities to greater extent. However, when we further tried to increase the silicon

content we observed drastic drop in capacities. This can be attributed to imbalance of electrode components that led to poor formation of hydrogen bonding interactions and poor electronic connectivity. Finally, for the crumpled S/MX capsule work (Chapter V), unfortunately, we were not able to increase the silicon content in the electrode beyond 65wt%. However, we were able to make higher loading electrodes (>1.2 $mg_{total}/cm^2$), which we were not able to do for the previous chapters. This shows that the high tap density of capsules allow for formation of higher loading electrodes without any issues of crack formation of delamination.

**Future directions**

Through silicon anodes with TA as a binder showed comparable performance as compared to other widely studied binders widely for silicon anodes, the performance can be further improved by either making a composite of TA with other binders or cross-linking the TA.

We combined TA with binders such as carboxymethyl cellulose (CMC) and polydopamine (PD). However, we did not see any significant improvement in capacities (Figure VI-2). This is probably because the essential hydrogen bonding groups of TA ware utilized to form interactions with CMC or PD, which reduced its availability to bind with silicon. Thus, instead of combing TA with other binders, it is recommended to cross-link TA with itself or with other binder molecules that has high density of hydrogen bonding functional groups (for *e.g.* citric acid).

Because the phenol moieties of TA can be further modified to impart additional functionality using simple organic chemistry, it should not be difficult to incorporate

crosslinking into TA structures. We performed initial evaluations on a thermally cross-linked TA. For that, we first synthesized methacrylated TA (MTA) following a previous report.[1] Following that, we made silicon electrodes using MTA as binder, and (2-hydroxy-2-methylpropiophenone) as a thermal initiator. We observed lower cycling capacities as compared to anodes made using TA as a binder. We attributed this behavior to the steric hindrance cause by the bulky groups, that minimized the exposure of -OH groups which are critical to improve the binding ability to silicon. A future direction would be to systematically methacrylate the pyrogallol groups on TA so as to find an optimum balance that will allow for effective cross-linking without causing much steric hindrance. Another future direction would be add $Li^+$ ion conducting groups, which will not only improve binding ability to silicon, but also improve the ion-diffusion within the binder.

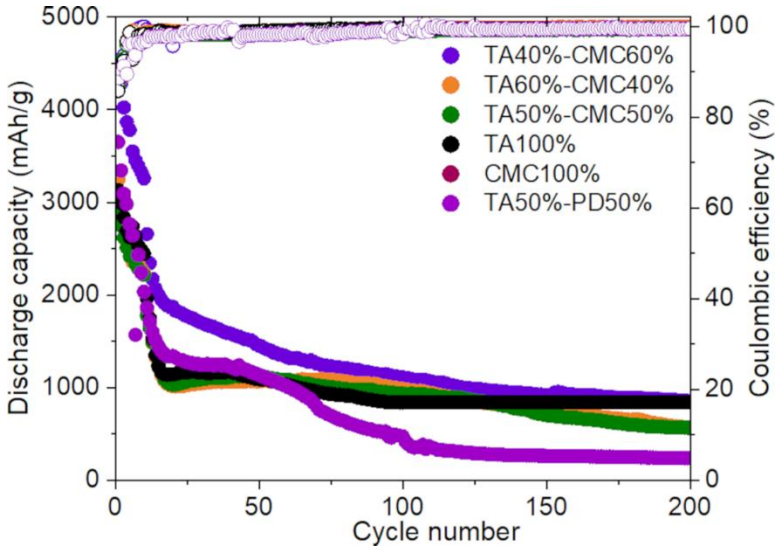


Figure VI-2. Galvanostatic cycling performance of silicon electrodes with different binders.

Addition of just 4 wt% MXenes improved the cycling performance of silicon anode and also the total energy density. We made electrodes with high silicon content of 80 wt%. However, we added 16 wt% of sodium alginate binder so as to make structurally strong electrode. A future direction will be to further reduce the binder content in ethe electrode. This can be achieved by choosing a new binder, for *e.g.* TA that has abundant --OH groups to improve binding ability to both silicon and MXenes. Due to very low viscosity of TA+water composite, there is a possibility of aggregation of MXene nanosheets causing inhomogeneous electrode formation. This can be reduced by utilizing crosslinked TA. Additionally, the antioxidative property of TA would reduce oxidation of MXene nanosheets and improve its stability.[2] We believe that in the future, as the MXene synthesis becomes more mature, it would be easier to tune the properties of MXenes, For *e.g.*, the dead weight in silicon anodes can be further reduced by utilizing MXenes which have larger lateral size, are more conductive, and have a uniform distribution of -OH functional groups. A systematic study on varying the MXene properties and understanding its effect on anode performance should be conducted, so as to find the best performing MXene for silicon anode.

Though the Si/MX crumpled electrode architecture improved the SEI stability and reduced the through plane expansion during cycling, the capacities obtained were very low. This is probably because of excessive crowding of silicon particles within the capsule which affects the contact of silicon particles with the conductive MXene shell. Future work will involve optimization of MXene sheet size for efficient contact of silicon particle

within capsules. Instead of using PVDF as a binder, crosslinked TA can be used as a binder here to further improve structural integrity of the electrode made with Si/MX capsules.

Finally, future work to make silicon electrode made with Si/MX capsule, TA as binder, and MXene as conductive additive/binder is desired.

**References**

1. Shim, J.; Bae, K. Y.; Kim, H. J.; Lee, J. H.; Kim, D. G.; Yoon, W. Y.; Lee, J. C., Solid Polymer Electrolytes Based on Functionalized Tannic Acids from Natural Resources for All-Solid-State Lithium-Ion Batteries. *ChemSusChem* **2015,** *8* (24), 4133-8.
2. Zhao, X.; Vashisth, A.; Prehn, E.; Sun, W.; Shah, S. A.; Habib, T.; Chen, Y.; Tan, Z.; Lutkenhaus, J. L.; Radovic, M.; Green, M. J., Antioxidants Unlock Shelf-Stable $Ti_3C_2T$ (MXene) Nanosheet Dispersions. *Matter* **2019,** *1* (2), 513-526.